

AD-A153 827 EXPERIMENTAL AND THEORETICAL INVESTIGATION OF MICROWAVE 1/1
AND MILLIMETER WA. (U) MARYLAND UNIV COLLEGE PARK
W W DESTLER 30 DEC 84 AFOSR-TR-85-0408 AFOSR-83-0013

EXPERIMENTAL AND THEORETICAL INVESTIGATION OF MICROWAVE
AND MILLIMETER WA. (U) MARYLAND UNIV COLLEGE PARK
M W DESTLER 30 DEC 84 AFOSR-TR-85-0408 AFOSR-83-0013

1/1

UNCLASSIFIED

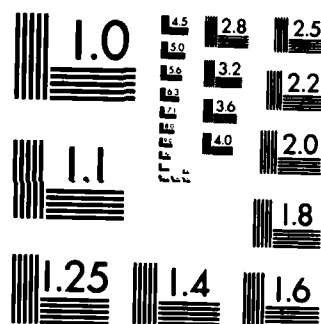
F/G 20/7

NL

END

14 MED

OT 15



MICROCOPY RESOLUTION TEST CHART
NATIONAL BUREAU OF STANDARDS-1963-A

AFOSR-TR. 85-0408

2
②

EXPERIMENTAL AND THEORETICAL INVESTIGATION OF MICROWAVE AND MILLIMETER
WAVE RADIATION FROM HOLLOW, ROTATING ELECTRON BEAMS

Contract No. AFOSR-83-00130

PROGRESS REPORT

For the Period December 1, 1983 through November 30, 1984

Submitted to

Air Force Office of Scientific Research

Prepared by

The Electrical Engineering Department and
The Laboratory for Plasma and Fusion Energy Studies
University of Maryland
College Park, Maryland 20742

DTIC
ELECTE
MAY 16 1985
S A D

Approved for public release;
distribution unlimited.

85 04 22 108

AD-A153 827

DTIC FILE COPY

UNCLASSIFIED

SECURITY CLASSIFICATION OF THIS PAGE

REPORT DOCUMENTATION PAGE

1a. REPORT SECURITY CLASSIFICATION UNCLASSIFIED		1b. RESTRICTIVE MARKINGS	
2a. SECURITY CLASSIFICATION AUTHORITY		3. DISTRIBUTION/AVAILABILITY OF REPORT Approved for public release; Distribution unlimited	
2b. DECLASSIFICATION/DOWNGRADING SCHEDULE			
4. PERFORMING ORGANIZATION REPORT NUMBER(S)		5. MONITORING ORGANIZATION REPORT NUMBER(S) AFOSR-TR. 85-0408	
6a. NAME OF PERFORMING ORGANIZATION University of Maryland	6b. OFFICE SYMBOL (If applicable) NP	7a. NAME OF MONITORING ORGANIZATION AFOSR/NP	
6c. ADDRESS (City, State and ZIP Code) The Electrical Engineering Department and The Laboratory for Plasma & Fusion Energy Studies College Park, MD 20742		7b. ADDRESS (City, State and ZIP Code) Building 410 Bolling AFB DC 20332-6448	
8a. NAME OF FUNDING/SPONSORING ORGANIZATION AFOSR	8b. OFFICE SYMBOL (If applicable) NP	9. PROCUREMENT INSTRUMENT IDENTIFICATION NUMBER AFOSR 83-0013	
8c. ADDRESS (City, State and ZIP Code) Building 410 Bolling AFB DC 20332-6448		10. SOURCE OF FUNDING NOS.	
		PROGRAM ELEMENT NO. 61102F	TASK NO. 2301
		TASK NO. A8	WORK UNIT NO. N/A
1. TITLE (Include Security Classification) "EXPERIMENTAL & THEORETICAL INVESTIGATION OF MICROWAVE & MILLIMETER WAVE RADIATION FROM HOLLOW ROTATING ELECTRO BEAMS"			
2. PERSONAL AUTHOR(S) Dr William W. Destler			
11a. TYPE OF REPORT ANNUAL	13b. TIME COVERED FROM 1 Dec 83 TO 30 Nov 84	14. DATE OF REPORT (Yr., Mo., Day) 30 Dec 84	15. PAGE COUNT 54
16. SUPPLEMENTARY NOTATION			
COSATI CODES		18. SUBJECT TERMS (Continue on reverse if necessary and identify by block number)	
FIELD	GROUP	SUB. GR.	
ABSTRACT (Continue on reverse if necessary and identify by block number) Studies of the production of microwave and millimeter wave radiation from rotating electron beams have been pursued at the University of Maryland under AFOSR sponsorship since 1978. In the period 1978-1981, these studies entered the broadband radiation produced when a rotating electron beam interacts with the TE and/or TM modes of a smooth cylindrical conducting boundary system. These early studies led in 1981 to the first demonstration of a new type of coherent radiation source at microwave and millimeter wave wavelengths with demonstrable advantages over existing sources. This device, informally called a Cusp Injected Magnetron or Cusptron by members of our group, produces radiation by the resonant interaction of a rotating electron beam with the modes of a magnetron-type conducting boundary.			
DISTRIBUTION/AVAILABILITY OF ABSTRACT CLASSIFIED/UNLIMITED <input checked="" type="checkbox"/> SAME AS RPT. <input type="checkbox"/> DTIC USERS <input type="checkbox"/>		21. ABSTRACT SECURITY CLASSIFICATION Unclassified	
NAME OF RESPONSIBLE INDIVIDUAL r Robert J. Barker		22b. TELEPHONE NUMBER (Include Area Code) 202/767-5011	22c. OFFICE SYMBOL NP

FORM 1473, 83 APR

EDITION OF 1 JAN 73 IS OBSOLETE.

UNCLASSIFIED

SECURITY CLASSIFICATION OF THIS PAGE

EXPERIMENTAL AND THEORETICAL INVESTIGATION OF MICROWAVE AND MILLIMETER
WAVE RADIATION FROM HOLLOW, ROTATING ELECTRON BEAMS

Contract No. AFOSR-83-00134

PROGRESS REPORT

For the Period December 1, 1983 through November 30, 1984

Submitted to

Air Force Office of Scientific Research

Prepared by

The Electrical Engineering Department and
The Laboratory for Plasma and Fusion Energy Studies
University of Maryland
College Park, Maryland 20742

AIR FORCE OFFICE OF SCIENTIFIC RESEARCH (AFOSR)
NOTICE OF TRANSMITTAL TO DTIC
This technical report is approved for distribution under the provisions of AFOSR-12.
Distribution is unlimited.
MATTHEW J. KILPATRICK
Chief, Technical Information Division



PROGRESS REPORT

SUBMITTED TO: Air Force Office of Scientific Research

SUBMITTED BY: Electrical Engineering Department
Laboratory for Plasma and Fusion Energy Studies
University of Maryland
College Park, Maryland 20742

GRANT NUMBER: AFOSR-83-0013

PERIOD: December 1, 1983 through November 30, 1984

PRINCIPAL INVESTIGATORS: William W. Destler
Associate Professor
Electrical Engineering Department

Charles D. Striffler
Associate Professor
Electrical Engineering Department

TITLE OF PROPOSED RESEARCH: "Experimental and Theoretical Investigation of
Microwave and Millimeter Wave Radiation from
Hollow, Rotating Electron Beams"

I. INTRODUCTION

Studies of the production of microwave and millimeter wave radiation from rotating electron beams have been pursued at the University of Maryland under AFOSR sponsorship since 1978. In the period 1978-1981, these studies centered around the broadband radiation produced when a rotating electron beam interacts with the TE and/or TM modes of a smooth cylindrical conducting boundary system. These early studies led in 1981 to the first demonstration of a new type of coherent radiation source at microwave and millimeter wave wavelengths with demonstrable advantages over existing sources. This device, informally called a Cusp Injected Magnetron or Cusptron by members of our group, produces radiation by the resonant interaction of a rotating electron beam with the modes of a magnetron-type conducting boundary.

The advantages of this new type of radiation source are best understood by comparison to a conventional magnetron [Fig. 1(a)]. In a magnetron, electrons are thermionically or field emitted from a central cathode and accelerated toward a multiresonator anode block. A strong applied magnetic field prevents the electrons from reaching the anode, and the resulting mean electron motion is essentially an $E \times B$ drift around the device. This circulating electron space charge interacts resonantly with the modes of the slotted outer conducting boundary, which acts as a cylindrical slow wave structure. Although efficient

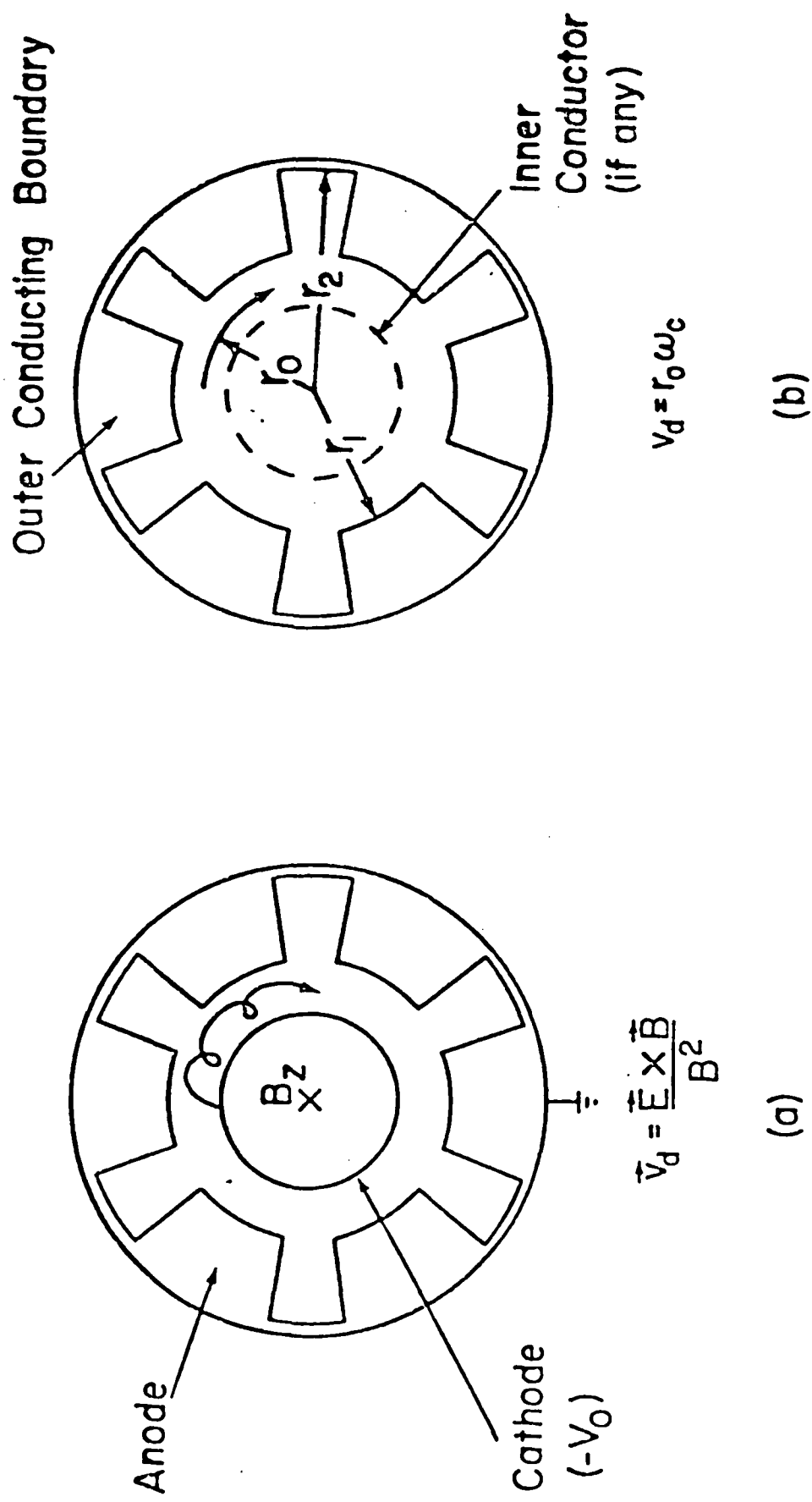


Figure 1. (a) Conventional magnetron, (b) Cusp injected magnetron.

radiators at low frequencies (2-8 GHz), magnetrons suffer from inherent limitations, including:

- a) The strong applied magnetic field needed to prevent the electrons from crossing the anode-cathode gap results in a slow electron circulation velocity, and thus a limit to the operating frequency (the operating frequency is roughly equal to the number of resonators times the circulation frequency of electrons around the device).
- b) Since the electric field in a magnetron is a function of radius, there is considerable velocity shear in the beam, resulting in multimoding difficulties whenever the number of slots exceeds 6-8.
- c) As electrons lose energy to radiation, they are accelerated by the applied electric field into the slots, where they strike the walls, form plasma, and eventually short out the device. Thus, magnetrons do not perform well in the long pulse or cw regimes, especially at high power.
- d) Since the center conductor of a magnetron is the cathode, the dimensions of the device are determined more by diode design requirements than by wave considerations.

In a Cusp Injected Magnetron [Figs. 1(b), and 2], a high quality rotating electron beam is produced by injecting a non-rotating hollow beam through a narrow magnetic cusp. The resultant rotating beam interacts resonantly with the modes of a magnetron-type conducting boundary system, a resonance which is driven strongly by the negative mass instability. The advantages of such a device are now clear:

- a) Much lower magnetic fields may be used, since the required larmor radius is much larger.
- b) Higher frequency operation should be possible, since the circulation velocity of the electrons is now simply $r_o \omega_c$, a value at least twice, and more typically five times, that in a conventional magnetron.
- c) Since the rotating beam is essentially devoid of velocity shear, operation with higher slot numbers should be possible before multimoding occurs.
- d) Because there are no applied voltages in the interaction region, electrons move to smaller radii as they lose energy, and long pulse or cw operation at high power should be possible.

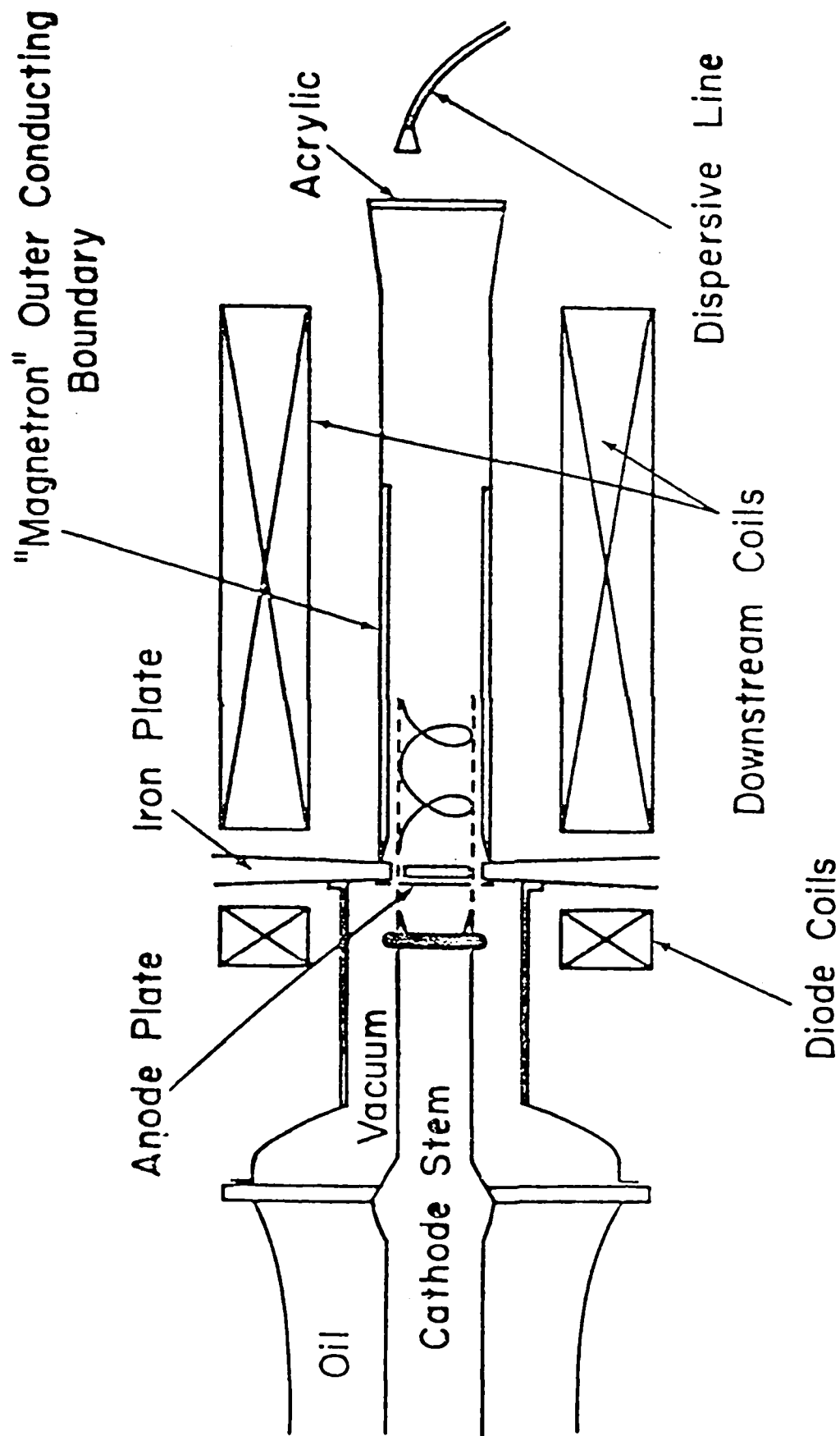


Figure 2. Cusp injected magnetron.

- e) Since the diode has been separated from the interaction region, the dimensions of the device are not determined by diode design considerations.

During the period 1981-1983, experiments were conducted on a large pulse line accelerator which had originally been constructed to produce intense rotating electron rings for collective ion acceleration experiments. Using rotating beams with typical parameters of 2 MeV, 2 kA, 5 ns, about 15% of the electron beam power was converted to microwave radiation at the 12th harmonic of the cyclotron frequency (9.6 GHz) by the interaction of the rotating beam with a 12 slot outer magnetron boundary. Experiments continue on this facility at the present time, and during the past grant period we have succeeded in producing comparable output at the 20th harmonic (16 GHz), and are currently working on optimizing radiation at the 30th and 40th harmonics. Extensive theoretical efforts have accompanied this experimental work at every stage.

In 1983, we also completed construction of a small table-top experiment designed to demonstrate the feasibility of this concept at low electron energy and current (20-40 kV, 1 A). During the past grant period, we have reported efficient production of microwave radiation at the 6th harmonic in this device, using applied magnetic fields of only 250 gauss. Experiments on radiation production at the 12th harmonic are currently in progress.

The past year has seen real progress in our efforts to understand theoretically the physics involved in the radiation production process. Improved modeling of both the empty cavity modes and the beam modes is allowing a more systematic design of experiments, and we have made progress in understanding mode competition issues.

During the past grant period we have also conducted a brief study of the radiation production from rotating electron beams interacting with a periodic wiggler magnetic field produced by samarium cobalt magnets interior and exterior to the beam. This work has been conducted in collaboration with Professor George Bekefi's group at MIT, and the initial results of this work (in which radiation has been observed in the frequency range 100-170 GHz), are very encouraging.

Section II of this report details progress made during the past grant period. A list of publications and presentations resulting from this work is enclosed in Appendix A and recent publications are enclosed in Appendix B.

II. PROGRESS REPORT

December 1, 1983 to November 30, 1984

A. Experimental Research

1. Improvements to the Experimental Facilities. During the past year, the experimental facilities have been enhanced by the completion of the CUSPTRON low voltage, low current, table top experimental facility, and by the installation of diagnostic equipment on the high power facility in K-band (18-26 GHz). The latter installation means that we now have diagnostic equipment in place over the entire range 7-50 GHz, all of which is available to help diagnose the radiation from the low power experiment as well.

2. High Power Experiments. During the past year, experimental work on the high power pulse line facility (2 MeV, 2 kA, 5 ns), has concentrated on the production of radiation at the 20th harmonic of the electron cyclotron frequency (16 GHz). To this end, we have conducted improved measurements of the rotating beam profile as a function of axial position in the interaction region (Fig. 3). These measurements have led to the design of an improved 20 slot outer magnetron boundary system, with a dramatic improvement in radiation production at this frequency over previously reported designs. In these experiments, about 15% of the injected electron beam power was converted to radiation at 16 GHz, using an applied magnetic field of only 1400 gauss (Fig. 4). A

WILMUS FLAT MEASUREMENTS OF BEAM CROSS-SECTION

AS A FUNCTION OF AXIAL POSITION.

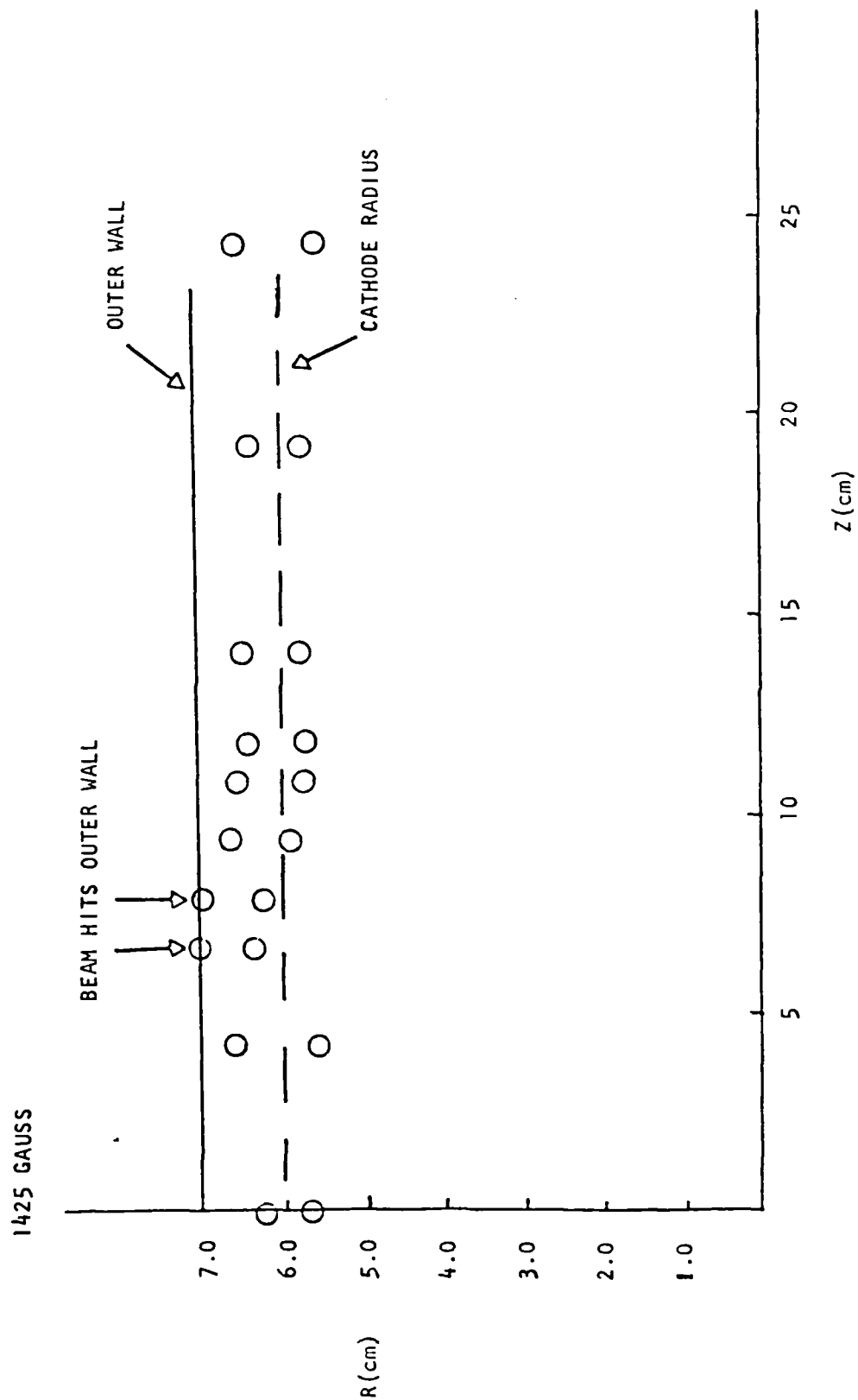


Figure 3

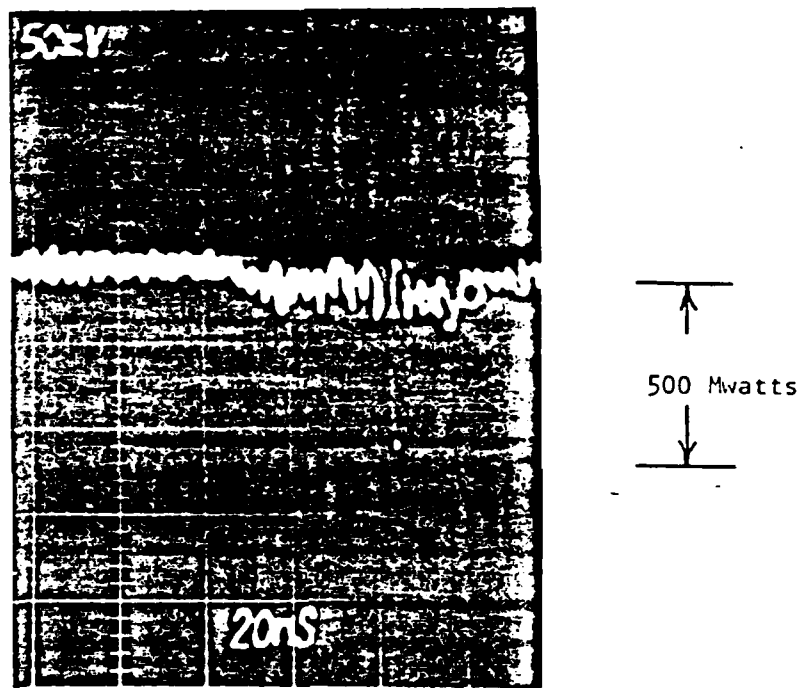
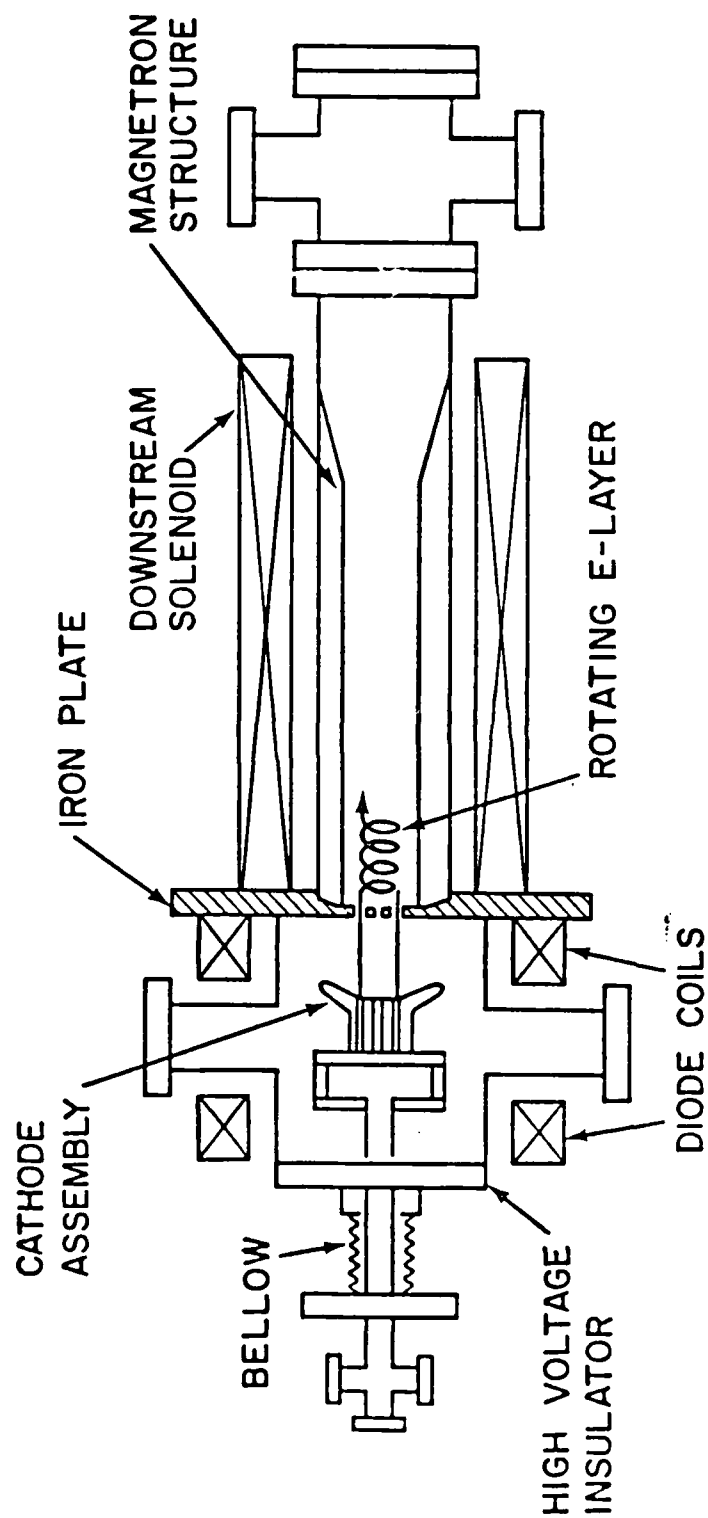


Figure 4. Microwave signal in Ku-band(12-18GHz) after passing through a 36 meter long dispersive line. The 500 Mwatt burst is determined to be at a frequency of 15.5 GHz by its arrival time at the detector. Power at other frequencies is typically down by a factor of at least 30.

paper detailing these new results is currently under preparation. Design and construction of 30 and 40 slot systems is currently in progress.

3. Low Power Experiments--CUSPTRON. Initial experiments on the table top experiment, CUSPTRON (20-30 kV, 1 A, 5 μ s, 100 pps) (Fig. 5) have concentrated on demonstrating the feasibility of this concept at low electron energy and current. Thus, initial experiments were designed to operate at the 6th harmonic (about 4 GHz). During the past year, we reported the efficient (over 10%) production of radiation at this frequency using an applied magnetic cusp field of about 250 gauss. These results were published in Physics of Fluids Letters, a copy of which is enclosed in Appendix B. Experiments to produce radiation at the 12th harmonic are currently in progress.

4. Rotating Beam Free Electron Laser Experiments. In this work, conducted on the high power facility in collaboration with Professor George Bekefi's group at MIT, a rotating beam interacts with a periodic wiggler field produced by samarium cobalt magnets placed interior and exterior to the beam (Fig. 6). Thus, the device is essentially a continuously circulating Free Electron Laser, and is expected to produce radiation upshifted in frequency from that of the wiggler wavelength by a factor of γ^2 . Initial results of these experiments are that at least 200 kW of radiation was observed in T-band (100-170 GHz) with the wiggler magnets in place. When the wiggler field was removed, radiation at these frequencies fell to levels too low to be measured by our



RELATIVE AXIAL MAGNETIC FIELDS
AT BEAM RADIUS

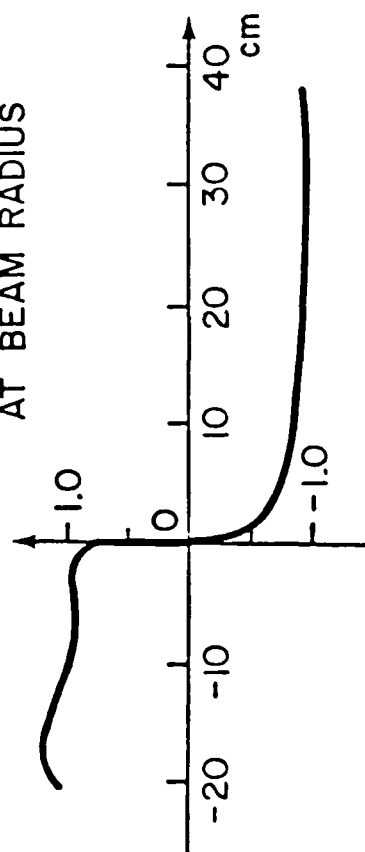


Figure 5.

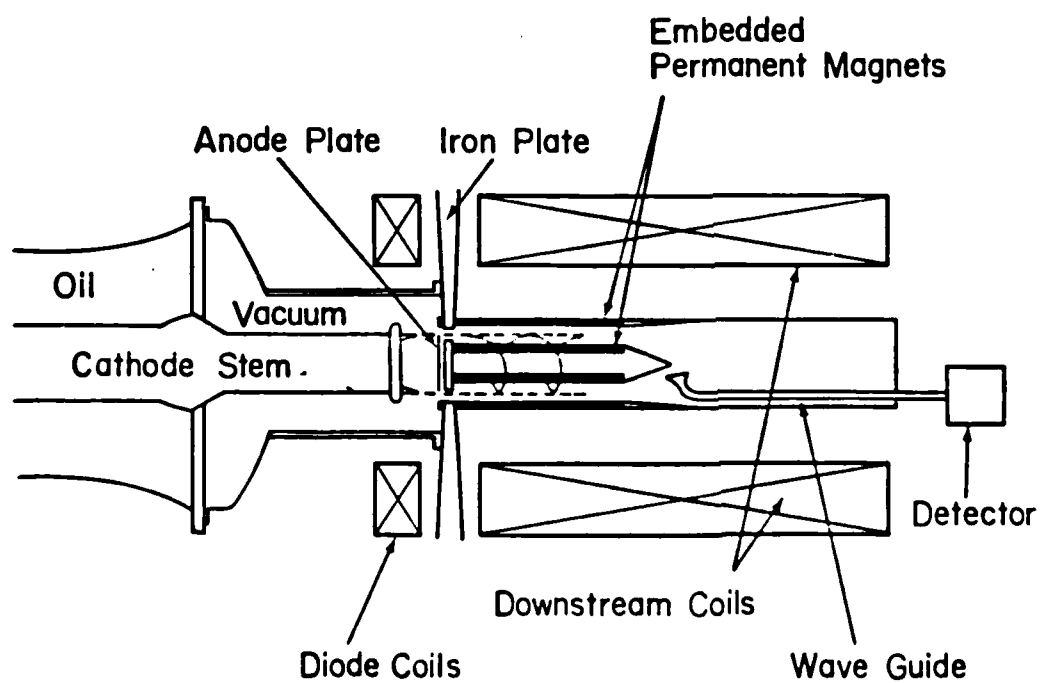
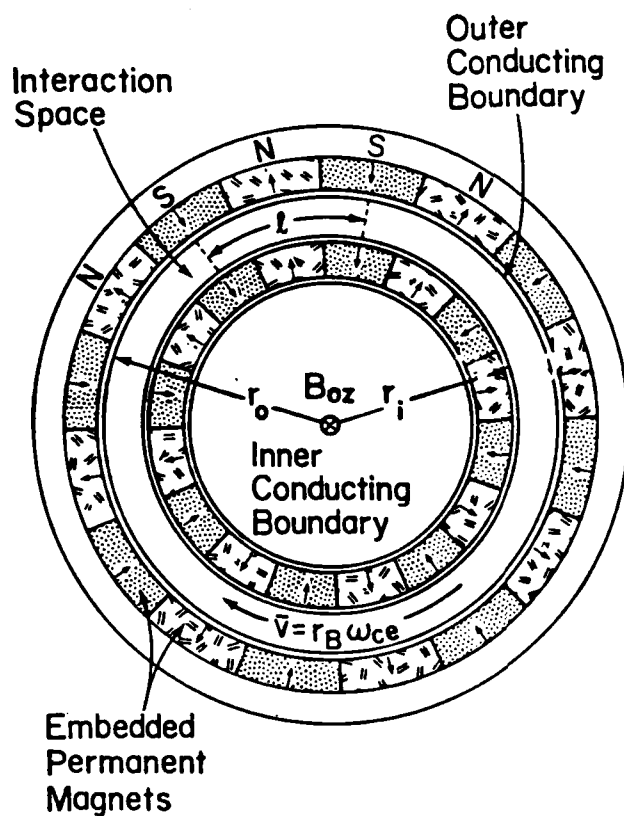


Figure 6.

diagnostic equipment. These results have been reported in a paper published in Applied Physics Letters, enclosed in Appendix B.

B. Theoretical Research

Over the past year, we have made substantial progress in our theoretical understanding of the cusp injected-slotted wall (magnetron) microwave system. One of the main areas of increased understanding occurred with respect to the importance of initial conditions. This work will appear in the Ph.D. thesis of Ravi Kulkarni and was presented at the Fall 1983 APS meeting. The important point of this analysis is the initial shape of the beam front (symmetric or preloaded) and the system geometry that it is entering. If a nonloaded beam is injected into a smooth wall, all eigenfunctions of the guide system are necessary to create the beam front field profile, that is, all l harmonics of the TE and TM modes. However, if the nonloaded beam is injected into a waveguide with slots on the outer wall, a set of different field eigenfunctions is present. The dominant eigenfunction is the dc field and multiples of the number of slots N_s , $2N_s$, Thus, a nonloaded beam injected into N_s slots has a dominant field preference for the $2\pi(N_s)$ mode. The actual form factor is the familiar $\sin(x)/x$ function.

The second important theoretical contribution this past year came in the detailed study of field profile for high frequency generation. When the number of slots increases to the regime of 20-40, the frequency regime is sufficiently high that beam location relative to the slots

becomes very important. In this regime we are operating on a high radial mode number, thus the beam should be located on a peak of the electric field profile that also happens to couple well to the slot modes. Since there are many radial peaks, this location becomes increasingly important. Thus, it is not sufficient to look only at resonance conditions but also at details of the beam location and coupling efficiency to the slots. Again this work was presented at the 1983 APS meeting and will appear in Ravi Kulkarni's Ph.D. thesis. This work is coupled to the linear growth rate analysis that appears in our most recent published works (see Refs. 15 and 16, Appendix A, and also enclosed in Appendix B).

Also during the past year we have initiated studies in the following areas:

1. General formalism of the linear stability of rotating electron beams in various wall configurations.
2. Analysis of the modes and linear stability in a dielectric lined waveguide.

APPENDIX A

Publications and Presentations Resulting from this Work

APPENDIX A

Publications and Presentations Resulting from this Work

1. W. W. Destler, D. W. Hudgings, M. J. Rhee, S. K. Kawasaki, and V. L. Granatstein, "Experimental Study of Microwave Generation and Suppression in a Non-Neutral E-Layer," J. Appl. Phys. 48, 3291 (1977).
2. W. W. Destler, W. Namkung, and R. L. Weiler, "Experimental Study of Intense Microwave Generation by the Negative Mass Instability," Bull. Am. Phys. Soc. 24, 1068 (1979).
3. W. Namkung, H. Romero, and C. D. Striffler, "Theoretical Study of Microwave Generation from a Rotating E-Layer-Coaxial Waveguide System," Bull. Am. Phys. Soc. 24, 1068 (1979).
4. T. F. Wang and C. D. Striffler, "Negative Mass Instability of a Relativistic E-Ring in a Hollow Waveguide," Bull. Am. Phys. Soc. 24, 1068 (1979).
5. W. W. Destler, C. D. Striffler, W. Namkung, H. Romero, and R. Weiler, "High Power Microwave Generation from an Intense Rotating Electron Beam," 1980 IEEE Int. Conf. on Plasma Science, Madison, WI, May 19-21, 1980.
6. W. W. Destler, R. Kulkarni, C. D. Striffler, and R. L. Weiler, "High Power Microwave Generation from a Cusp-Injected Magnetron," Bull. Am. Phys. Soc. II, 25, 886 (1981).
7. W. W. Destler, R. L. Weiler, and C. D. Striffler, "High Power Microwave Generation from a Rotating E-Layer in a Magnetron-Type Waveguide," Appl. Phys. Lett. 38, 570 (1981).
8. W. W. Destler, R. Kulkarni, C. D. Striffler, and R. L. Weiler, "High Power Microwave Generation from a Rotating E-Layer in Various Conducting Wall Systems," 1981 IEEE Int. Conf. on Plasma Science, Santa Fe, NM, May 18-20, 1981.
9. W. W. Destler, H. Romero, C. D. Striffler, R. L. Weiler, and W. Namkung, "Intense Microwave Generation from a Non-Neutral Rotating E-Layer," J. Appl. Phys. 52, 2740 (1981).
10. R. Kulkarni, D. Calderone, and C. D. Striffler, "Stability of a Rotating E-Layer in a Magnetron-Type Waveguide," Bull. Am. Phys. Soc. 26, 935 (1981).

11. W. W. Destler, D. Calderone, R. Kulkarni, W. Namkung, R. Weiler, and C. D. Striffler, "High-Power Microwave Generation from an Intense Rotating Electron Beam," 1982 IEEE Int. Conf. on Plasma Science, Ottawa, Ontario, Canada, May 17-19, 1982.
12. R. Kulkarni, C. D. Striffler, W. W. Destler, and R. L. Weiler, "Mode Structure and Interaction of a Rotating Relativistic Electron Beam in a Magnetron-Type Waveguide," Bull. Am. Phys. Soc. 27, 1073 (1982).
13. W. W. Destler, R. Kulkarni, C. D. Striffler, and R. L. Weiler, "Microwave Generation at High Harmonics of the Electron Cyclotron Frequency," Bull. Am. Phys. Soc. 27, 1017 (1982).
14. W. Namkung, W. Lawson, W. W. Destler, and C. D. Striffler, "Microwave Generation from a Non-Relativistic Rotating E-Layer through a Magnetic Cusp (Cusptron)," Bull. Am. Phys. Soc. 27, 1062 (1982).
15. W. W. Destler, R. Kulkarni, C. D. Striffler, and R. L. Weiler, "Microwave Generation from Rotating Electron Beams in Magnetron-Type Waveguides," J. Appl. Phys. 54, 4152 (1983).
16. C. D. Striffler, W. W. Destler, R. Kulkarni, and R. L. Weiler, "High Power Microwave Generation from Rotating E-Layers in Magnetron-Type Conducting Boundary Systems," IEEE Trans. Nucl. Sci. NS-30, 3429 (1983).
17. H. S. Uhm, C. M. Kim, and W. Namkung, "Linear Theory of Cusptron Microwave Tubes," Phys. Fluids 27, 488 (1984).
18. W. W. Destler, "Experimental Studies of High Power Microwave Generation from Rotating Electron Beams in Magnetron-Type Waveguides," Bull. Am. Phys. Soc. 28, 1087 (1983).
19. R. Kulkarni and C. D. Striffler, "Interaction of a Rotating Electron Beam with a Cylindrical Slotted Wall Structure," Bull. Am. Phys. Soc. 28, 1087 (1983).
20. W. Namkung, "Observation of Microwave Generation from a Cusptron Device," Phys. Fluids 27, 329 (1984).
21. G. Bekefi, R. E. Shefer, and W. W. Destler, "Millimeter Wave Emission from a Rotating Electron Ring in a Rippled Magnetic Field," Appl. Phys. Lett. 44, 280 (1984).
22. G. Bekefi, R. E. Shefer, and W. W. Destler, "Millimeter Wave Radiation from a Rotating Electron Beam in a Rippled Magnetic Field," IEEE Int. Conf. on Plasma Science, St. Louis, MO, May 14-16, 1984.

23. R. Kulkarni, W. W. Destler, W. G. Lawson, C. D. Striffler, and S. B. Swanekamp, "High Power Microwave Generation from a Cusp-Injected Intense Relativistic Electron Beam," IEEE Int. Conf. on Plasma Science, St. Louis, MO, May 14-16, 1984.

APPENDIX B

Copies of Papers Published and Abstracts of Papers Presented

HIGH POWER MICROWAVE GENERATION FROM ROTATING E-LAYERS

IN MAGNETRON-TYPE CONDUCTING BOUNDARY SYSTEMS*

C. D. Striffler, W. W. Destler, R. Kulkarni, and R. L. Weller

Electrical Engineering Department and
Laboratory for Plasma and Fusion Energy Studies
University of Maryland
College Park, Maryland 20742

Summary

Studies of the production of microwave and millimeter wave radiation at high harmonics of the relativistic electron cyclotron frequency by the interaction of a rotating E-layer with a multi-resonator magnetron boundary system have been conducted. The interaction of a 2 MeV, 1-2 kA, 5 ns cusp injected E layer of radius 6 cm with 12, 20, and 40 slot magnetron type waveguides are studied. Approximately 10% of the injected electron beam power is converted to microwaves at 12ω (10 GHz), 2% at 20ω (17 GHz), and 1% at 40ω (34 GHz). We have theoretically examined this system via analyzing the resonant interaction of a doppler shifted electron beam mode with the modes of the conducting boundary system. The location of these resonant interactions in frequency agrees well with the observed spectrum.

I. Introduction

The interest in high power microwave/millimeter sources in the past few years has resulted from possible applications in such areas as heating of fusion plasmas, particle accelerators, and communications. Among these new sources are gyrotrons, free electron lasers, and relativistic magnetrons. In this paper, we report studies of another such source in which high power radiation is generated at high harmonics of the relativistic electron cyclotron frequency ω by the resonant interaction of a fast rotating E-layer beam mode with the waveguide modes of a magnetron-type conducting boundary. This concept was first reported by our group in 1981¹ after extensive work on microwave production in hollow and coaxial boundary systems.² Recent theoretical studies³ indicate that these rotating beam-slotted wall systems should operate over a wide range of electron energies and currents and at frequencies into the millimeter regime. We have also initiated work to explore the low electron energy regime.⁴ The potential of such devices to produce radiation near high harmonics of the electron cyclotron frequency makes them especially attractive because of the relatively low applied magnetic field required compared to gyrotrons and magnetrons operating at the same frequency.

In Fig. 1, a schematic of the experimental configuration is shown. A rotating E-layer is produced by passing a hollow nonrotating beam through a narrow symmetric magnetic cusp. The downstream axis encircling particles propagate along various inner and/or outer conducting wall structures. The cross-section of a slotted structure on both the inside and outside walls is shown in Fig. 2. The outer surface of the inner wall has a radius R_i and the outer wall a radius R_o . The beam of radius R_b (~ 6 cm) rotates at a velocity $V \sim c$ in the region between the inner and outer wall. The depth of the slots is indicated by

d_s . We have examined systems in which the number of slots is 12 or 20 placed on either the inner or outer walls or both. We present theoretical (Section II) and experimental (Section III) studies of the production of radiation in these slotted wall systems.

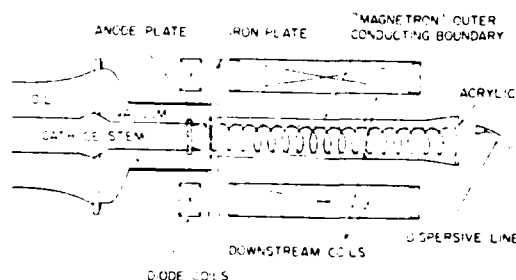


FIG. 1. Schematic of experimental system.

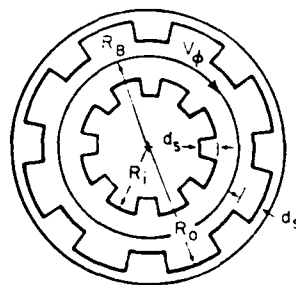


FIG. 2. Cross section of downstream slotted-wall cylindrical tube.

II. Model of Beam-Slotted Waveguide Interaction

The general dispersion relation describing the TE mode structure of a slotted wall conductor as shown in Fig. 2 can be derived by first solving the wave equation for H_z in the slot spaces and the interaction region [$R_i < r < R_o - d_s$, see Fig. 2] separately and then matching the corresponding tangential electric and magnetic fields. The resulting equations can then be solved by expanding the eigenfunctions of both regions in terms of the other and applying Floquet's Theorem for periodic systems. The result can be calculated independently for each mode i' of the slot region. The dispersion relation for a slotted outer wall and no inner wall is

*Work supported by the Air Force Office of Scientific Research and the University of Maryland Computer Science Center.

$$D_{\ell\ell'}(k) \equiv \frac{J_{\ell'}(kR_w)N_{\ell'}(kR_0) - J_{\ell'}(kR_0)N_{\ell'}(kR_w)}{J_{\ell'}(kR_w)N_{\ell'}(kR_0) - J_{\ell'}(kR_0)N_{\ell'}(kR_w)} - \frac{N_s \Delta\theta}{2\pi} \left[\begin{matrix} 1, n' = 0 \\ 2, n' \neq 0 \end{matrix} \right] \times \frac{F_{\ell\ell'}^2}{4} \times \frac{J_{\ell'}(kR_w)}{J_{\ell'}(kR_w)} = 0 \quad (1)$$

where $\ell' = \pi n' / \Delta\theta$, $n' = 0, 1, 2, \dots$, $\ell = \ell_0 + mN_s$, $k^2 = \omega^2/c^2 - k_z^2$, $R_w = R_0 - d_s$, $\Delta\theta$ is the solid angle subtended by one slot, N_s is the number of slots, and ℓ_0 represents the phase shift from slot to slot of the field profile. We have defined

$$F_{\ell\ell'} = \frac{\sin \frac{\Delta\theta}{2}(\ell + \ell')}{\frac{\Delta\theta}{2}(\ell + \ell')} + (-1)^n \frac{\sin \frac{\Delta\theta}{2}(\ell - \ell')}{\frac{\Delta\theta}{2}(\ell - \ell')} \quad (2)$$

This dispersion relation includes not only the TEM slot resonances but the higher order resonances as well. For the case $\ell' = 0$ (constant electric field across the slot gap) the result reduces to that obtained by Collins.⁵ As an example, the mode structure ($k_z = 0$) for an outer magnetron wall with 12 (N_s) slots, $\ell' = 0$, $d_s = 1$ cm, and $R_0 = 7.5$ cm is shown in Fig. 3. The dots represent the discrete magnetron cutoff frequencies and have the same dependence on k_z as in the hollow waveguide. The numbered connecting lines from dot to dot merely serve to distinguish one radial mode n_r from another. Also shown is the beam mode $\omega = \ell_0 \omega_c = \ell_0 v_0 / R_0$ for $\gamma_0 = 6$, $R_b = 6$ cm. Note that the mode structure is periodic every $\ell_0 = 12$ (N_s) and the relative reduction in phase velocity as compared to hollow waveguide modes.

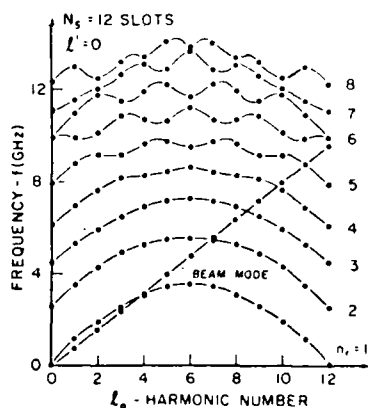


FIG. 3. Discrete mode structure for hollow waveguide with outer magnetron type boundary with parameters $R_0 = 7.5$ cm, $d_s = 1$ cm, $N_s = 12$, $\ell' = 0$, $\Delta\theta = \pi/N_s$. Beam mode line for $\gamma_0 = 6$, $R_b = 6$ cm.

The linear analysis representing the interaction of a beam wave with the modes of the waveguide proceeds by first linearizing the equations of motion and then Fourier transforming them to ω - k space. The equation of continuity is then applied to obtain the perturbed charge and current densities. These are then substituted into Maxwell's equations and solved with the magnetron type boundary conditions. From this a modified dispersion relation is obtained defining the interaction of the beam mode with the waveguide mode. The resulting first order modified dispersion relation for the fundamental mode $m = 0$ is

$$D_{\ell\ell'}(k) = - \frac{N_s \Delta\theta v_0^2 (\ell^2 - k^2 R_b^2)}{\pi \gamma_0 k R_w \omega_c^2} \times \frac{F_{\ell\ell'}^2}{4} \left[\frac{J_{\ell'}(kR_b)}{J_{\ell'}(kR_w)} \right]^2 \quad (3)$$

where $\psi_\ell = \omega - \ell_0 \omega_c - k_z v_z$, $v = e^2 n_s u R_0 / 2m_0$ and n_s is the beam surface density. This analysis represents an extension of a planar model studied in Ref. 6.

For the case of resonant interaction, $\psi_\ell \sim 0$ and $D_{\ell\ell'}(k) \sim 0$, one can obtain an explicit expression for the growth rate, $\text{Im}\omega = \omega_i$,

$$\frac{\omega_i}{\omega_c (\frac{v}{c})^{1/3}} = \frac{\sqrt{3}}{2} \left\{ \frac{N_s \Delta\theta}{\pi \omega_c} \frac{1}{k R_w} \frac{(\ell^2 - k^2 R_b^2)}{|D'_{\ell\ell'}(k_\ell)|} \times \frac{F_{\ell\ell'}^2}{4} \frac{J_{\ell'}^2(k R_b)}{J_{\ell'}^2(k R_w)} \right\}^{1/3} \quad (4)$$

where

$$D_{\ell\ell'}(k_\ell) = 0, \quad D'_{\ell\ell'}(k_\ell) = \frac{\omega}{kc^2} \left. \frac{\partial D_{\ell\ell'}(k)}{\partial k} \right|_{k=k_\ell}$$

In Fig. 4, the growth rate as given in Eq. (4) is plotted vs. ℓ for the system parameters used in the mode structure shown in Fig. 3. The number associated with each curve represents interaction with the same labeled radial mode as in Fig. 3. Note that resonance in most cases requires a finite k_z . Since the growth rates for the various modes are approximately equal, we surmise that the radial field profile in the interaction space and/or the starting conditions play an important role as to which mode(s) is present. If we examine Eq. (1) and look for modes ($\ell_0 = N_s = 12$) that have a substantial field component near the slot, we see that the mode corresponding to $n_r = 6$ (9.8 GHz) or near the zero of $J_{12}'(kR_w)$ has a field profile that peaks near the outer wall. In this case, we would expect good coupling between the waveguide and slot. The other lower radial mode numbers represent zeros near $J_{\ell}'(kR_w)$ which has a field profile that is more evenly distributed.

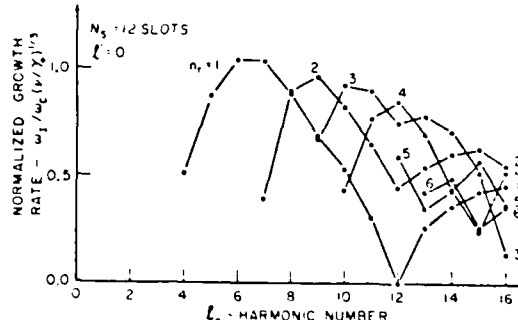


FIG. 4. Normalized growth rate for resonant beam-waveguide interaction including finite k_z . Same parameters as in Fig. 3.

III. Experimental Results

The experimental configuration is shown in Fig. 1. Hollow, nonrotating, relativistic electron beams (2 MeV, 20 kA, 30 ns) are emitted from a circular knife edge carbon cathode. A 0.5 cm wide circular slit aligned with the cathode knife edge allows a fraction of the electron beam to pass through the magnetic cusp transition region where the $v_z \times B_r$ force in this transition region converts most of the axial particle motion into azimuthal motion. The resulting rotating beam propagates in the downstream region with an axial velocity in the range 0.1-0.3 c and interacts with various conducting boundary

configurations. The radiation produced is extracted out the downstream end of the drift chamber as shown in Fig. 1. The downstream end of the drift chamber is flared to allow a smooth transition to free space, and the radiation is picked up by receiving horns connected to X-band (8-12 GHz), Ku band (12-18 GHz), and Ka band (24-40 GHz) dispersive waveguide lines 36 m in length. These dispersive lines are connected to calibrated attenuators and calibrated detectors. The spectrum is determined using standard dispersive line theory and total power is computed by multiplying the power measured at the detector by factors associated with the dialed in attenuation, the frequency dependent attenuation of the dispersive lines, and the ratio of the total area over which radiation is observed to that of the receiving horn.

The results of these experiments are presented in Fig. 5. Figures 5(a) and 5(b) show the measured spectrum for a rotating beam of radius $R_b = 6$ cm interacting with an empty circular waveguide of radius 7.5 cm. These results show the characteristic broad band spectrum associated with this configuration with power levels of around 200 kW.² Figures 5(c) through 5(f) show the resulting spectra obtained by inserting various slotted boundaries into the empty waveguide. Figure 5(c) shows the radiated power spectrum from the interaction of the beam with a slotted outer wall and no inner conductor. The outer conductor radius R_o is 7.5 cm and the slot depth d_s is 1 cm. The applied magnetic field is 1375 G. The number of slots N_s is 12. The large peak observed at 9.6 GHz corresponds to the expected resonant point near $12\omega_c$ ($f_c = 770$ MHz) and represents an increase in power over the empty waveguide case by a factor of 10^3 . Figure 5(d) shows the radiated power spectrum for a rotating beam interacting with a slotted inner conductor and a smooth outer boundary. In this case, $N_s = 20$, R_o is 7.5 cm, the inner radius R_i is 5.3 cm, and d_s is 0.4 cm. The applied magnetic field is 1387 G. A dominant peak at 16 GHz that corresponds approximately to the $20\omega_c$ resonant point is seen with an output of 30 MW. Figure 5(e) shows the results for a different 20 slot case in which the beam radius R_b is reduced to 5.25 cm and R_i is reduced to 4.85 cm, the magnetic field is set at 1575 G. These new conditions shift the cyclotron frequency up to 990 MHz which causes the $20\omega_c$ resonance to be pushed up to 20 GHz, although the power fell to about 3 MW. The drop in power by a factor of 10 for the smaller radius case can best be explained by referring to Fig. 6. Figure 6 is a plot of the axial beam current passing through the cusp as a function of the applied magnetic field. The optimum operating range for the $R_b = 6$ cm beam is at 1350-1415 G with a maximum injected current of about 3 kA. The optimum operating range of the new 5.25 cm beam is at a field of 1550-1600 G and a current of about 1 kA. If it is presumed that power is proportional to the square of the beam density and therefore to the square of the beam current, the factor of 2-3 drop in the injected current would cause a reduction in the radiated power by a factor of 4-9.

Figure 5(f) shows the radiated power spectrum for a rotating beam propagating between $N_s = 20$ slotted inner and outer conductors (180° out of phase). In this case, $R_o = 7.5$ cm, $R_i = 5.0$ cm, $d_s = 0.64$ cm, and $R_b = 6$ cm. The applied magnetic field is 1400 G. Theoretical analysis of such "glide symmetric" systems indicate that as the two slotted walls are brought closer together, the effective periodicity of the system approaches half of that possessed by either

slotted wall alone. As can be seen, the radiated power was largely moved up to 36 GHz, near $40\omega_c$. We are initiating theoretical work on this new concept.

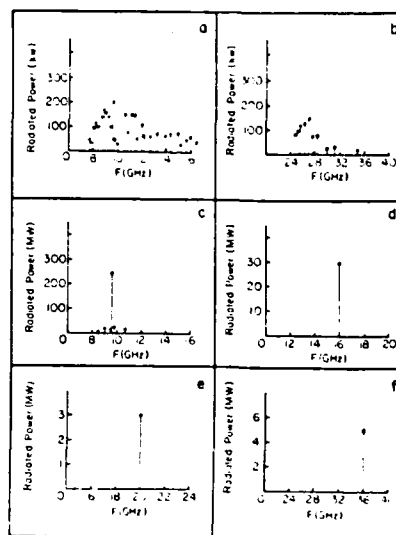


FIG. 5. Typical single shot power spectra. Smooth outer wall, no inner wall: (a) X-band, (b) Ka-band. Slotted wall structures: (c) 12 outer, (d) 20 inner, smooth outer, $R_b = 6.0$ cm, (e) same as (d) except $R_b = 5.25$ cm, (f) 20 inner/outer. Geometry is in the text.

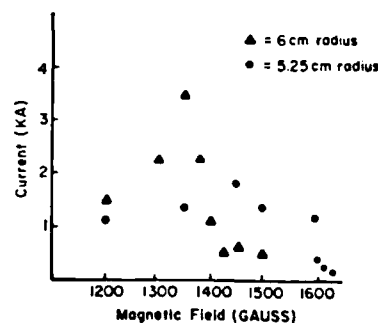


FIG. 6. Axial beam current passing through cusp as a function of magnetic field for $R_b = 6.0$ cm, $R_b = 5.25$ cm.

References

1. W. W. Destler, R. L. Weiler, and C. D. Striffler, *Appl. Phys. Lett.* **38**, 570 (1981).
2. W. W. Destler, H. Romero, C. D. Striffler, R. L. Weiler, and W. Namkung, *J. Appl. Phys.* **52**, 2740 (1981).
3. Y. Y. Lau and L. R. Barnett, *Int. J. of Infrared and Millimeter Waves*, **3**, 619 (1982) and *Int. J. of Electronics*, Oct. 1982.
4. W. Namkung, W. W. Destler, W. Lawson, and C. D. Striffler, *Bull. Am. Phys. Soc.* **27**, 1062 (1982).
5. G. R. Collins, "Microwave Magnetrons," p. 56, McGraw Hill, 1948.
6. W. W. Destler, R. Kulkarni, C. D. Striffler, and R. L. Weiler, *J. Appl. Phys.*, (to be published).
7. R. Mitra and S. Lippat, *Canadian J. of Phys.* **43**, 353 (1965).

Microwave generation from rotating electron beams in magnetron-type waveguides

W. W. Destler, R. Kulkarni, C. D. Striffler, and R. L. Weiler
University of Maryland, College Park, Maryland 20742

(Received 27 January 1983; accepted for publication 1 April 1983)

The production of high power microwave radiation at high harmonics of the electron cyclotron frequency by the interaction of a rotating electron beam with a magnetron-type conducting boundary has been studied theoretically and experimentally using a 2-MeV, 1–2-kA, 10-ns electron beam pulse. Approximately 10% of the electron beam power has been converted to microwave radiation at the 12th harmonic, and about 2% at the 20th harmonic. Radiation characteristics are in good agreement with a theoretical analysis of the resonant interaction of a beam mode with the modes of the conducting boundary system. Radiation from rotating beams in "glide-symmetric" boundary systems is also reported.

PACS numbers: 85.10.Ka

I. INTRODUCTION

The renewed interest in novel high power microwave/millimeter wave sources in the past few years has resulted from possible applications of such sources in such diverse areas as heating of fusion plasmas, particle accelerators, and communications. Among these new sources are gyrotrons,^{1–3} free electron lasers,^{4,5} and relativistic magnetrons.^{6,7} In this paper, we report experimental and theoretical studies of a new type of microwave device in which high power microwaves are generated at high harmonics of the electron cyclotron frequency (ω_c) by the injection of a rotating, axis encircling, electron layer (*E*-layer) into a magnetron-type conducting boundary configuration. This concept, first reported by our group in 1981,⁸ was derived from previous experimental and theoretical work on the microwave production from rotating *E*-layers in simple cylindrical or coaxial boundary systems.^{9,10}

The potential of such devices to produce radiation at or near high harmonics of the electron cyclotron frequency makes them especially attractive, since they require substantially less applied magnetic field strength than gyrotrons or magnetrons operating at the same frequency. Recent theoretical studies,^{11–13} moreover, indicate that they may be expected to operate over a wide range of electron energies and currents and at frequencies into the millimeter regime. In this paper, we present theoretical and experimental studies of the production of radiation in such systems at or near $12\omega_c$ and $20\omega_c$. In addition, we discuss the results of an experiment in which an *E*-layer is injected into a "glide symmetric" boundary system designed to produce radiation near the 40th harmonic. A theoretical discussion in which the radiation is modeled as a resonant interaction of a beam mode with the modes of the conducting boundary system is presented in Sec. II. The experimental results are summarized in Sec. III, and conclusions are drawn in Sec. IV.

II. ANALYSIS OF THE INTERACTION OF AN ELECTRON BEAM WITH A SLOTTED WAVEGUIDE: CARTESIAN LIMIT ($k_z = 0$)

In our experiment, a thin annular electron beam rotates about the axis of a magnetic field (B_0) slotted waveguide cy-

lindrical system as shown in Fig. 1(a). The beam's azimuthal velocity is

$$V_\phi = R_B \omega_c = \frac{R_B e B_0}{m \gamma_0}$$

and also has a velocity component along the field V_z , where

$$\beta_\phi^2 + \beta_z^2 = (V_\phi/c)^2 + (V_z/c)^2 = 1 - (1/\gamma_0^2).$$

The slotted structure is placed on either the outer wall, the inner wall, or both. In order to investigate theoretically the interaction of the beam with the modes of the guide, we have considered a cartesian model of the cylindrical system. This

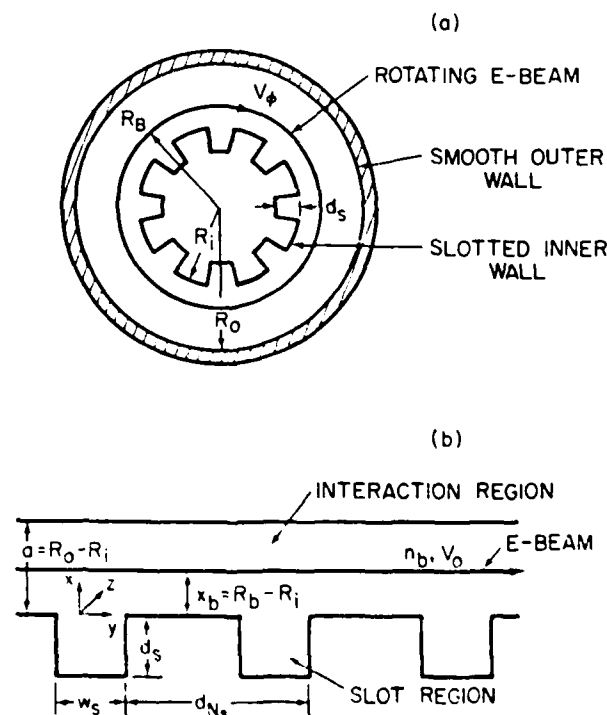


FIG. 1. (a) Experimental schematic of inner slotted coaxial waveguide with N_s slots. (b) Cartesian model of the cylindrical waveguide as a periodic planar system of N_s slots.

model is shown in Fig. 1(b). The model and dimensions are so drawn and labeled as if the slotted wall is interior to the beam and the exterior wall is smooth. The space where the beam travels, the "interaction region," has a width " a " ($= R_0 - R_i$) and the slots have a depth d_s , width w_s , and a periodicity given by the length d_N . The symbol N_s represents the number of the slots in the cylindrical system, that is, we require $N_s d_N = 2\pi R_R$. Thus, in the cartesian analysis, the system periodicity occurs in a distance $N_s d_N$. The beam is located a distance $x_b (= R_b - R_i)$ from the slots and is travelling across the slots at a velocity $V_{0i} (= V_\beta)$. The coordinate system for analysis is also shown in Fig. 1(b).

A brief comment on the cartesian model is in order because of the large amount of literature, including our own,¹⁰ that analyzed the smooth wall tube in cylindrical coordinates. In the smooth wall case, the analysis of mode structure and linear stability of the interaction of the rotating electron beam with the waveguide modes was relatively straightforward. For smooth walls, cylindrical waveguides are required in order to have any mode-beam resonance. In that case, the linearized quantities were Fourier decomposed as $\exp(i\phi + k_z z - \omega t)$. The dominant perturbation in that case was along the beam, and we obtained¹⁰

$$R_b \bar{\phi}_1 \simeq \frac{e}{m\gamma_0} \frac{(\psi_i^2/\gamma_{\phi 0}^2 + \omega_c^2 \beta_{\phi 0}^2)}{\psi_i^2 - \omega_c^2} \frac{\delta \bar{E}_\phi}{\psi_i^2}, \quad (1)$$

where $\psi_i = \omega - i\omega_c - k_z V_{\phi 0}$, $\omega_c = eB_0/m\gamma_{\phi 0}$, $\beta_{\phi 0} = R_b \omega_c/c$, $\gamma_0 = (1 - \beta_{\phi 0}^2 - \beta_{\phi 0}^2)^{-1/2}$. When analyzing resonant interaction $\psi_i \simeq 0$, the above expression can be approximated by

$$r_b \bar{\phi}_1 \simeq - \frac{e}{m\gamma_0} \beta_{\phi 0}^2 \frac{\delta \bar{E}_\phi}{\psi_i^2}, \quad (2)$$

which represents a "negative mass" effect. However, if the above analysis is taken to the cartesian limit, $V_{\phi 0} = R_b \omega_c = \text{constant}$, $R_b \rightarrow \infty$, $B_0 \rightarrow 0$, Eq. (1) becomes

$$R_b \bar{\phi}_1 \simeq \frac{e}{m\gamma_0} \frac{1}{\gamma_{\phi 0}^2} \frac{\delta \bar{E}_\phi}{\psi_i^2}, \quad (3)$$

now representing a "positive mass." Below, we will derive an expression identical to Eq. (3). With respect to the analysis at hand where we are looking for resonant interaction of a

beam wave with a waveguide mode, the sign of the mass term is not important, since the equation is cubic versus quadratic in form. Likewise, the dominance of the negative mass term or the cartesian term for a given system is not clear. The magnitude of γ_0 , location of the beam relative to the conducting wall, frequency shift, and beam density n/γ_0 , all appear to be determining factors as to which is most important. However, the relative simplicity of the modes for a cartesian slotted waveguide versus the actual cylindrical slotted waveguide has led us to pursue the former model.

A. Empty waveguide analysis: Dispersion relation

In this initial investigation, we simplify the analysis by considering the mode structure for the case of $k_z = 0$ (cut-off). When there is no beam present, the empty waveguide, the modes decompose into TE and TM waves. Only the TE mode ($E_z = 0$, $H_z \neq 0$) has a nonzero value of E_x , the electric field that couples the wave to the beam. Assuming the fields vary as $\exp(j\omega t - j\beta_n y)$, the H_z field in the interaction region, $0 < x < a$, is given by

$$H_z^I(x, y) = \sum_n A_n \cos[K_n(a - x)] e^{-j\beta_n y}, \quad (4)$$

where $K_n^2 = \omega^2/c^2 - \beta_n^2$, $\beta_n = \beta_0 + 2\pi n/d_N$, and the other nonzero fields are given by $E_x^I = -j\beta_n/\omega\epsilon_0 H_z^I$ and $E_y^I = (j/\omega\epsilon_0) \partial H_z^I / \partial x$. The quantity $\beta_n d_N$ represents the phase shift from one slot region to the next. Likewise, in the first slot region, $-d_s < x < 0$, $-w_s/2 < y < w_s/2$, the H_z field is given by

$$H_z^I(x, y) = \sum_n A_n \cos[K_n(x + d_s)] \cos[\beta_n(y + w_s/2)], \quad (5)$$

where $K_n^2 = \omega^2/c^2 - \beta_n^2$, $\beta_n = \pi n/w_s$, and the other fields are given by $E_x^I = -j/\omega\epsilon_0 \partial H_z^I / \partial y$ and $E_y^I = (j/\omega\epsilon_0) \partial H_z^I / \partial x$.

Our solution procedure is to choose one of the orthogonal modes in the slot, that is, a specific n' , and find the coefficients of the field components in the interaction region to satisfy the boundary conditions across the gap. Specifically, the continuity of E_y and H_z across the gap is required. That is, for E_y ,

$$\sum_{n=-\infty}^{\infty} A_n K_n \sin(K_n a) e^{-j\beta_n y} = \begin{cases} -A_{n'} K_{n'} \sin(K_{n'} d_s) \cos[\beta_{n'}(y + w_s/2)], & -w_s/2 < y < w_s/2 \\ 0, & w_s/2 < |y| < d_N/2, \end{cases} \quad (6)$$

and for H_z ,

$$\sum_{n=-\infty}^{\infty} A_n \cos(K_n a) e^{-j\beta_n y} = A_{n'} \cos(K_{n'} d_s) \cos[\beta_{n'}(y + w_s/2)], \quad -w_s/2 < y < w_s/2. \quad (7)$$

The dispersion relation $\omega(\beta_0)$ is determined by multiplying Eq. (6) by the eigenfunctions in the interaction region, $e^{j\beta_{n'} y}$, and integrating from $-d_N/2$ to $d_N/2$ and multiplying Eq. (7) by the eigenfunctions in the slot region, $\cos[\beta_{n'}(y + w_s/2)]$, and integrating from $-w_s/2$ to $w_s/2$. The dispersion relation for the empty waveguide¹⁵ becomes

$$D_{n'}(\omega, \beta_0) \equiv \begin{cases} 1 & \text{if } n' = 0 \\ 1/2 & \text{if } n' \neq 0 \end{cases} \times \frac{\cot(K_{n'} d_s)}{K_{n'} w_s} + \sum_{n=-\infty}^{\infty} \frac{\cot(K_n a)}{K_n d_N} F_{n,n} = 0, \quad (8)$$

where

$$F_{n,n'} = \left\{ \frac{\sin \left[\frac{\omega_i}{2} (\beta_{n'} + \beta_n) \right]}{\frac{\omega_i}{2} (\beta_{n'} + \beta_n)} + (-1)^{n'} \frac{\sin \left[\frac{\omega_i}{2} (\beta_{n'} - \beta_n) \right]}{\frac{\omega_i}{2} (\beta_{n'} - \beta_n)} \right\}^2 \quad (9)$$

Specifically for the $n' = 0$ slot mode, the dispersion relation¹⁶ becomes

$$D_{0,0}(\omega, \beta_0) = \frac{\cot \left(\frac{\omega d_i}{c} \right)}{\frac{\omega}{c} w_i} + \sum_{n=-\infty}^{\infty} \frac{\cot(K_n a)}{K_n d_{N_i}} \left(\frac{\sin \left[\frac{\omega_i \beta_n}{2} \right]}{\frac{\omega_i \beta_n}{2}} \right)^2 = 0. \quad (10)$$

For this slot mode, which is a TEM mode in the slot, the electric field across the gap is $E_y^i(0, y) = -[jA_0/\epsilon_0 c] \sin(\omega d_i/c)$, a spatially constant electric field.

B. Beam-waveguide linear stability analysis

The analysis of the slotted waveguide when the electron beam is present is based on the assumption that the beam only slightly perturbs the empty waveguide fields. The electron beam in the cartesian model [Fig. 1(b)] is a thin sheet beam of uniform density, $n_b = n_s \delta(x - x_b)$, located a distance x_b from the slot. The beam travels with a velocity across the slots given by $V_b = V_0 a_y$. The relativistic mass ratio of this equilibrium beam is $\gamma_0 = (1 - V_0^2/c^2)^{-1/2}$.

The linear stability of the beam-waveguide system to small perturbations is examined as follows. The beam particles and resulting fields are perturbed according to $\exp[j(\omega t - \beta_n y)]$ with a complex amplitude that depends on x . The perturbation produces fields of the form of TE waves. That is, $\tilde{\mathbf{E}} = (\tilde{E}_x, \tilde{E}_y, 0)$ and $\tilde{\mathbf{B}} = (0, 0, \tilde{B}_z)$, all assumed to be small. The linearized equations of motion give

$$\begin{aligned} \tilde{v}_x &= -\frac{e}{jm\gamma_0\psi_n} [\tilde{E}_x + V_0 \tilde{B}_z], \\ \tilde{v}_y &= -\frac{e}{jm\gamma_0^3\psi_n} \tilde{E}_y, \\ \tilde{v}_z &= 0, \end{aligned} \quad (11)$$

where $\psi_n = \omega - \beta_n V_0$ and all quantities with a tilde are small. The linearized continuity equation gives the perturbed beam density

$$\tilde{n} = -\frac{1}{j\psi_n} \frac{\partial}{\partial x} n_b \tilde{v}_x + \frac{n_b \beta_n}{\psi_n} \tilde{v}_y. \quad (12)$$

From these the perturbed charge and current density in Maxwell's equations can be computed. They are

$$\tilde{\rho} = -e\tilde{n} = \frac{e}{j\psi_n} \left[\frac{\partial}{\partial x} (n_b \tilde{v}_x) - n_b j\beta_n \tilde{v}_y \right] \quad (13a)$$

and

$$\tilde{J}_x = -en_b \tilde{v}_x, \quad (13b)$$

$$\tilde{J}_y = -en_b \tilde{v}_y - eV_0 \tilde{n}. \quad (13c)$$

All perturbed quantities can be written in terms of the fields via Eq. (11). We now proceed to solve Maxwell's equations in the interaction space with the electron beam. We write the solutions for \tilde{H}_z in the form

$$\tilde{H}_z = \begin{cases} A_n \cos[K_n(a-x)] e^{-j\beta_n y}, & x_b < x < a \\ [B_n \cos(K_n x) + C_n \sin(K_n x)] e^{-j\beta_n y}, & 0 < x < x_b \end{cases} \quad (14)$$

from which we can calculate \tilde{E}_x and \tilde{E}_y . We then apply the boundary conditions at the electron beam, which are: continuity of \tilde{E}_y , which gives

$$\frac{\partial \tilde{H}_z}{\partial x} \Big|_{x_b^+} = \frac{\partial \tilde{H}_z}{\partial x} \Big|_{x_b^-} \quad (15)$$

and jump in \tilde{H}_z due to the perturbed surface current, which gives

$$\tilde{H}_z(x_b^+) - \tilde{H}_z(x_b^-) = \frac{en_s \omega}{\psi_n} \tilde{v}_y(x_b). \quad (16)$$

These boundary conditions allow us to write all the fields in the interaction space in terms of one coefficient, say B_n . We then sum the fields over all these interaction space modes and match these fields to one of the modes in the slot, i.e., the n' mode as we did in Eqs. (6) and (7). From this we obtain a modified dispersion relation given by

$$\left\{ \begin{array}{l} 1 \text{ if } n' = 0 \\ 1/2 \text{ if } n' \neq 0 \end{array} \right\} \times \frac{\cot(K_{n'} d_i)}{K_{n'} w_i} + \sum_{n=-\infty}^{\infty} \frac{F_{n,n'}}{K_n d_{N_i}} \frac{\cos(K_n a) + \alpha K_n \cos(K_n x_b) \sin[K_n(a-x_b)]}{\sin(K_n a) + \alpha K_n \sin(K_n x_b) \sin[K_n(a-x_b)]} = 0, \quad (17)$$

where $\alpha = e^2 n_i / m \epsilon_0 \gamma_0^3 \psi_n^2 \equiv (v/\gamma_0)(4\pi c^2/\gamma_0^2 \psi_n^2)$. For the appropriate limit, $v/\gamma_0 \ll 1$, the first-order modified dispersion relation becomes

$$\begin{aligned} D_{n'}(\omega, \beta_0) &= \left\{ \begin{array}{l} 1 \text{ if } n' = 0 \\ 1/2 \text{ if } n' \neq 0 \end{array} \right\} \times \frac{\cot(K_{n'} d_i)}{K_{n'} w_i} + \sum_{n=-\infty}^{\infty} \frac{\cot(K_n a)}{K_n d_{N_i}} F_{n,n'} \\ &= -\frac{1}{d_{N_i}} \frac{v}{\gamma_0} \frac{4\pi c^2}{\gamma_0^2} \sum_{n=-\infty}^{\infty} \frac{1}{\psi_n^2} \frac{\sin^2[K_n(a-x_b)]}{\sin^2 K_n a} F_{n,n'} \end{aligned} \quad (18)$$

using Eq. (8). The left-hand side, when equal to zero, represents the empty waveguide dispersion relation and the right-hand side represents the electron beam effects.

We solve Eq. (18) in order to determine the interaction of the electron beam and the waveguide modes. We look for solutions where $\omega = \beta_0 V_0 + \delta\omega$, for $|\delta\omega| \ll \beta_0 V_0 \equiv \omega_0$. Expanding $D_n(\omega, \beta_0)$ about ω_0 and multiplying by $(\delta\omega)^2$ we obtain from Eq. (18)

$$D_n(\omega_0, \beta_0)(\delta\omega)^2 + \left. \frac{\partial D_n}{\partial \omega} \right|_{\omega_0} (\delta\omega)^3 \approx - \frac{1}{d_N} \frac{v}{\gamma_0} \frac{4\pi c^2}{\gamma_0^2} F_{0,n} \frac{\sin^2[K_0(a - x_b)]}{\sin^2(K_0 a)}, \quad (19)$$

where we kept only the $n = 0$ term on the right-hand side of Eq. (18), and $K_0 = \sqrt{\omega_0^2/c^2 - \beta_0^2}$. Equation (19) is solved and the results are displayed and discussed shortly. For the case of beam-waveguide resonance, i.e., $D_n(\omega_0, \beta_0) = 0$, Eq. (19) is a third-order equation for $\delta\omega$ and possesses an unstable root of growth rate

$$\frac{\omega_I}{(v/\gamma_0)^{1/3}} = \frac{\text{Im } \omega}{(v/\gamma_0)^{1/3}} = \frac{\sqrt{3}}{2} \left\{ \frac{1}{\left. \frac{\partial D_n}{\partial \omega} \right|_{\omega_0}} \frac{1}{d_N} \frac{4\pi c^2}{\gamma_0^2} F_{0,n} \times \frac{\sin^2[K_0(a - x_b)]}{\sin^2(K_0 a)} \right\}^{1/3}. \quad (20)$$

Since this represents the maximum growth rate, all results are normalized to the factor $(v/\gamma_0)^{1/3}$. From Eq. (19), when the second-order term in $\delta\omega$ dominates on the left-hand side (nonresonance), the stability of the mode is determined by the sign of $D_n(\omega_0, \beta_0)$.

C. Results

The results of the analytical analysis are presented in graphical form in Figs. 2–6. In Figs. 2 and 3, the empty slotted waveguide mode structure [Eq. (8)] for a 12 and 20 slot system is shown, and in Figs. 4–6 the linear growth rates [imaginary part of $\delta\omega$ in Eq. (19)] are shown.

In Fig. 2, the dispersion relation for a 12 slot waveguide system is displayed. Referring to Fig. 1(b), the geometric parameters are: $a = 2.5$ cm, $d_N = 3.14$ cm, $d_s = 1.0$ cm, $w_s = 1.57$ cm. In Fig. 2(a), the dispersion relation of the system for the $n' = 0$ slot mode is shown and for the $n' = 1$ slot mode in Fig. 2(b). Specifically, frequency in GHz is plotted versus $\beta_0 d_N$, where $\beta_0 d_N = 2\pi$ means the phase of the electric field across all slot gaps is in exactly the same direction at any time and when $\beta_0 d_N = \pi$, it means the field changes direction from gap to gap. For reference, the equivalent azimuthal harmonic number l for a cylindrical system is plotted along with $\beta_0 d_N$. Since the system is assumed to repeat itself every 12 slots, the spectrum is discrete, indicated by the "dots." If the system is not bounded in y , the dispersion curves are continuous as shown by the solid lines. Obviously, the dispersion curve repeats itself every 2π in $\beta_0 d_N$. For reference, the beam wave $\omega = \beta_0 V_0$ for a beam with $\gamma_0 = 6$ is drawn which is very close to the velocity of light line on this graph. This value of γ_0 corresponds to an electron energy of about 2.5 MeV. The experiments reported in the next section

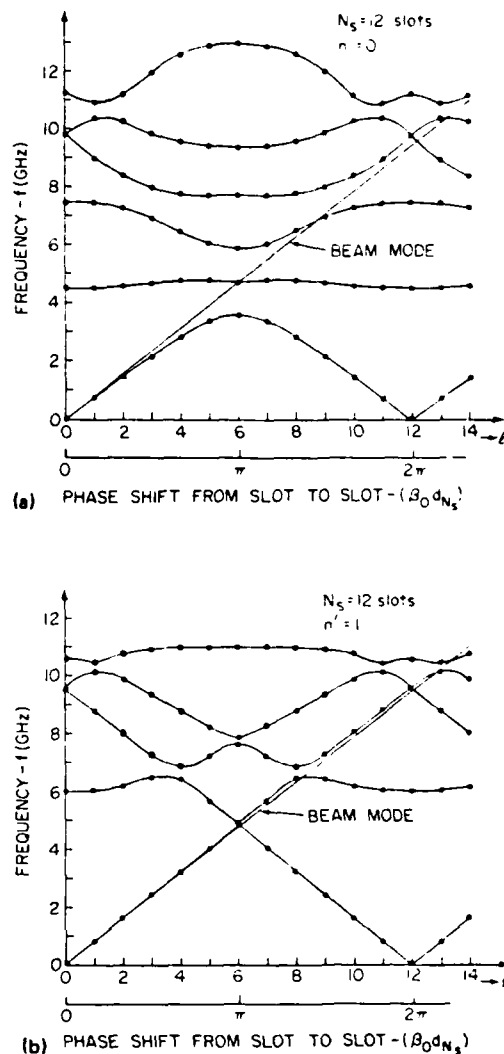


FIG. 2. Vacuum waveguide mode structure for a 12 (N_s) slot periodic planar waveguide with geometry $a = 2.5$ cm, $d_N = 3.14$ cm, $d_s = 1.0$ cm, $w_s = 1.57$ cm. The interacting beam mode is also shown ($\gamma_0 = 6$). (a) $n' = 0$: zero-order slot mode; (b) $n' = 1$: first-order slot mode.

were performed with injected electron beam energies in the range 2–2.5 MeV, with associated $\gamma_0 = 5$ –6. We find these results to be relatively insensitive to variations in γ_0 over this range. One should note that if no slots are present ($d_s = 0$), the dispersion relation would be $\omega = c\sqrt{k_y^2 + (n\pi/a)^2}$ and thus no modes have a phase velocity less than the velocity of light, and thus there can be no beam-waveguide mode resonant interaction. Obviously, the presence of the slots slows the waves down to below the velocity of light allowing resonant interaction. One can think of the various modes displayed in Figs. 2(a) and 2(b) as x-mode structure which is equivalent to radial (r) mode structure in the cylindrical system.

In Fig. 3, the dispersion relation for a 20 slot waveguide system is displayed in the same manner as in Fig. 2. The

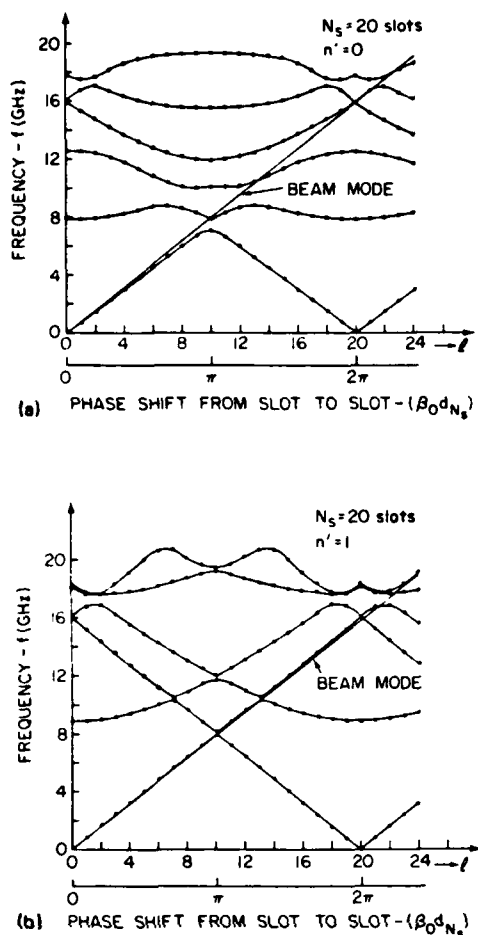


FIG. 3. Vacuum waveguide mode structure for a 20(N_s) slot periodic planar waveguide with geometry $a = 1.7$ cm, $d_N = 1.885$ cm, $d_s = 0.4$ cm, $w_s = 0.6283$ cm. The interacting beam mode is also shown ($\gamma_0 = 6$). (a) $n' = 0$: zero-order slot mode; (b) $n' = 1$: first-order slot mode.

geometry of this system is, $a = 1.7$ cm, $d_N = 1.885$ cm, $d_s = 0.4$ cm, $w_s = 0.6283$ cm. The dispersion relation for the $n' = 0$ slot mode is shown in Fig. 3(a) and for the $n' = 1$ slot mode in Fig. 3(b). Again the beam mode ($\gamma_0 = 6$) is displayed.

In Fig. 4, the normalized growth rate is shown for the 12 slot waveguide of Fig. 2 and an electron beam that is located 1.0 cm (x_0) from the slots and has a relativistic mass ratio of $\gamma_0 = 6$. The normalization factor, $\omega_c = 2\pi f_c$, is that of an equivalent rotating beam at a radius of 6 cm. Specifically, $f_c = 0.8$ GHz. The growth rate is plotted versus frequency f and equivalent azimuthal harmonic number l ($\beta_0 d_N$). The growth rate for the $n' = 0$ slot mode is displayed in Fig. 4(a) and for the $n' = 1$ slot mode in Fig. 4(b). In Fig. 5, the normalized growth rate for a 12 slot waveguide is shown that has a slot width of half the value of that in Figs. 2 and 4, that is, $w_s = 0.785$ cm. In Fig. 6, the normalized growth rate for a 20 slot waveguide is shown that has the same geometric values as in Fig. 3 and the same beam parameters as in Figs. 4 and 5.

For discussion purposes, consider the 12 slot guide whose mode structure appears in Fig. 2 and growth rate for

electron beam interaction in Fig. 4. For the $n' = 0$ slot mode case, Fig. 2(a) indicates that there are beam mode-waveguide mode intersections in frequency and equivalent harmonic number at: 4–5 GHz ($l \sim 6$), 6–7 GHz ($l \sim 8$ or 9), 9–10 GHz ($l \sim 12$), 10–11 GHz ($l \sim 13$), etc. In Fig. 4(a), we see that there is strong interaction near these frequencies, indicated by finite growth rate and no unstable interaction at other harmonics. The frequency regime in Fig. 4(a) is extended beyond that shown in Fig. 2(a) but the same resonant interactions occur but with higher x -mode numbers. The growth rates are calculated as if the waveguide were not periodic, i.e., the dispersion relation represented by the solid line of Fig. 2(a). Though there is not exact intersection of a beam mode and a periodic waveguide mode (dots), we envision that a finite k_z will allow an intersection to occur. However, if the required k_z becomes too large, the frequency will be far removed from the spectrum regime displayed. The $n' = 1$ slot mode results in Figs. 2(b) and 4(b) can be discussed in the same manner. However, one should note that the cutoff frequency in the slot is 9.6 GHz for this mode, and thus the two unstable interactions near $l = 6$ and 8 in Fig. 4(b) represent attenuated waves in the slots but for $l \geq 12$ there are propagating modes in the slot. Clearly $n' \geq 2$ slot modes have a higher cutoff frequency in the slot and thus are not displayed, because we surmise that attenuated slot modes will not be observed.

A 12 slot waveguide with a slot width of half that used in Figs. 2 and 4 results has a growth rate spectrum in frequency as shown in Fig. 5(a) for the $n' = 0$ slot mode, and the for the $n' = 1$ in Fig. 5(b). The cutoff frequency in the slot is about 19 GHz for this width and thus all $n' = 1$ growth rates represent attenuated waves in the slot.

The results of the 20 slot guide are shown in Figs. 3 and 6. Again, unstable interaction occurs where the beam wave intersects the waveguide mode. The $n' = 1$ mode has a cutoff frequency in the slot of about 24 GHz indicating that only the unstable interactions above this value while propagate out of the system.

These results should be compared with those of the smooth hollow waveguide-electron beam interaction presented in Ref. 10. In those results, all beam harmonics (l) were unstable once resonant interaction could occur, whereas in the present analysis, the guide mode structure does not allow for every l mode to resonantly interact.

III. EXPERIMENT

A. Apparatus

In our configuration, a rotating relativistic E -layer is produced by passing a hollow nonrotating beam through a narrow symmetric magnetic cusp. The downstream chamber, in which the rotating beam propagates, has a conducting wall structure that is similar to that of the magnetron. The experimental configuration is shown schematically in Fig. 7. A hollow, nonrotating, relativistic electron beam (2–2.5 MeV, 20 kA, 30 ns) is emitted from a 12-cm-diam circular knife-edge carbon cathode located 7.5 cm upstream of the anode. A 0.5-cm-wide circular slit in the anode plate allows a fraction of the diode current to pass through the

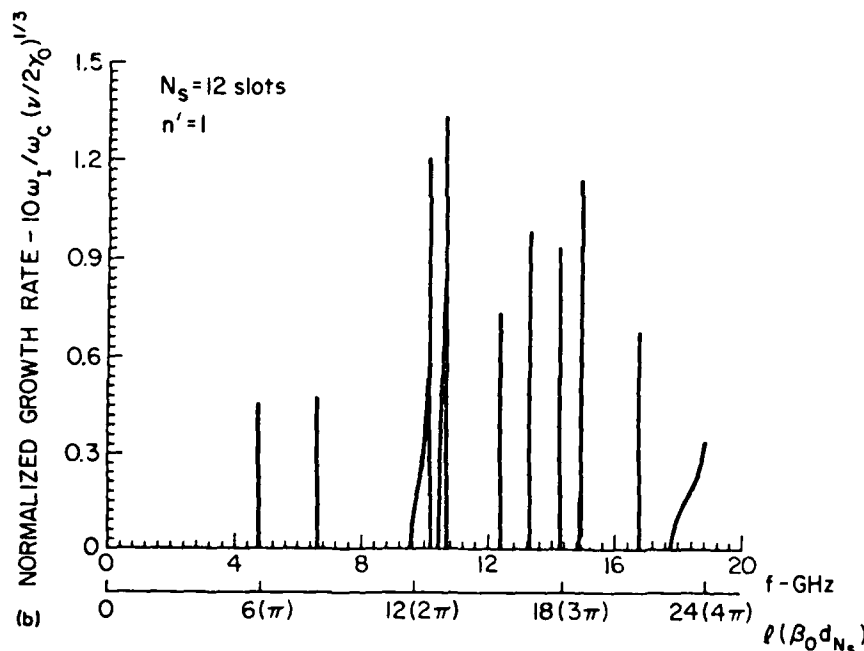
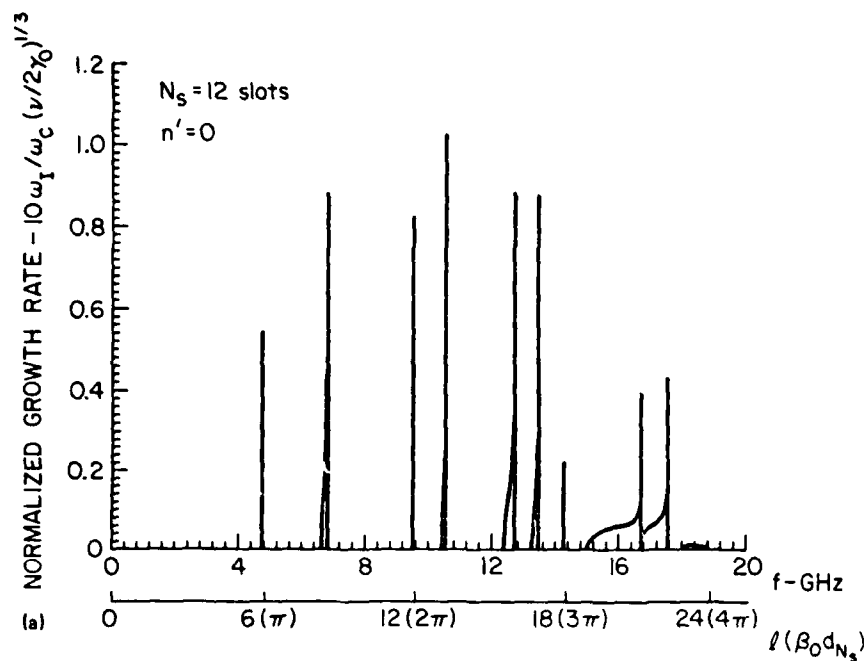


FIG. 4. Normalized TE growth rate [Eq. (19)] vs frequency f and equivalent harmonic number l for a 12 slot periodic planar waveguide with geometry the same as in Fig. 2 and beam parameters $\gamma_0 = 6$, $x_s = 1.0$ cm, and $f_s = \omega_c/2\pi = 0.8$ GHz. (a) $n' = 0$: zero-order slot mode; (b) $n' = 1$: first-order slot mode.

anode plane into the magnetic cusp transition region, where the $\mathbf{v}_\perp \times \mathbf{B}_r$ force efficiently converts axial particle velocity to azimuthal velocity downstream of the cusp transition. The details of particle motion in the cusp region are reported elsewhere,¹⁴ and it is easily shown that the downstream particle orbits are axis encircling with a gyroradius equal to the cathode radius. Typical downstream beam parameters are 2 MeV, 2 kA, and 5 ns, and the rotating E -layer moves through the downstream region with an axial velocity in the range 0.1–0.3 c . Thus, since the azimuthal velocity $v_\perp \approx c$, the ratio v_\perp/v_\parallel is in the range 3–10. The instantaneous ener-

gy spread in the electron beam is very small (less than 1%) as indicated from previous results.⁹ The magnetic field upstream and downstream of the cusp transition is in the range 1200–1400 G, with a resultant relativistic cyclotron frequency of about 770 MHz at 1350 G.

B. Radiation at $12\omega_c$

The rotating electron beam in the region downstream of the cusp transition interacts with an *outer* conducting slotted boundary as depicted in Fig. 7. It consists of 12 resonators ($N_s = 12$) having an outer radius R_o of 7.5 cm and an inner

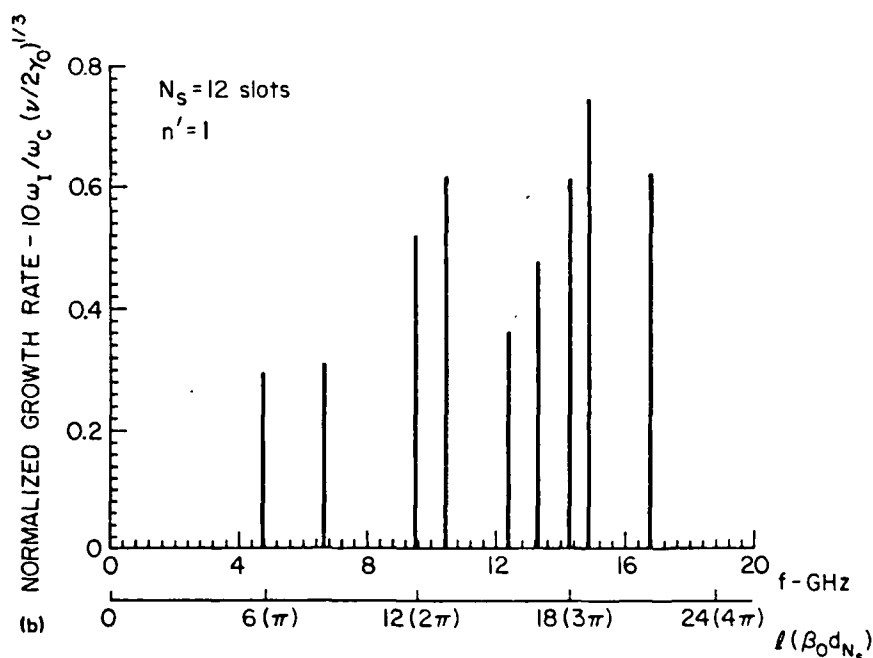
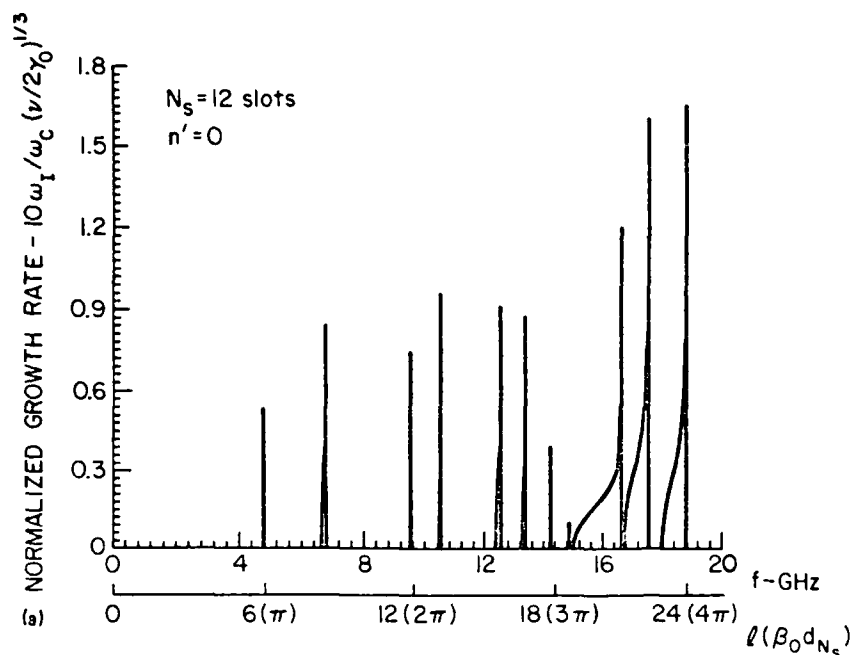


FIG. 5. Normalized TE growth rate [Eq. (19)] vs frequency f and equivalent harmonic number l for a 12 slot periodic planar waveguide with geometry the same as is Fig. 2 except $\omega_c = 0.785$ cm. The beam parameters are $\gamma_0 = 6$, $x_h = 1.0$ cm, and $f_0 = \omega_c/2\pi = 0.8$ GHz. (a) $n' = 0$; zero-order slot mode; (b) $n' = 1$ first-order slot mode.

radius of 6.5 cm, that is, the slot depth is 1 cm. No inner conducting boundary was used for these experiments. For comparison purposes, measurements were also made of the radiation produced when the beam interacts with a simple cylindrical outer conducting boundary of 7.5 cm radius. Details of the radiation production in this latter configuration have been reported elsewhere.^{9,10} Unlike a conventional magnetron, where radiation is usually extracted through a window in one of the resonators, radiation in this system was extracted axially out the downstream end of the drift chamber, as shown in Fig. 7. The downstream end of the

drift chamber was flared to provide a smooth transition to free space, and the radiated power was detected by a receiving horn and a 34-m X-band (8–12 GHz) dispersive line connected to a calibrated attenuator and a calibrated detector. Total power was obtained by determining the effective radiation area at a given axial position of the receiving horn (by carefully surveying the region to determine over what area radiation is produced) from the output end of the drift chamber and multiplying the measured radiated power at the detector by the ratio of this area to that of the receiving horn. The power spectrum of the radiation was determined

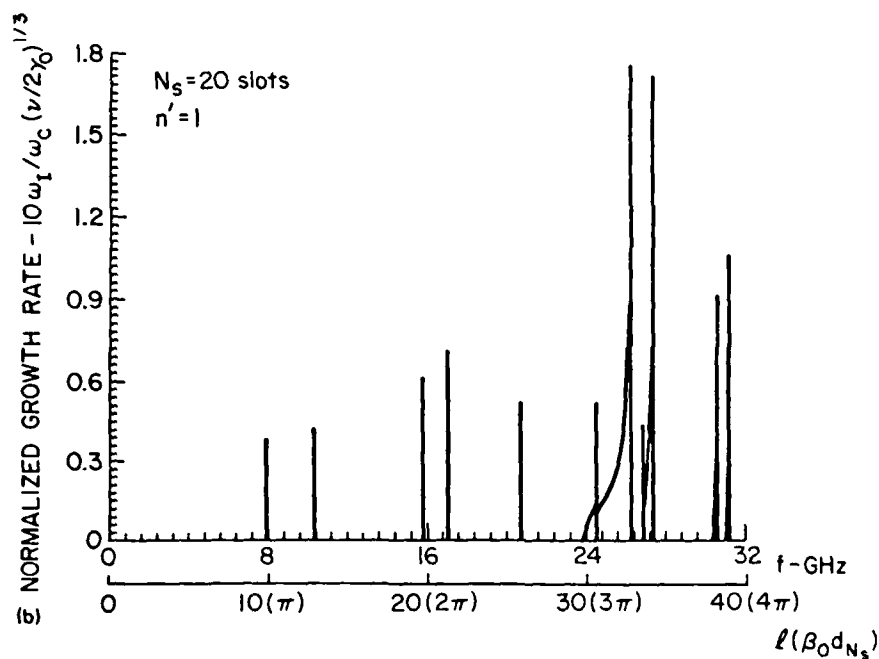
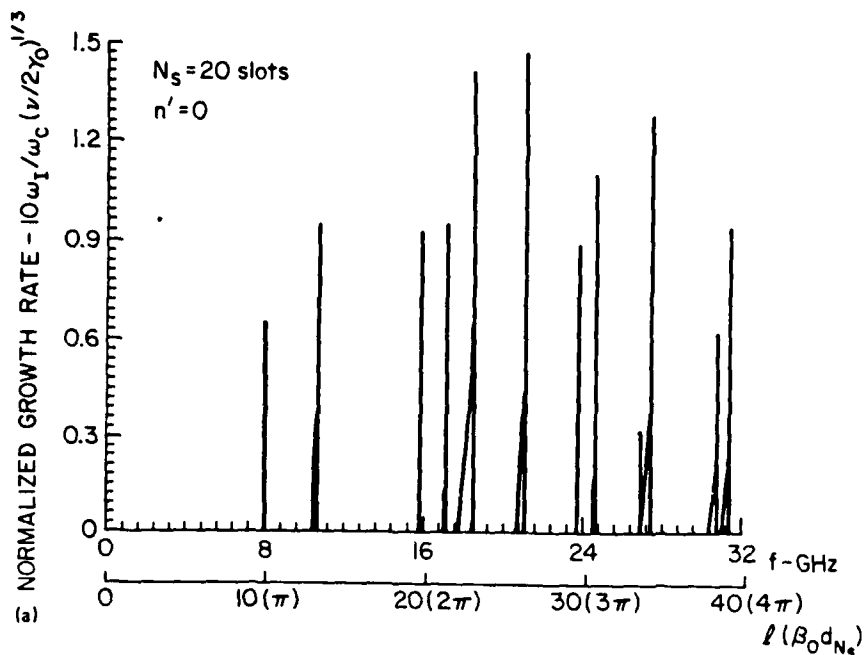


FIG. 6. Normalized TE growth rate [Eq. (19)] vs frequency f and equivalent harmonic number l for a 20 slot periodic planar waveguide with geometry the same as in Fig. 3 and beam parameters $\gamma_0 = 6$, $x_b = 1.0$ cm, and $f_c = \omega_c/2\pi = 0.8$ GHz. (a) $n' = 0$: zero-order slot mode; (b) $n' = 1$: first-order slot mode.

by making use of the frequency-dependent group velocity of the radiation down the dispersive line. The undispersed radiation pulse duration was measured to be about 5 ns.

Results of these measurements are shown in Fig. 8 both for the simple cylindrical outer boundary [Fig. 8(a)] and for the magnetron-type boundary [Fig. 8(b)]. Each spectrum was obtained from a single shot, with each point representing a peak in the dispersed radiation waveform reaching the detector. The magnetic field setting in each case was 1350 G. Shot to shot reproducibility using the magnetron boundary was about $\pm 5\%$ in frequency and about $\pm 20\%$ in power

amplitude. It is easily seen that both the total power and the spectrum of the emitted radiation are affected dramatically by the multiresonator boundary. For the simple outer boundary, the power is very broad band in the X-band frequency spectrum with peak powers around 200 kW. However, for the magnetron type boundary, the peak power is a factor of 1000 greater and occurs predominantly at a single frequency around 9.6 GHz. These results have been published previously.⁵

An indication of the strength of the resonant interaction is shown in Fig. 9, where the power produced at 9.6

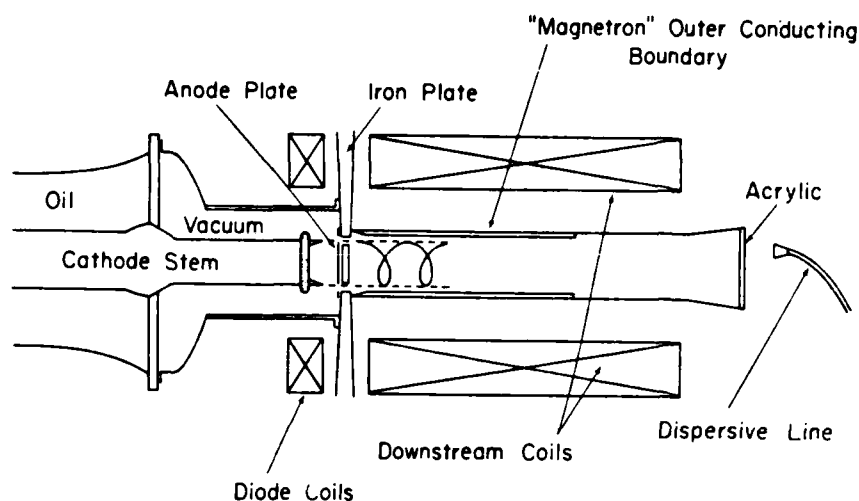


FIG. 7. General experimental configuration.

GHz is shown as a function of applied magnetic field. It is easily seen that only for magnetic fields close to 1350 G are these high powers obtained. The cusp cutoff field is the value above which the electrons no longer have sufficient energy to pass through the cusp.

C. Radiation at $20 \omega_c$

Because of the difficulty in machining outer magnetron-type conducting boundaries for operation at higher frequencies, these experiments were conducted using slotted inner conductors, as shown in Fig. 1(a). Outer magnetron boundaries should, however, be superior for long pulse oper-

ation of this device, because electrons move to smaller radii as they lose energy and may eventually collide with an inner boundary, producing plasma and breakdown difficulties. Apart from this change, the basic experimental configuration in this case was the same as that used for studies at $12 \omega_c$, except that radiation was monitored using a 36-m Ku band (12–18 GHz) dispersive line with associated attenuators and detectors.

Tracings of raw oscilloscope data obtained from the Ku-band dispersive line for a simple coaxial boundary system and a slotted inner $n = 20$ boundary system (of similar dimension) are shown in Fig. 10. It is easily seen that the broad band radiation observed in the unslotted boundary system is converted by the slotted boundary into higher power radiation at a single frequency. The attenuation values given include the correction for the fraction of the total area over which radiation is observed that is detected by the receiving horn, but do not include the frequency-dependent attenuation of the dispersive line. At 16 GHz, this attenuation is about 12 dB. As the burst duration is comparable to the pulse duration, the line bandwidth cannot be estimated accurately, although it is certainly less than 1 GHz. The best results obtained from these measurements are plotted in Fig. 11, and show the same characteristic behavior as the $12 \omega_c$ results, although the radiated power is lower. This is attri-

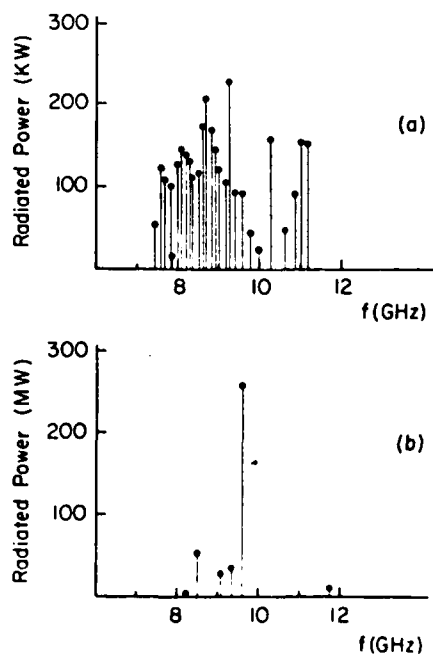


FIG. 8. Typical single shot power spectra for (a) simple cylindrical outer conducting boundary, $R_o = 7.5$ cm; (b) $V_r = 12$ multiresonator magnetron outer conducting boundary, $R_o = 7.5$ cm, $R_i = 6.5$ cm. Applied magnetic field is 1350 G in each case.

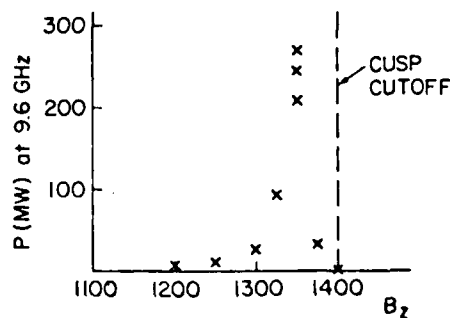


FIG. 9. Radiated power at 9.6 GHz plotted as a function of applied magnetic field.

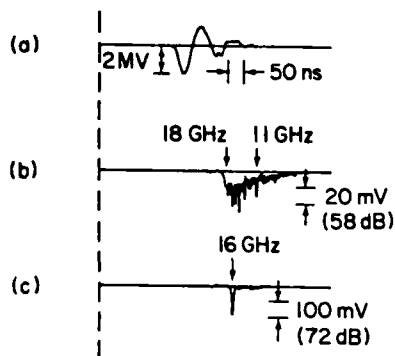


FIG. 10. Typical oscilloscope waveforms of (a) electron beam generator output voltage, (b) Ku band detector signal for rotating beam interacting with a simple coaxial boundary, $R_o = 7.0$ cm, $R_i = 5.0$ cm, (c) Ku band detector signal for a $N_i = 20$ slotted inner conductor, $R_o = 7.0$ cm, $R_i = 5.3$ cm, $d_i = 4$ mm, $\omega_i = 6.3$ mm.

butted to a somewhat lower injection current (1 kA compared to 1.5–2 kA in the $12\omega_c$ case) and to the fact that the fields in the slot cannot penetrate as far into the beam when the slots are smaller. It is also notable that this boundary was designed to operate with the “ 2π ,” $n' = 0$ modes only, while the $12\omega_c$ boundary may actually be resonating at a “ 2π ,” $n' = 1$ mode.

In these experiments, we have routinely monitored radiation in X-band as well. In the case where a system is effectively radiating in the “ 2π ” mode at 16 GHz, we do not observe any enhancement of radiation in X-band that might be associated with excitation of the “ π ” probe at 8 GHz. The

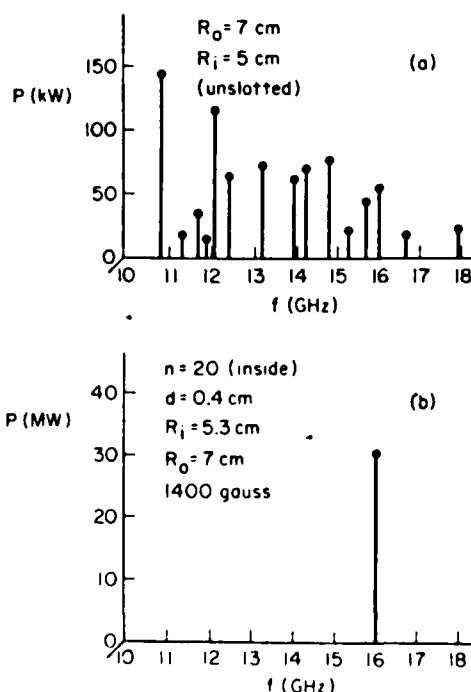


FIG. 11. Radiated power vs frequency (a) for the simple coaxial boundary, (b) for the $N_i = 20$ slotted inner conductor.

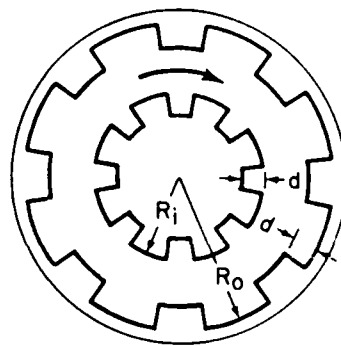


FIG. 12. Rotating beam propagating between slotted inner and outer boundaries.

observed radiation in X-band is more characteristic of that observed in an unslotted cylindrical boundary system.

We have also varied the slot depth to observe its effect on radiated power. As expected, unless the slot depth is set to a value such that a “ 2π ” resonance occurs near $N_i\omega_c$, peaking and enhancement of the radiated power spectrum at this frequency do not occur.

D. Radiation from “glide symmetric” boundaries

In this configuration, shown in Fig. 12, a rotating beam propagates between slotted boundaries with an effective 180° phase difference between inner and outer slots. In linear systems, such configurations are said to possess “glide reflection symmetry,” and theoretical analysis¹⁵ shows that as the two conductors are moved closer together, the effective periodicity of the system approaches half that possessed by either boundary. Thus, in principle, such a configuration might lead to higher frequency radiation. When a beam was injected into such a configuration, the radiation was moved into Ka band (26–40 GHz) and was measured using a 36-m-long Ka band dispersive line. Radiation was produced predominantly at 36 GHz, slightly greater than $40\omega_c$, and the radiated power spectrum is shown in Fig. 13. Theoretical analysis of this system is currently in progress.

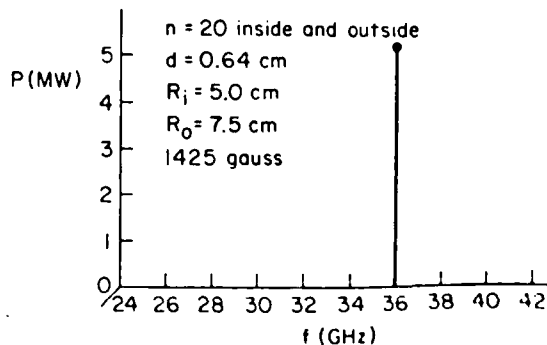


FIG. 13. Radiated power vs frequency for a rotating beam propagating between $N_i = 20$ slotted inner and outer boundaries, $R_o = 7.5$ cm, $R_i = 5.0$ cm, $d = 6.4$ mm.

IV. CONCLUSIONS

(1) Good qualitative agreement between theory and experiment has been achieved in these studies of the interaction of a rotating electron beam with a slotted wall waveguide structure that is placed either inside or outside of the electron beam.

(2) The slotted wall structures peak the radiation at selected frequencies versus the broad band nature of the radiation when a smooth wall structure is used. These selected frequencies are very close to the resonant frequencies where a beam mode intersects a waveguide mode.

(3) One would expect, because of the wall structure, that the beam would preferentially radiate at the 2π mode, that is, the beam harmonic l that equals the number of slots. This is true if there is an intersection of a beam wave and a waveguide mode at this location. Thus, by changing wall geometry, this required intersection can be achieved and radiation is observed near ω_c .

(4) In order that multi-moding be reduced, the $n' \gg 1$ slot mode cutoff frequency can be raised above the $n' = 0$ 2π mode by reducing the width of the slots, that is, making w_s/d_N smaller. At the same time, however, the volume of the slots is reduced, which may affect the total radiated energy. Multimoding due to electron beam properties is less likely in our system than in conventional cross-field devices, because there is almost no velocity shear across the beam. This velocity shear gives rise to many $\omega = \beta_0 V_0$ lines instead of the one we drew, that is, an angular region on the ω vs $\beta_0 d_N$ graph.

ACKNOWLEDGMENTS

We would like to acknowledge discussions in this work with K. R. Chu, J. Y. Choe, Y. Y. Lau, W. Namkung, M. J. Rhee, and H. S. Uhm. This work is supported by the Air Force Office of Scientific Research and the University of Maryland Computer Science Center.

- ¹V. A. Flyagin, A. V. Gapanov, M. I. Potelin, and V. V. Yulpatov, *IEEE Trans. Microwave Theory Tech.* **MTT-25**, 514 (1977).
- ²J. L. Hirschfield and V. L. Granatstein, *IEEE Trans. Microwave Theory Tech.* **MTT-25**, 528 (1977).
- ³H. S. Uhm, R. L. Davidson, and K. R. Chu, *Phys. Fluids* **21**, 1877 (1978).
- ⁴D. A. G. Deacon, L. R. Elias, J. M. M. Madey, G. J. Ramian, H. A. Schwettman, and T. I. Smith, *Phys. Rev. Lett.* **38**, 897 (1977).
- ⁵E. Ott and R. V. Lovelace, *Appl. Phys. Lett.* **27**, 378 (1975).
- ⁶G. Bekefi and T. J. Orzechowski, *Phys. Rev. Lett.* **37**, 379 (1976).
- ⁷A. Palevsky and G. Bekefi, *Phys. Fluids* **22**, 986 (1979).
- ⁸W. W. Destler, R. L. Weiler, and C. D. Striffler, *Appl. Phys. Lett.* **38**, 570 (1981).
- ⁹W. W. Destler, D. W. Hudgings, M. J. Rhee, S. Kawasaki, and V. L. Granatstein, *J. Appl. Phys.* **48**, 3291 (1977).
- ¹⁰W. W. Destler, H. Romero, C. D. Striffler, R. L. Weiler, and W. Namkung, *J. Appl. Phys.* **52**, 2740 (1981).
- ¹¹Y. Y. Lau and L. R. Barnett, *Int. J. Infrared Millimeter Waves* **3**, 619 (1982).
- ¹²Y. Y. Lau and L. R. Barnett, *Int. J. Electron.* **53**, 6 (1982).
- ¹³H. S. Uhm, C. M. Kim, and W. Namkung, *Phys. Fluids*, (to be published).
- ¹⁴M. J. Rhee and W. W. Destler, *Phys. Fluids* **17**, 1574 (1974).
- ¹⁵R. Mittra and S. Laxpati, *Can. J. Phys.* **43**, 353 (1965).
- ¹⁶G. B. Collins, *Microwave Magnetrons* (McGraw-Hill, New York, 1948), p. 56.

Observation of microwave generation from a cusptron device

Won Namkung

Electrical Engineering Department, University of Maryland, College Park, Maryland 20742

(Received 18 October 1983; accepted 14 November 1983)

The first observation of microwave generation at the sixth harmonic of the electron cyclotron frequency using a 17 kV, 0.6–1.0 A, 3 μ sec electron beam is reported. This device, which is called a cusptron, produces radiation from the resonant interaction of a nonrelativistic rotating electron beam and a magnetron-type conducting boundary with six vanes by the negative mass instability. The observed radiated power is approximately 500 W at 4.38 GHz.

There have been numerous experimental and theoretical studies of high-power and high-frequency microwave devices such as gyrotrons,^{1–3} relativistic magnetrons,⁴ and free electron lasers.^{5,6} High-power microwaves have been also produced by the resonant interaction of a relativistic rotating electron layer (*E* layer) with the modes of various conducting boundary systems by the negative-mass instability.^{7–11} To date, these devices have been operated using high magnetic fields and/or high electron energies. The device which we report here operates at low electron energy, and, since it produces radiation by the negative mass instability at a high harmonic of the electron cyclotron frequency, uses very low applied magnetic fields.

One of the simplest ways to produce a rotating *E* layer involves the use of a magnetic cusp field through which an annular electron beam is injected. After the cusp transition region, an annular beam becomes an axis-rotating beam propagating downstream with the same radius as the cathode. The name cusptron originates from the use of a magnetic cusp field to produce a rotating *E* layer and the magnetron-type conducting boundary for a beam-wave interaction.^{12,13} The axis-encircling electrons are bunched azimuthally by the negative mass instability and the beam energy is thereby transferred to the wave energy. Recent theoretical studies^{14,15} on this device have shown that effective

microwave generation can be expected over a wide range of electron energies. A cusptron operated in the nonrelativistic regime holds promise as a practical and compact microwave tube with low magnetic fields. In this paper, we report preliminary results of a cusptron experiment operated at the sixth harmonic of the electron cyclotron frequency.

The experimental setup and the magnetic field distribution are shown schematically in Fig. 1. The magnetic cusp field is produced by two independently controlled coils on the diode side and by a long solenoid on the downstream side. The transition width of the cusp is narrowed substantially by a soft iron plate placed between the solenoids. The cusp transition length has been measured as 0.5 cm, which is determined by the FWHM value of the radial magnetic field at the beam radius. The system vacuum is maintained by two 30 ℓ /sec ion pumps at $2\text{--}5 \times 10^{-8}$ Torr.

A hollow electron beam is emitted from an annular thermionic cathode of 1.4 cm inner radius and 1.6 cm outer radius with a Pierce-type focusing electrode. The cathode assembly is mounted on a bellows coupled pipe for its alignment and the cathode-anode gap adjustment can be made without breaking the system vacuum. A typical cathode-anode gap is 6 cm. An anode with an annular slit is attached to the iron plate. A 0.2 cm wide circular slit in the anode plate allows an annular electron beam to pass through the magnetic cusp transition region, where the $\mathbf{v}_z \times \mathbf{B}$ force converts axial velocity to azimuthal velocity downstream of the cusp transition. The details of electron motion in a cusp region may be found in Refs. 16 and 17.

The conducting boundary in the beam-wave interacting region has six equally spaced vanes of $R_a = 1.84$ cm inner radius and $R_c = 3.68$ cm outer radius. The dispersion relation of the fundamental mode (2π mode) becomes

$$\omega^2/c^2 - k_z^2 = \eta^2/R_a^2.$$

For these values, $\eta = 1.656$, and the cutoff frequency is $\omega_c = (2\pi)4.297$ GHz. These parameters are obtained from theoretical studies¹⁴ for a resonant interaction of the 2π mode with a beam of radius 1.6 cm and a beam energy of 17 keV due to the limitation of the available high voltage power supply. Under this limited electron energy, we can operate this device with a magnetic cusp field up to 280 G.

In radiation measurement experiments, we fix the diode parameters at 17 kV, 0.6–1.0 A, 3 μ sec, 60 pps. and the magnetic field near the cathode at 220 G. The downstream magnetic field is continuously varied. The radiated power signal

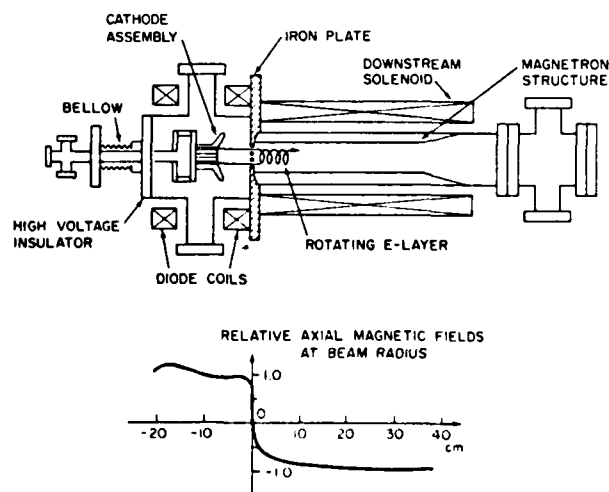


FIG. 1. Schematic of the cusptron experiment and the axial magnetic field distribution at $r = 1.5$ cm (in relative units).

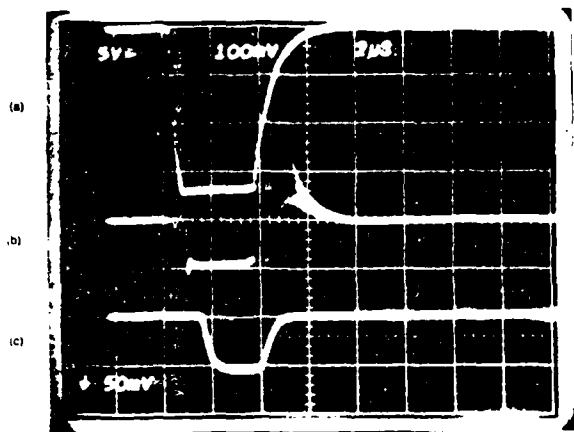


FIG. 2. Oscilloscope traces of (a) beam voltage (5 kV/div), (b) diode current (1 A/div), and (c) detector signal (100 mV/div).

from a C band (3.95–5.85 GHz) detector responds sharply only in a narrow region of the downstream magnetic field. Typical microwave power detected is approximately 500 W and the microwave frequency measured by a spectrum analyzer is 4.38 GHz with an 8 MHz bandwidth. Figure 2 shows typical oscilloscope traces of the beam voltage, diode current, and detector signal. The detected frequency corresponds to the sixth harmonic of the electron cyclotron frequency at a magnetic field of only 260 G. The resonant interaction takes place only about 2.5 cm downstream from the iron plate, since the downstream flat field shown in Fig. 1 is 400 G. The conversion efficiency between the power detected by the receiving antenna and the diode power is approximately 3%–4%. It is possible that the efficiency of radiation production could be much higher, since a fraction of the electron beam intercepts the anode plate.

In conclusion, about 500 W of microwave radiation at 4.38 GHz has been generated by the interaction of a nonrelativistic rotating E layer with an $N = 6$ magnetron-type conducting boundary. The diode is operated at 17 kV, 0.6–1.0 A, and 3 μ sec. This experiment has successfully demonstrated

that high harmonic microwave generation can be produced from a nonrelativistic cusptron device. This device holds promise as an efficient, compact microwave tube suitable for many practical applications.

ACKNOWLEDGMENTS

The author would like to acknowledge useful discussions with M. J. Rhee, H. S. Uhm, and W. W. Destler. Important technical support was provided by W. Lawson, D. Byun, M. Naimann, J. Rehwinkel, A. Bromborsky, J. Choe, and A. Krall.

This work was supported by the Air Force Office of Scientific Research and the University of Maryland Computer Science Center.

- ¹V. A. Flyagin, A. V. Gapanov, M. I. Petelin, and V. K. Yulpatov, IEEE Trans. Microwave Theory Tech. MTT-25, 514 (1977).
- ²J. L. Hirschfield and V. L. Granatstein, IEEE Trans. Microwave Theory Tech. MTT-25, 528 (1977).
- ³H. S. Uhm, R. C. Davidson, and K. R. Chu, Phys. Fluids 21, 1877 (1978).
- ⁴A. Palevsky and G. Bekefi, Phys. Fluids 22, 986 (1979).
- ⁵D. A. G. Deacon, L. R. Elias, J. M. M. Madey, G. J. Ramian, H. A. Schwettman, and T. I. Smith, Phys. Rev. Lett. 38, 897 (1977).
- ⁶H. S. Uhm and R. C. Davidson, Phys. Fluids 24, 1541 (1981).
- ⁷W. W. Destler, D. W. Hudgings, M. J. Rhee, S. Kawasaki, and V. L. Granatstein, J. Appl. Phys. 48, 3291 (1977).
- ⁸W. W. Destler, H. Romero, C. D. Striffler, R. L. Weiler, and W. Namkung, J. Appl. Phys. 52, 2740 (1981).
- ⁹W. W. Destler, R. L. Weiler, and C. D. Striffler, Appl. Phys. Lett. 38, 570 (1981).
- ¹⁰W. W. Destler, R. Kulkarni, C. D. Striffler, and R. L. Weiler, J. Appl. Phys. 54, 4152 (1983).
- ¹¹D. B. McDermott, N. C. Luhmann, Jr., A. Kupiszewski, and H. R. Jory, Phys. Fluids 26, 1936 (1983).
- ¹²W. W. Destler, D. Calderone, R. Kulkarni, W. Namkung, R. Weiler, and C. D. Striffler, presented at the 1982 IEEE International Conference on Plasma Science, 17–19 May 1982, Ottawa, Canada, paper 2p3.
- ¹³W. Namkung, W. W. Destler, W. Lawson, and C. D. Striffler, Bull. Am. Phys. Soc. 27, 1062 (1982).
- ¹⁴H. S. Uhm, C. M. Kim, and W. Namkung, Phys. Fluids 27, 487 (1984).
- ¹⁵Y. Y. Lau and L. R. Barnett, Int. J. Infrared Millimeter Waves 3, 619 (1982).
- ¹⁶M. J. Rhee and W. W. Destler, Phys. Fluids 17, 1574 (1974).
- ¹⁷W. W. Destler and M. J. Rhee, Phys. Fluids 20, 1582 (1977).

Linear theory of cusptron microwave tubes

Han S. Uhm and Chung M. Kim

Naval Surface Weapons Center, White Oak, Silver Spring, Maryland 20910

Won Namkung

The Electrical Engineering Department, University of Maryland, College Park, Maryland 20742

(Received 2 November 1982; accepted 22 September 1983)

Stability properties of the negative-mass instability in a rotating annular electron beam (E layer) are investigated, in connection with applications on the cusptron microwave tubes. The analysis is carried out for an infinitely long E layer propagating through a magnetron-type conducting wall and propagating parallel to an applied axial magnetic field. It is assumed that the E layer is thin and very tenuous. A closed algebraic dispersion relation of the negative-mass instability is obtained, including the important influence of conducting boundaries on the mode control in microwave generation and amplification. It is shown that for typical present experimental beam parameters, the gain of the cusptron normalized to the excitation frequency can be comparable to that of the gyrotron. Moreover, under the appropriate geometric configuration, perturbations with azimuthal mode number N are dominantly unstable. This optimizes the microwave power output of the radiation with frequency $\omega \simeq N\omega_c$, where ω_c is the electron cyclotron frequency and N is the resonator number in the conducting wall.

I. INTRODUCTION

In recent years, there have been numerous experimental and theoretical investigations on high-power and high-frequency microwave devices such as gyrotrons,¹⁻³ relativistic magnetrons,⁴ and free electron lasers.^{5,6} High-power microwaves also have been produced by the negative-mass instability⁷⁻¹⁰ of a relativistic rotating electron layer (E layer) in a conducting waveguide. This relatively new scheme of microwave generation by a rotating E layer has many attractive features in practical application. Using a mode control scheme currently under investigation,¹¹ for example, this device could be a tunable, high-frequency microwave tube with low magnetic fields. One of the simple ways to produce a rotating E layer is to use a magnetic cusp field, through which an annular electron beam becomes a rotating electron layer.¹² After passing through a cusped magnetic field, a nonrelativistic E layer propagates through a conventional magnetron-type conducting wall. The name "cusptron" originates from the cusp and the magnetron. In this paper, we investigate the negative-mass stability properties of the E layer in a magnetron-type conductor, in connection with the application to the cusptron microwave tube.

In recent literature,¹³ Lau and Barnett have also studied the negative-mass stability properties in a similar physical configuration. However, their analysis has been restricted to infinite axial wavelength perturbations. In an electron beam propagating through any oscillator or amplifier with its axial velocity $\beta_z c \hat{e}_z$, the influence of the finite axial wavelength perturbation on the stability behavior is dominantly important in determining the necessary physical parameters, to optimize the gain, the bandwidth, and the efficiency of the microwave tubes. For example, as will be seen in Sec. IV, in an optimized cusptron amplifier, the maximum growth of the microwave signal occurs at a nonzero axial wavenumber perturbation (i.e., $k \neq 0$). Moreover, the infinite axial wavelength perturbations ($k = 0$) do not grow for the

optimized conditions, indicating no amplification in these physical parameter regimes, which is particularly important for a stable operation of the microwave amplifier. In this regard, we investigate the negative-mass stability properties of the E layer, including the important influence of the finite axial wavelength perturbations on the stability behavior and determining all the optimum conditions of the cusptron microwave tubes. Most critical parameters are determined from the grazing condition in Eqs. (52) and (53). The grazing condition dominates the nature of the dispersion relations in Eqs. (47) and (48), changing them from a second-order to a third-order polynomial, and maximizing the growth rate, the bandwidth, and the efficiency of the cusptron microwave tubes.

The stability analysis of the negative-mass instability is carried out for an E layer with radius R_0 propagating through a magnetron-type conductor with its inner- and outermost radii R_i and R_o , respectively. Equilibrium and stability properties are calculated for the electron distribution function [Eq. (1)] in which all electrons have the same energy and the same canonical angular momentum but a Lorentzian distribution in the axial canonical momentum. The stability analysis is calculated within the framework of the linearized Vlasov-Maxwell equations for an infinitely long E layer propagating parallel to an applied magnetic field $B_0 \hat{e}_z$, with an axial velocity $\beta_z c \hat{e}_z$. We assume that the E layer is thin and very tenuous. The formal dispersion relation [Eq. (29)] of the negative-mass instability is obtained in Sec. II, including the important influence of conducting boundaries on the mode control in microwave amplification and generation.

In Sec. III, properties of the vacuum dispersion relation in a magnetron-type conductor are investigated without including the influence of beam electrons. It is shown that the vacuum dispersion relation reduces to three distinct modes; the transverse electric (TE), the transverse magnetic (TM),

and the magnetron TE modes. From numerical calculation, the cutoff frequency $\omega_{cl} = \eta c/R_a$ is obtained in terms of the ratio R_c/R_a . In Sec. IV, the negative-mass stability properties of an E layer are numerically investigated. Several points are noteworthy from the numerical calculation for a nonrelativistic cusptron. First, optimum coupling occurs between the beam and the fundamental 2π modes. It is shown for the fundamental 2π mode that for typical present experimental beam parameters, gain of the cusptron normalized by the excitation frequency can be comparable to that of the gyrotron. Second, for the applied magnetic field satisfying the grazing condition of the $l = N$ perturbations, other azimuthal perturbations with $l \neq N$ are suppressed. Here l is the azimuthal harmonic number of perturbations and N is the number of resonators in the magnetron-type conductor. Under this grazing condition, the $l = N$ mode perturbation is the dominant unstable mode, optimizing the microwave power output for radiation with frequency $\omega \simeq l\omega_c$. Therefore, even for relatively low magnetic field, a high-frequency microwave can be amplified by making use of the cusptron with $N \geq 2$. Finally, the growth rate and Doppler-shifted real oscillation frequency are substantially increased by changing the applied field index from zero to a small positive value. Preliminary investigation of a relativistic cusptron amplifier is also carried out in Sec. IV.

II. VLASOV-MAXWELL THEORY

As illustrated in Fig. 1, the equilibrium configuration consists of a nonneutral electron layer (E layer) that is infinite in axial extent and aligned parallel to an applied magnetic field $B_0(r)\hat{e}_z$. The electron layer is accomplished by the passing of a hollow electron beam through an ideal cusp magnetic field.¹² Therefore, the electron layer is in a fast rotational equilibrium, where all electrons have positive canonical angular momentum. The mean radius of the E layer is denoted by R_0 . We also assume that the radial thickness of the E layer is $2a$ which is much less than the equilibrium radius R_0 , i.e., $a \ll R_0$. The mean motion of the E layer is in

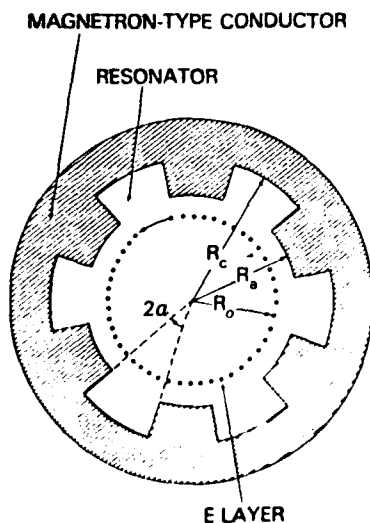


FIG. 1. Cross-sectional view of cusptron.

the azimuthal direction, and the applied magnetic field provides radial confinement of the electrons. As shown in Fig. 1, the outer conductor is a magnetron-type configuration with its inner- and outermost radii R_c and R_a , respectively. The angle of the open spaces in the magnetron-type conductor is denoted by 2α . In the theoretical analysis, cylindrical polar coordinates (r, θ, z) are employed. In the present analysis, we assume that $v/\hat{\gamma} \ll 1$, where $v = N_e e^2/mc^2$ is Budker's parameter and $\hat{\gamma}mc^2$ is the electron energy. Here N_e is the total number of electrons per unit axial length, and $-e$ and m are the charge and rest mass of electrons, respectively. Consistent with the low-density assumption, we neglect the influence of equilibrium self-fields.

In the present analysis, we investigate the equilibrium and stability properties for the choice of equilibrium distribution function:

$$f_b^0(H, P_\theta, P_z) = \frac{\omega_c N_e \hat{p}_z \Delta}{4\pi^3 mc^2} \frac{\delta(\gamma - \hat{\gamma}) \delta(P_\theta - P_0)}{(P_z - \hat{p}_z)^2 + \hat{p}_z^2 \Delta^2}, \quad (1)$$

where $H = \gamma mc^2 = (m^2 c^4 + c^2 p^2)^{1/2}$ is the total energy, P_z is the axial canonical momentum, $P_\theta = r[p_\theta - (e/c)A_\theta(r)]$ is the canonical angular momentum, $\omega_c = eB_0(R_0)/\hat{\gamma}mc$ is the electron cyclotron frequency, $A_\theta(r)$ is the azimuthal component of the equilibrium vector potential, $P_0 = (e/c)R_0 A_\theta(R_0) = (e/2c)R_0^2 B_0(R_0)$, and $\hat{\gamma}$, \hat{p}_z , and Δ are constants.

In the subsequent stability analysis, we examine the linearized Vlasov-Maxwell equations for perturbations about a thin E -layer equilibrium described by Eq. (1). To calculate stability quantities of the E layer, we adopt a normal-mode approach in which all E -layer perturbations are assumed to vary with time and space according to

$$\delta\psi(\mathbf{x}, t) = \psi_l(r) \exp[i(l\theta + kz - \omega t)],$$

where $\text{Im } \omega > 0$. Here, ω is the complex eigenfrequency, k is the axial wavenumber, and l is the azimuthal harmonic number. The Maxwell equations for the perturbed electric and magnetic field amplitudes can be expressed as

$$\begin{aligned} \nabla \times \hat{\mathbf{E}}(\mathbf{x}) &= i(\omega/c) \hat{\mathbf{B}}(\mathbf{x}), \\ \nabla \times \hat{\mathbf{B}}(\mathbf{x}) &= (4\pi/c) \hat{\mathbf{J}}(\mathbf{x}) - i(\omega/c) \hat{\mathbf{E}}(\mathbf{x}), \end{aligned} \quad (2)$$

where $\hat{\mathbf{E}}(\mathbf{x})$ and $\hat{\mathbf{B}}(\mathbf{x})$ are the perturbed electric and magnetic fields,

$$\hat{\mathbf{J}}(\mathbf{x}) = -e \int d^3p \, \mathbf{v} f_b(\mathbf{x}, \mathbf{p}) \quad (3)$$

is the perturbed current density,

$$\begin{aligned} \hat{f}_b(\mathbf{x}, \mathbf{p}) &= e \int_{-\infty}^{\infty} d\tau \exp(-i\omega\tau) \\ &\times \left(\hat{\mathbf{E}}(\mathbf{x}') + \frac{\mathbf{v}' \times \hat{\mathbf{B}}(\mathbf{x}')}{c} \right) \frac{\partial}{\partial \mathbf{p}} f_b^0, \end{aligned} \quad (4)$$

is the perturbed distribution function, and $\tau = t' - t$.

From Eq. (2), it is straightforward to show that

$$\frac{\partial}{\partial r} \hat{B}_{\theta}(r) - i \frac{c}{\omega} \left(p^2 \hat{E}_{\theta}(r) + \frac{lk}{r} \hat{E}_{\theta}(r) \right) = - \frac{4\pi}{c} \hat{J}_{\theta}(r), \quad (5)$$

where

$$p^2 = \omega^2/c^2 - k^2. \quad (6)$$

For the present purposes, we assume that

$$|\Omega| = |\omega - l\omega_c - k\beta_z c| \ll \omega_c, \quad la \ll R_0, \quad (7)$$

where $\beta_z = \hat{p}_z/\gamma mc$ and c is the speed of light in *vacuo*. The perturbed axial and azimuthal electric fields $[\hat{E}_{1\theta}(r)$ and $\hat{E}_{1z}(r)]$ are continuous across the beam boundaries ($r = R_1$ and $r = R_2$). Here $R_1 = R_0 - a$ and $R_2 = R_0 + a$ are the inner and outer boundaries of the E layer, respectively. Moreover, within the context of Eq. (7), it is valid to approximate

$$\hat{E}_{1\theta}(R_1) \simeq \hat{E}_{1\theta}(R_0) \simeq \hat{E}_{1\theta}(R_2), \quad (8)$$

$$\hat{E}_{1z}(R_1) \simeq \hat{E}_{1z}(R_0) \simeq \hat{E}_{1z}(R_2).$$

Integrating Eq. (5) from $r = R_1 - \delta$ to $r = R_2 + \delta$ and taking the limit $\delta \rightarrow 0_+$, we obtain

$$\hat{B}_{1z}(R_2^+) - \hat{B}_{1z}(R_1^-) = -\frac{4\pi}{c} \int_{R_1}^{R_2} dr \hat{J}_{1\theta}(r), \quad (9)$$

where $\psi(R_j^\pm)$ denotes $\lim_{\delta \rightarrow 0} \psi(R_j \pm \delta)$. Similarly, the discontinuity of the azimuthal component of the perturbed magnetic field is given by

$$\hat{B}_{1\theta}(R_2^+) - \hat{B}_{1\theta}(R_1^-) = \frac{4\pi}{c} \int_{R_1}^{R_2} dr \hat{J}_{1z}(r). \quad (10)$$

For convenience in the subsequent analysis, we introduce the normalized electric and magnetic wave admittances,¹⁴ d_\pm and b_\pm , defined at the inner and outer surfaces of the E layer by

$$d_+ = \frac{-[r(\partial/\partial r)\hat{E}_{1z}(r)]_{R_2^+}}{l\hat{E}_{1z}(R_2)}, \quad (11)$$

$$d_- = \frac{[r(\partial/\partial r)\hat{E}_{1z}(r)]_{R_1^-}}{l\hat{E}_{1z}(R_1)},$$

and

$$b_+ = \frac{-l\hat{B}_{1z}(R_2^+)}{[r(\partial/\partial r)\hat{B}_{1z}(r)]_{R_2}}, \quad (12)$$

$$b_- = \frac{l\hat{B}_{1z}(R_1^-)}{[r(\partial/\partial r)\hat{B}_{1z}(r)]_{R_1}}.$$

From Eq. (2), it is straightforward to show that

$$\frac{\partial}{\partial r} \hat{B}_{1z}(r) = i \frac{c}{\omega} \left(p^2 \hat{E}_{1\theta}(r) + \frac{lk}{r} \hat{E}_{1z}(r) \right),$$

$$\hat{B}_{1\theta}(r) = -\frac{kl}{p^2 r} \hat{B}_{1z}(r) + \frac{i\omega}{cp^2} \frac{\partial}{\partial r} \hat{E}_{1z}(r), \quad (13)$$

outside the E layer and the radial coordinate r satisfying $r < R_0$. Substituting Eq. (13) into Eqs. (9) and (10) and making use of Eqs. (11) and (12) we obtain

$$(b_- + b_+) [p^2 R_0 \hat{E}_{1\theta}(R_0) + kl \hat{E}_{1z}(R_0)]$$

$$= -i \frac{4\pi\omega l}{c^2} \int_{R_1}^{R_2} dr \hat{J}_{1\theta}(r), \quad (14)$$

$$(d_- + d_+) \hat{E}_{1z}(R_0)$$

$$= -i \frac{4\pi k}{\omega} \int_{R_1}^{R_2} dr \hat{J}_{1\theta}(r) + i \frac{4\pi p^2 R_0}{\omega l} \int_{R_1}^{R_2} dr \hat{J}_{1z}(r),$$

where use has been made of Eq. (8). Evidently, an evaluation of the azimuthal and axial components of the perturbed current density ($\hat{J}_{1\theta}$ and \hat{J}_{1z}) is required for a detailed stability analysis.

A. Perturbed current density

In this section, we evaluate the perturbed distribution function and subsequently the perturbed current density. As indicated in Eq. (4), the particle trajectories, $r'(\tau)$, $\theta'(\tau)$, and $z'(\tau)$, in the equilibrium fields are required in order to evaluate the perturbed distribution function. The applied axial magnetic field $B_0(r)\hat{e}_z$ is approximated by

$$B_0(r) = B_0(R_0)(1 - n\rho/R_0), \quad (15)$$

where $\rho = r - R_0$ and

$$n = -\frac{R_0}{B_0(R_0)} \left(\frac{\partial}{\partial r} B_0(r) \right)_{R_0} \quad (16)$$

is the magnetic field index. Therefore, the azimuthal component of the vector potential is expressed as

$$rA_\theta(r) = R_0 A_\theta(R_0) + B_0(R_0) \int_{R_0}^r dr r \left(1 - \frac{n\rho}{R_0} \right). \quad (17)$$

Making use of the Hamiltonian $H = \gamma mc^2 = (m^2 c^4 + c^2 p^2)^{1/2}$, the canonical angular momentum $P_\theta = r[p_\theta - (e/c)A_\theta(r)]$, and Eq. (17), we obtain the electron trajectories¹⁵

$$\rho' = r' - R_0 = \omega_c \delta P_\theta / \gamma \omega^2 R_0 + A_r \sin(\omega_r \tau + \phi),$$

$$z' = z + p_z \tau / \gamma m, \quad (18)$$

$$\dot{\theta}' = \omega_c - \mu (\delta P_\theta / \gamma m R_0^2) + (\omega_c / R_0) \rho',$$

where

$$\mu = (\omega_c^2 / \omega_r^2) - (1/\gamma_\theta^2), \quad (19)$$

$$\omega_r^2 = (1 - n)\omega_c^2 \quad (20)$$

is the radial betatron frequency squared of electrons, $\gamma_\theta = (1 - \beta_\theta^2)^{-1/2}$ is the relativistic mass ratio associated with the azimuthal electron velocity $\beta_\theta c$, A_r is the amplitude for radial betatron oscillations, $\delta P_\theta = P_\theta - P_0$, and $\tau = t' - t$. Within the context of Eq. (7), it is valid to approximate

$$\dot{\theta}' = \omega_c - \mu (\delta P_\theta / \gamma m R_0^2), \quad (21)$$

and to neglect the small oscillatory term $\omega_c \rho' / R_0$.

After a simple algebraic manipulation that makes use of Eq. (7), the perturbed distribution function in Eq. (4) is approximated by^{14,15}

$$\hat{f}_b = eI \left\{ \left[\left(1 - \frac{kV_z}{\omega} \right) R_0 \hat{E}_{1\theta}(R_0) + \frac{lV_z}{\omega} \hat{E}_{1z}(R_0) \right] \frac{\partial}{\partial P_\theta} f_b^0 \right.$$

$$\left. + \left[\frac{kV_\theta}{\omega} \hat{E}_{1\theta}(R_0) + \left(1 - \frac{lV_\theta}{\omega R_0} \right) \hat{E}_{1z}(R_0) \right] \frac{\partial}{\partial P_z} f_b^0 \right\}, \quad (22)$$

where the orbit integral I is defined by

$$I = \int_{-\infty}^0 d\tau \exp[i\{l(\theta' - \theta) + k(z' - z) - \omega\tau\}] \\ = i \left(\omega - l\omega_c - \frac{k p_z}{\gamma m} + l\mu \frac{\delta P_\theta}{\gamma m R_0^2} \right)^{-1}, \quad (23)$$

and use has been made of Eq. (8). Substituting Eq. (23) into Eq. (22) and carrying out a tedious but straightforward algebra, we obtain the perturbed distribution function

$$\hat{f}_b = i \frac{ec}{\gamma m R_0^2 \omega} \frac{l^2 \mu - k^2 R_0^2}{(\omega - l\omega_c - k\beta_z c)^2} \\ \times [\beta_\theta \hat{E}_{\theta\theta}(R_0) + \beta_z \hat{E}_{zz}(R_0)]. \quad (24)$$

Subsequently, integrals of the perturbed current density in the left-hand side of Eq. (14) are given by

$$\int_{R_1}^{R_2} dr \hat{J}_{\theta\theta}(r) = \frac{\beta_\theta}{\beta_z} \int_{R_1}^{R_2} dr \hat{J}_{zz}(r) \\ = -i \frac{\omega_c c \sigma}{2\pi\omega} [\beta_\theta \hat{E}_{\theta\theta}(R_0) + \beta_z \hat{E}_{zz}(R_0)], \quad (25)$$

where the effective susceptibility σ is defined by

$$\sigma(\omega, k) = \frac{\nu}{\gamma} \frac{c^2}{R_0^2} \frac{l^2 \mu - k^2 R_0^2}{(\omega - l\omega_c - k\beta_z c + i|k|[\beta_z c \gamma \Delta / \gamma_z^2])^2}, \quad (26)$$

and $\nu = N_b e^2 / mc^2$ is Budker's parameter.

Substituting Eq. (25) into Eq. (14), we obtain the matrix equation relating $\hat{E}_{\theta\theta}(R_0)$ and $\hat{E}_{zz}(R_0)$. The condition for a nontrivial solution to this matrix equation is that the determinant of the matrix vanishes. This gives the general dispersion relation

$$\frac{2}{lp^2 c^2} \left(\frac{l^2 \omega_c^2}{b_- + b_+} - \frac{(kc - \beta_z \omega)^2}{d_- + d_+} \right) \sigma + 1 = 0, \quad (27)$$

where use has been made of the approximation $\omega \simeq l\omega_c + k\beta_z c$, which is consistent with Eq. (7). Defining the geometric factor $\Gamma(\omega, k)$,

$$\Gamma(\omega, k) = \frac{lp^2 c^2}{2} \left(\frac{l^2 \omega_c^2}{b_- + b_+} - \frac{(kc - \beta_z \omega)^2}{d_- + d_+} \right)^{-1}, \quad (28)$$

and substituting Eq. (26) into Eq. (27), the dispersion relation in Eq. (27) is expressed as

$$\Gamma(\omega, k) = -\frac{\nu}{\gamma} \frac{c^2}{R_0^2} \frac{l^2 \mu - k^2 R_0^2}{(\omega - l\omega_c - k\beta_z c + i|k|[\beta_z c \gamma \Delta / \gamma_z^2])^2}, \quad (29)$$

which can be used to determine the complex eigenfrequency $\Omega = \omega - l\omega_c - k\beta_z c$ in terms of various physical parameters.

B. Geometric factor $\Gamma(\omega, k)$

The evaluation of the wave admittances at the boundaries of the E layer is required in order to complete the dispersion relation. To make the theoretical analysis tractable, in the subsequent analysis, we concentrate the lowest modes of the electromagnetic waves inside the resonator where $R_a < r < R_c$. Moreover, the previous studies^{16,17} have exhibited that the lowest modes in the resonator dominate the wave interaction. In this regard, for the transverse magnetic

(TM) mode, we select (see the Appendix)

$$\hat{E}_z(r) = 0, \quad R_a < r < R_c, \quad (30)$$

which is the lowest mode properly satisfying all the necessary boundary conditions. The Maxwell equations of the TM mode in the region $0 < r < R_a$ can be expressed as

$$\left(\frac{1}{r} \frac{\partial}{\partial r} r \frac{\partial}{\partial r} - \frac{l^2}{r^2} + p^2 \right) \hat{E}_{\theta\theta}(r) = 0, \quad (31)$$

except the inside of the E layer (i.e., $R_1 < r < R_2$). Here $p^2 = \omega^2/c^2 - k^2$ is defined in Eq. (6). The physically acceptable solutions to Eq. (31) are given by

$$\hat{E}_{\theta\theta}(r) = \begin{cases} AJ_l(pr), & 0 < r < R_1, \\ B \left(J_l(pr) - \frac{J_l(\eta)N_l(pr)}{N_l(\eta)} \right), & R_2 < r < R_a, \end{cases} \quad (32)$$

where $J_l(x)$ and $N_l(x)$ are Bessel functions of the first and second kind, respectively, the parameter η is defined by

$$\eta^2 = (\omega^2/c^2 - k^2)R_a^2, \quad (33)$$

and A and B are constants. Substituting Eq. (32) into Eq. (11) and carrying out a straightforward algebra with $a \ll R_0$, we obtain a sum of the electric wave admittance:

$$d_- + d_+ = \frac{2J_l(\eta)/\pi l}{J_l(\xi)[J_l(\xi)N_l(\eta) - J_l(\eta)N_l(\xi)]}, \quad (34)$$

where $\xi = \eta R_0/R_a$.

Similarly, for the transverse electric (TE) mode, the sum of the magnetic wave admittances is expressed as (see the Appendix)

$$b_- + b_+ = \frac{2lG_l(\omega, k)/\pi \xi^2 J_l'(\xi)}{J_l'(\xi) + G_l(\omega, k)N_l'(\xi)}, \quad (35)$$

where

$$G_l(\omega, k) = -J_l'(\eta)D(\omega, k)/N_l'(\eta)F(\omega, k), \quad (36)$$

$$D(\omega, k) = \sum_{m=-\infty}^{\infty} \frac{J_l(\eta)}{J_l'(\eta)} \left(\frac{\sin j\alpha}{j\alpha} \right)^2 \\ - \frac{\pi}{N\alpha} \frac{J_0(\eta)N_l(\xi) - J_l(\xi)N_0(\eta)}{J_l(\xi)N_l(\eta) - J_l(\eta)N_l(\xi)} \quad (37)$$

is the vacuum dispersion function,

$$F(\omega, k) = D(\omega, k) - \left(\frac{J_l(\eta)}{J_l'(\eta)} - \frac{N_l(\eta)}{N_l'(\eta)} \right) \left(\frac{\sin l\alpha}{l\alpha} \right)^2, \quad (38)$$

the integer j in Eq. (37) is defined by

$$j = s + mN, \quad (39)$$

N is the number of resonators, α is the half-angle of the open spaces as shown in Fig. 1, s is an integer satisfying $0 \leq s \leq N-1$, the prime(') denotes $(d/dx)J_l(x)$, and, finally, the parameter ξ is defined by

$$\xi^2 = \eta^2 R_c^2 / R_a^2 = (\omega^2/c^2 - k^2)R_c^2. \quad (40)$$

For detailed information in deriving Eq. (35), we urge the reader to read the Appendix. Substituting Eqs. (34) and (35) into Eq. (28) completes the dispersion relation of the cusptron microwave tube.

III. VACUUM DISPERSION RELATION

In the absence of the beam [$\nu \rightarrow 0$ in Eq. (29)], the dispersion relation in Eq. (27) reduces to the TM dispersion relation

$$J_l(\eta) = 0, \quad (41)$$

and to the TE dispersion relation

$$G_l(\omega, k) = 0, \quad (42)$$

where use has been made of Eqs. (28), (34), and (35). The TM dispersion relation is equivalently expressed as

$$\omega^2/c^2 - k^2 = \beta_{ln}^2/R_a^2, \quad (43)$$

where β_{ln} is the n th root of $J_l(\beta_{ln}) = 0$. Similarly, it is shown from Eq. (36) that the TE dispersion relation can be equivalently expressed as the ordinary TE mode,

$$\omega^2/c^2 - k^2 = \alpha_{ln}^2/R_a^2, \quad (44)$$

and the magnetron TE mode,

$$D(\omega, k) = \sum_{m=-\infty}^{\infty} \frac{J_l(\eta)}{J'_l(\eta)} \left(\frac{\sin j\alpha}{j\alpha} \right)^2 - \frac{\pi}{N\alpha} \frac{J_0(\eta)N_1(\zeta) - J_1(\zeta)N_0(\eta)}{J_1(\zeta)N_1(\eta) - J_1(\eta)N_1(\zeta)} = 0, \quad (45)$$

where α_{ln} is the n th root of $J'_l(\alpha_{ln}) = 0$. In Eq. (45), N is the number of resonators, α is the half-angle of the open space in the resonator, the integer j in Eq. (45) is defined by $j = s + mN$, $s = 0, 1, 2, \dots, N-1$, and the parameters η and ζ are defined by $\eta^2 = \zeta^2 R_a^2/R_c^2 = p^2 R_a^2 = (\omega^2/c^2 - k^2)R_a^2$ in Eq. (33).

In the remainder of this section, we investigate properties of the magnetron TE mode in Eq. (45) which relate the parameter η to the parameter ζ . In other words, the value of the parameter η is evaluated in terms of $R_c/R_a = \zeta/\eta$. Once we determine the value of the parameter η , the dispersion curve in (ω, k) parameter space is obtained from the relation

$$\omega^2/c^2 - k^2 = \eta^2/R_a^2. \quad (46)$$

Shown in Fig. 2 are plots of the parameters η (solid curves) and ζ (dashed curves) versus the radius ratio R_c/R_a for

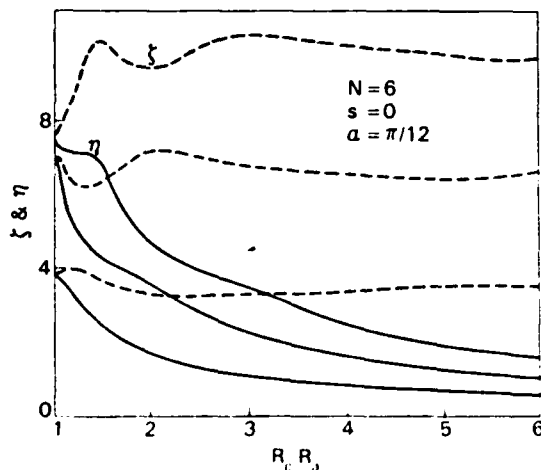


FIG. 2. Plots of the parameters η (solid curves) and ζ (dashed curves) versus the ratio R_c/R_a [obtained from Eq. (45)] for $N = 6$, $s = 0$, $\alpha = \pi/12$, and the three lowest radial modes.

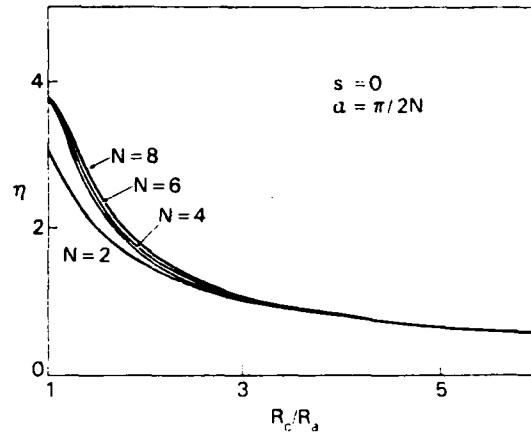


FIG. 3. Plots of the parameter η versus the ratio R_c/R_a obtained from Eq. (45) for $s = 0$, $\alpha = \pi/2N$, the lowest radial mode number, and several values of N .

$N = 6$, $s = 0$, $\alpha = \pi/12$, and the three lowest radial modes. Several points are noteworthy in Fig. 2. First, as expected, the value of the parameter η decreases monotonically as the ratio R_c/R_a increases. However, the value of the parameter ζ stays relatively steady. Second, we note that the values of parameters η and ζ at $R_c/R_a = 1$ are given by $\eta = \zeta = \alpha_{01} = 3.83$ for the lowest radial mode (the fundamental 2π mode), $\alpha_{02} = 7.02$ for the second and $\alpha_{01} = 7.50$ for the third mode. Finally, it is shown for the third radial mode that the value of the parameter η has a plateau for $1.2 < R_c/R_a < 1.4$.

In Fig. 3 we show plots of the parameter η versus ratio R_c/R_a for $s = 0$, $\alpha = \pi/2N$, the lowest radial mode number, and several values of N . Remarkably, the value of the parameter η is relatively independent of the number N for $N > 3$ and for the lowest radial mode number. On the other hand, for $N = 2$ and $R_c/R_a = 1$, the parameter η is given by $\eta = \zeta = \alpha_{21} = 3.05$. Dependence of the parameter η on the integer s is presented in Fig. 4 where the parameter η is plotted versus the ratio R_c/R_a for $N = 6$, $\alpha = \pi/12$, the lowest radial mode number, and different values of s . After a careful examination of Eq. (45), we note that the dispersion relation for $s = 1$ is identical to that for $s = N - 1$, and so on. In this regard, plots in Fig. 4 are presented only for the integer s satisfying $0 \leq s \leq N/2$. Obviously from Fig. 4, we conclude that the parameter η depends sensitively on the integer s . For $R_c/R_a = 1$, the value of the parameter η is given by $\eta = \alpha_{sl}$ for each s . Of course, the vacuum dispersion relation in Eq. (45) is also investigated for different values of the half-angle α . Shown in Fig. 5 are plots of the parameter η versus the ratio R_c/R_a for $N = 8$, $s = 0$, lowest radial mode number, and several values of α . The parameter η reduces with increasing value of the half-angle α for the range $1 < R_c/R_a < 1.4$, which is a typical parameter range of present experiments.

IV. NEGATIVE-MASS INSTABILITY IN MAGNETRON-TYPE CONDUCTOR

In this section, we investigate stability properties of the negative-mass instability in an E layer propagating through

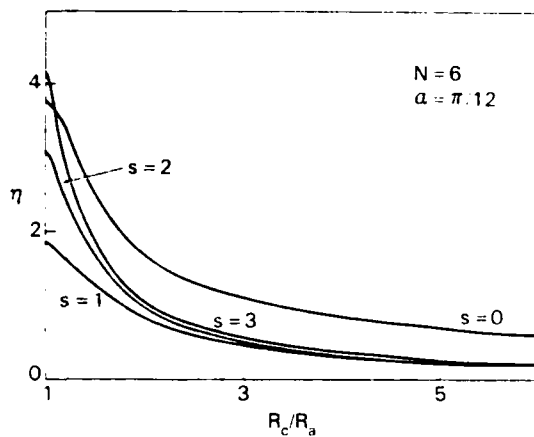


FIG. 4. Plots of the parameter η versus the ratio R_c/R_a obtained from Eq. (45) for $N=6$, $\alpha=\pi/12$, the lowest radial mode number, and different values of s .

a magnetron-type conductor, by making use of the dispersion relation in Eq. (29). The growth rate and bandwidth of the negative-mass instability are directly related to the gain and bandwidth of the cusptron amplifier or oscillator. Making use of the fact that the "Doppler-shifted" eigenfrequency Ω in Eq. (7) is well removed from the electron cyclotron resonance (i.e., $|\Omega| \ll \omega_c$), and evaluating the function $\Gamma(\omega, k)$ at $k = k_b = (\omega - l\omega_c)/\beta_z c$ for the amplifier and at $\omega = \omega_b = l\omega_c + k\beta_z c$ for the oscillator, the dispersion relation in Eq. (29) can be approximated by

$$\left[\Gamma(\omega, k_b) - \frac{1}{\beta_z c} \left(\frac{\partial}{\partial k} \Gamma \right)_{k_b} \Omega \right] \left(\Omega + i \frac{|k_b| \beta_z c \hat{\gamma} \Delta}{\gamma_z^3} \right)^2 = - \frac{\nu c^2}{2\gamma R_0^2} (l^2 \mu - k_b^2 R_0^2), \quad (47)$$

for the amplifier, and

$$\left[\Gamma(\omega_b, k) + \left(\frac{\partial}{\partial \omega} \Gamma \right)_{\omega_b} \Omega \right] \left(\Omega + i \frac{|k| \beta_z c \hat{\gamma} \Delta}{\gamma_z^3} \right)^2 = - \frac{\nu c^2}{2\gamma R_0^2} (l^2 \mu - k^2 R_0^2), \quad (48)$$

for the oscillator. In the remainder of this section, the growth

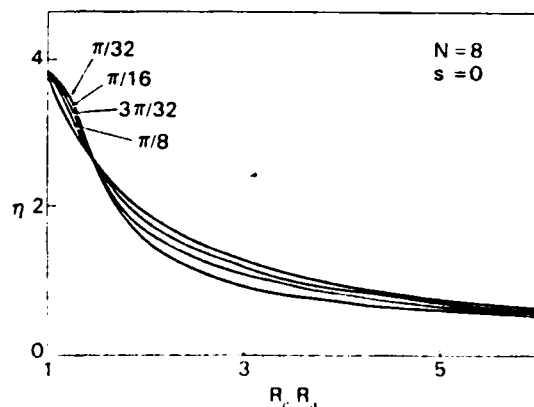


FIG. 5. Plots of the parameter η versus the ratio R_c/R_a obtained from Eq. (45) for $N=8$, $s=0$, the lowest radial mode number, and several values of α .

rate $\Omega_i = \text{Im } \Omega$ and the Doppler-shifted real oscillation frequency $\Omega_r = \text{Re } \Omega$ are numerically calculated from Eq. (47) for the amplifier and from Eq. (48) for the oscillator. Numerical calculation is carried out for the nonrelativistic electron beam parameters $\nu=0.002$, $\Delta=0.04$, $\beta_a=0.4$, and $\beta_z=0.2$ corresponding to $\hat{\gamma}=1.118$. For a relativistic beam, $\beta_a=0.96$ and $\beta_z=0.2$ correspond to $\hat{\gamma}=5.1$.

To the lowest order, the eigenfrequency ω and axial wavenumber k are obtained from the simultaneous solution of the vacuum waveguide mode dispersion relation,

$$\omega^2/c^2 - k^2 = \eta^2/R_a^2, \quad (49)$$

and the condition for cyclotron resonance

$$\omega \simeq l\omega_c + k\beta_z c. \quad (50)$$

Moreover, to maximize the growth rate and efficiency of microwave generation and amplification, it is required that the group velocity of the vacuum waveguide mode in Eq. (49) be approximately equal to the beam velocity, i.e.,

$$V_g = \frac{d\omega}{dk} = \frac{kc^2}{\omega} \simeq \beta_z c. \quad (51)$$

Solving Eqs. (50) and (51) for the characteristic frequency and axial wavenumber $(\omega, k) = (\omega_0, k_0)$, we find (Fig. 6)

$$\omega_0 = l\omega_c \gamma_z^2, \quad k_0 = l\omega_c \beta_z \gamma_z^2/c. \quad (52)$$

For maximum growth, it is also required that (ω_0, k_0) solve Eq. (49) in leading order. Therefore, for maximum efficiency, we find that R_a should satisfy

$$R_a = \eta c / l\omega_c \gamma_z. \quad (53)$$

Under the grazing condition in Eq. (53), the cyclotron resonance mode in Eq. (50) is a tangential line of the vacuum waveguide mode in Eq. (49), as shown in Fig. 6. Noting $\beta_0 = R_0 \omega_c / c$, it is found from Eq. (53) that the beam radius is determined from

$$R_0/R_a = \beta_0 c / R_a \omega_c = l\beta_0 \gamma_z / \eta, \quad (54)$$

and that the parameter η should satisfy the inequality

$$\eta / l\gamma_z > \beta_0, \quad (55)$$

for a physically acceptable cusptron microwave tube.

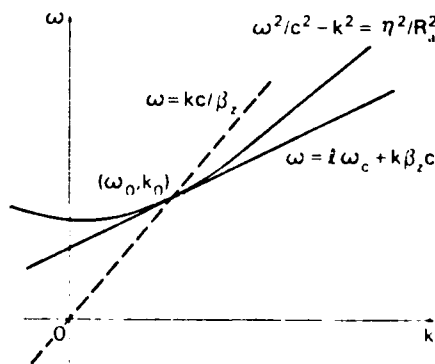


FIG. 6. The straight lines $\omega = k\beta_z c + l\omega_c$ and $\omega = kc/\beta_z$ intersect at (ω_0, k_0) ($l\omega_c \gamma_z^2/c, \beta_z \gamma_z^2/c$). The vacuum waveguide mode $\omega = (k^2 c^2 + \eta^2 c^2 / R_a^2)^{1/2}$ passes through (ω_0, k_0) provided $R_a \omega_c / c = \eta / l\gamma_z$.

A. Nonrelativistic cusptron amplifier

In this section, we summarize results of numerical calculation from Eq. (47) for the amplifier in a nonrelativistic electron beam ($\beta_u = 0.4$) propagating through a uniform applied magnetic field with the field index $n = 0$. Shown in Fig. 7 is a plot of the geometric factor $\Gamma(\omega, k_z)$ versus the normalized frequency ω/ω_c in Eq. (28) for $N = 6$, $l = 6$, $s = 0$, $\alpha = \pi/12$, $R_c/R_a = 1.4$, and $R_a\omega_c/c = 0.4433$ corresponding to the grazing condition in Eq. (53) for the parameter $\eta = 2.715$ in Fig. 2. Here the axial wavenumber k is substituted for by $k_z = (\omega - \omega_c)/\beta_z c$ consistent with the dispersion relation in Eq. (47) for amplifiers. As expected from the condition $R_a\omega_c/c = 0.4433$, the curve of the geometric factor Γ grazes the horizontal line. Values of the geometric factor Γ are very close to zero in a considerable range (i.e., $6 < \omega/\omega_c < 6.5$ in Fig. 7) of ω -space, thereby exhibiting the possibility of a broad unstable frequency range.

Figure 8 shows plots of (a) normalized growth rate Ω_r/ω_c and (b) Doppler-shifted real frequency Ω_r/ω_c vs ω/ω_c obtained from Eq. (47) for the electron beam parameters $\nu = 0.002$, $\Delta = 0.04$, $\beta_u = 0.4$, $\beta_z = 0.2$, the field index $n = 0$, and the grazing conditions (i.e., $R_a\omega_c/c = 0.4433$ for $R_c/R_a = 1.4$, 0.493 for $R_c/R_a = 1.3$, 0.5453 for $R_c/R_a = 1.2$, 0.5905 for $R_c/R_a = 1.1$, and 0.6257 for $R_c/R_a = 1$) corresponding to the fundamental 2π mode, and parameters otherwise identical to Fig. 7. For each value of R_c/R_a , the growth rate curve consists of two parts; a solid line corresponding to a relatively large Doppler-shifted real frequency and a dashed line corresponding to a very small Doppler-shifted real frequency [Figs. 8(a) and (b)]. The efficiency of a microwave tube is directly proportional to the Doppler-shifted real frequency.¹⁸ In this regard, even though instability of the dashed curve exhibits a large growth rate, there is no significant amplification in this frequency range corresponding to a small Doppler-shifted real frequency. Obviously from Fig. 8(a), the amplification growth rate [solid curve in Fig. 8(a)] reduces as R_c/R_a approaches to unity. In particular, for $R_c/R_a = 1$, the amplification growth rate vanishes, thereby smoothly connecting two dashed curves in Fig. 8(a). In this case ($R_c/R_a = 1$), the Doppler-shifted real

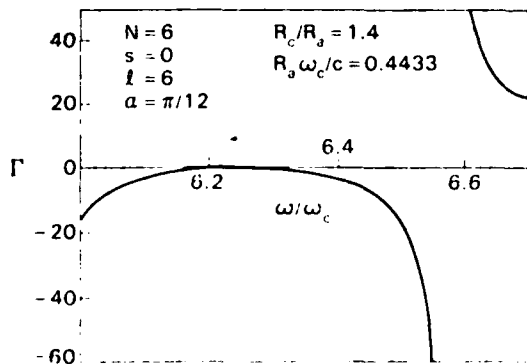


FIG. 7. Plot of the geometric factor $\Gamma(\omega, k_z)$ versus the normalized frequency ω/ω_c in Eq. (28) for $N = 6$, $l = 6$, $s = 0$, $\alpha = \pi/12$, $R_c/R_a = 1.4$, and $R_a\omega_c/c = 0.4433$ corresponding to the grazing condition for $\beta_z = 0.2$.

frequency Ω_r/ω_c is less than 0.003. We also note from Fig. 8(a) that the maximum growth rate of the cusptron normalized by the excitation frequency is comparable to that for the conventional gyrotron amplifier [curve for $R_c/R_a = 1.4$ Fig. 8(a)]. Also the Doppler-shifted real frequency for $R_c/R_a = 1.4$ in Fig. 8(b) exhibits a strong possibility of very high efficiency in microwave amplification.

Numerical investigation of Eq. (47) has been also carried out for a broad range of physical parameters s , l , α , and N and various radial mode numbers. From this numerical calculation, we make several conclusions. First, under the grazing condition $R_c = \eta c/N\omega$ corresponding to $l = N$, there is no amplification growth rate of instability for perturbations with $l \neq N$ azimuthal harmonic number. Second, optimizing the value of the parameter $R_a\omega_c/c$ according to Eq. (53), the $l \neq N$ perturbations also have a substantial amount of the amplification growth rate with relatively large Doppler-shifted real frequency. However, comparing with Fig. 8, we conclude that the amplification growth rate of the $l = N$ perturbation is the largest and the most effective means of microwave amplification. Third, after optimizing the parameter $R_a\omega_c/c$ according to Eq. (53), the $s = 0$ perturbation is the best for microwave amplification. Fourth, it is found that the lowest radial mode perturbation is the

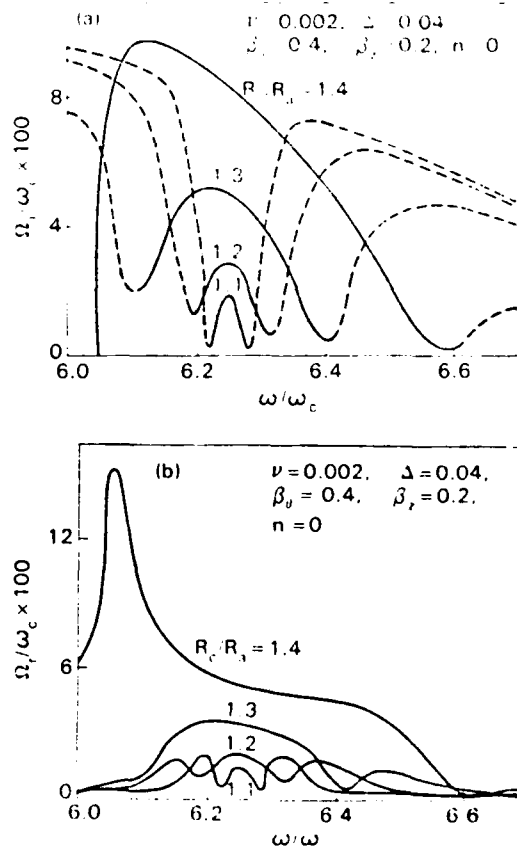


FIG. 8. Plots of (a) the normalized growth rate Ω_r/ω_c and (b) the Doppler-shifted real oscillation frequency Ω_r/ω_c vs ω/ω_c obtained from Eq. (47) for electron beam parameters $\nu = 0.002$, $\Delta = 0.04$, $\beta_u = 0.4$, and $\beta_z = 0.2$, field index $n = 0$, the grazing conditions corresponding to Eq. (53), and parameters otherwise identical to Fig. 7.

dominant unstable mode. Fifth, we also found from the numerical calculation that after optimizing $R_a \omega_c / c$, the growth rate and Doppler-shifted real frequency are almost independent of α in the range $\pi/4N < \alpha < \pi/2N$ for $s = 0$, $l = N$, and the lowest radial mode number. However, increasing α from $\pi/2N$ to π/N reduces drastically the growth rate and Doppler-shifted real frequency. Finally, stability properties have been investigated also for $N = 4$ and parameters otherwise identical to Fig. 8. It has been shown from numerical calculation that the maximum growth rate and Doppler-shifted real frequency of $N = 4$ are comparable to those of $N = 6$ case. However, the optimum value of the growth rate and real frequency occurs at $R_c/R_a = 1.8$ and $R_a \omega_c / c = 0.4494$. After consideration of all of these properties, we conclude for the nonrelativistic electron beam with $\beta_a = 0.4$ that the optimum physical parameters for microwave amplification are $N = 6$, $l = 6$, $s = 0$, $\alpha = \pi/12$, $R_c/R_a = 1.4$, and $R_a \omega_c / c = 0.4433$.

B. Effect of nonzero field index

As shown in Eqs. (47) and (48), the coupling coefficient is directly proportional to the parameter

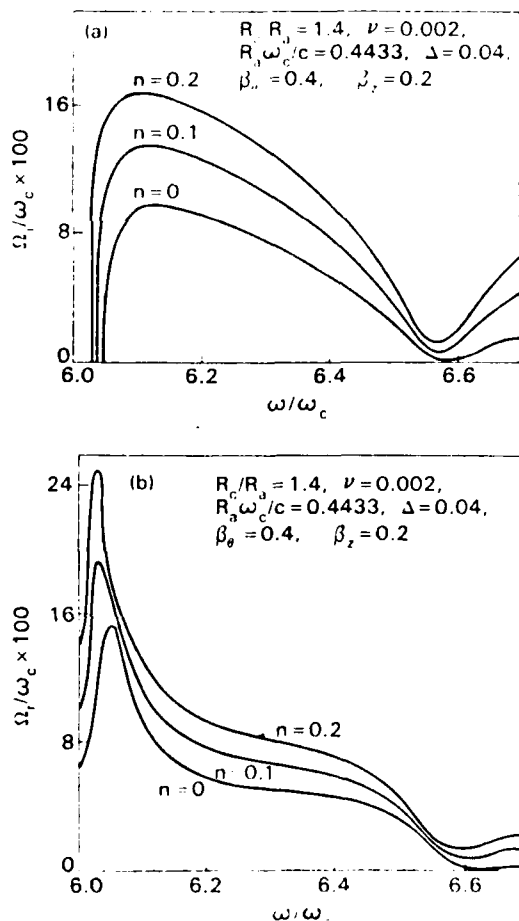


FIG. 9. Plots of (a) the normalized growth rate Ω_r/ω_c and (b) the Doppler-shifted real oscillation frequency Ω_r/ω_c vs ω/ω_c obtained from Eq. (47) for $R_c/R_a = 1.4$, $R_a \omega_c / c = 0.4433$, several different values of the field index n , and parameters otherwise identical to Fig. 8.

$$\mu = \frac{1}{1-n} - \frac{1}{\gamma_a^2} = \beta_a^2 + \frac{n}{1-n}, \quad (56)$$

where n is the field index defined in Eq. (16). Evidently from Eq. (56), for a nonrelativistic beam with $\beta_a^2 \ll 1$, a small increase of the field index from zero makes a big difference in the coupling coefficient, thereby enhancing the gain and efficiency of the microwave amplification. Shown in Fig. 9 are plots of (a) the normalized growth rate Ω_r/ω_c and (b) the Doppler-shifted real oscillation frequency Ω_r/ω_c obtained from Eq. (47) for $R_c/R_a = 1.4$, $R_a \omega_c / c = 0.4433$, several different values of the field index n , and parameters otherwise identical to Fig. 8. Obviously, the growth rate and real frequency increase substantially by increasing the field index from zero to a small positive value. However, since the applied magnetic field is no longer uniform along the axial direction for a nonzero field index, tapering of the conducting wall radius R_a is required in order to match the grazing condition in Eq. (53) (e.g., $R_a \omega_c / c = 0.4433$ in Fig. 9).

C. Nonrelativistic cusptron oscillator

The growth rate and Doppler-shifted real oscillation frequency are numerically obtained from Eq. (48) for the oscillations in a nonrelativistic electron beam. In Fig. 10 we show plots of (a) the normalized growth rate and (b) the Doppler-shifted real frequency versus the normalized axial wavenumber kc/ω_c obtained from Eq. (48) for the parameters identical to Fig. 8. The normalized lowest-order eigenfrequency $\omega_r/\omega_c = l + k\beta_z c/\omega_c$ is also shown in the horizontal scale in Fig. 10. Comparing Fig. 10(a) with Fig. 8(a), we note that the unstable range in frequency space for the oscillation is broader than that for the amplifier. Perturbations in the amplifier are unstable only for the positive k space. Moreover, the real frequency in the oscillator is considerably different from that in the amplifier [Figs. 8(b) and 10(b)].

D. Relativistic cusptron amplifier

Preliminary investigation of Eq. (47) has been carried out for the amplifiers in a relativistic electron beam with $\beta_a = 0.96$ and $\beta_z = 0.2$. After a careful examination of Eq. (55) and Fig. 2, we note for the relativistic electron beam ($\beta_a \rightarrow 1$) that the first available coupling occurs at the third-lowest radial mode number where the parameter η is larger than N for a reasonable range of R_c/R_a . Figure 11 shows plots of (a) the normalized growth rate Ω_r/ω_c and (b) the Doppler-shifted real frequency Ω_r/ω_c vs ω/ω_c for $\beta_a = 0.96$, the grazing conditions ($R_a \omega_c / c = 1.1101$ for $R_c/R_a = 1.5$, 1.1679 for $R_c/R_a = 1.25$, and 1.2249 for $R_c/R_a = 1$), and parameters otherwise identical to Fig. 8. Contrary to nonrelativistic cusptron amplifiers (in Fig. 8), the growth rate and bandwidth of instability in Fig. 11 increase drastically as R_c/R_a approaches unity. However, for $R_c/R_a = 1.5$ and $R_a \omega_c / c = 1.1101$, the Doppler-shifted real frequency of perturbations with the $l \neq N$ azimuthal mode number vanishes, while the $l = N$ perturbation has considerably large Doppler-shifted real frequency. In this regard, by selecting $R_c/R_a = 1.5$ and $R_a \omega_c / c = 1.1101$, microwaves with $l = N$ mode perturbations are dominantly amplified, thereby optimizing the

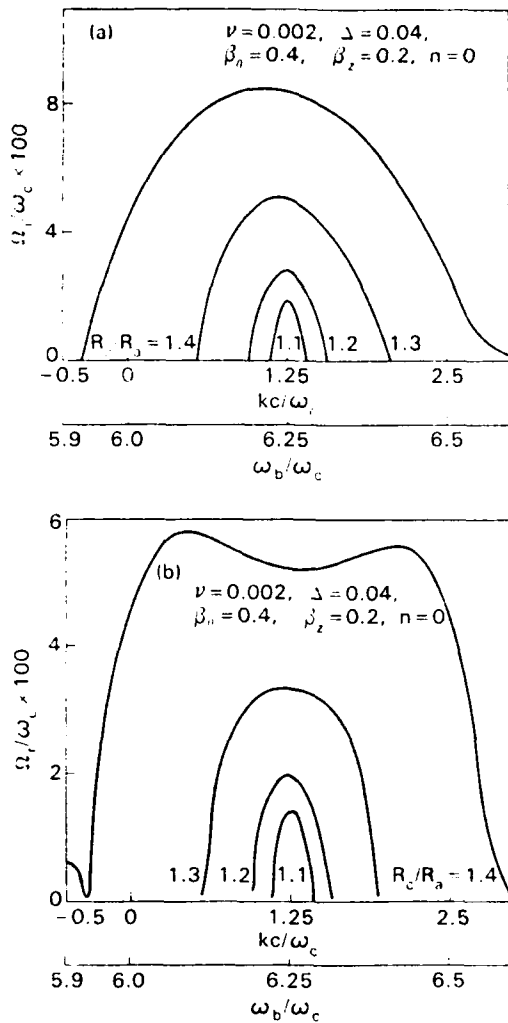


FIG. 10. Plots of (a) the normalized growth rate Ω_i/ω_c and (b) the Doppler-shifted real frequency Ω_r/ω_c versus the normalized axial wavenumber kc/ω_c obtained from Eq. (48) for parameters identical to Fig. 8.

microwave power output for radiation with frequency $\omega \simeq \omega_c$. On the other hand, for $R_c/R_a = 1$, various other modes compete with the $l = N$ mode, leading to multimode amplification. Therefore, even though the growth rate for $R_c/R_a = 1.5$ is less than that for $R_c/R_a = 1$, the geometric configuration with $R_c/R_a = 1.5$ is more effective to amplify microwaves. Numerical investigation of Eq. (47) for $N = 12$ and $N = 24$ also exhibits very similar properties.

After a careful examination of the geometric factor $\Gamma(\omega, k)$ for a broad range of various physical parameters, it can be found that

$$\Gamma(\omega, k_h) \simeq 0, \quad \left(\frac{\partial \Gamma(\omega, k)}{\partial k} \right)_{k=k_h} \simeq 0, \quad (57)$$

for particular values of $R_c/\omega_c/c$ and frequency ω . In this case, in order to correctly evaluate the gain of the cusptron, we approximate Eq. (29) by

$$\left[\Gamma(\omega, k_h) - \frac{1}{\beta_z c} \left(\frac{\partial}{\partial k} \Gamma \right)_{k=k_h} \Omega + \frac{1}{2\beta_z^2 c^2} \left(\frac{\partial^2}{\partial k^2} \Gamma \right)_{k=k_h} \Omega^2 \right] \times \left(\Omega + i \frac{|k_h \beta_z c \hat{\gamma} \Delta|^2}{\hat{\gamma}_z^2} \right)^2 = - \frac{\nu c^2}{2\hat{\gamma} R_0^2} (l^2 \mu - k_h^2 R_0^2). \quad (58)$$

Of course, the dispersion relation in Eq. (47) is used to obtain the gain for a broad range of physical parameters except ω satisfying Eq. (57). Obviously, Eq. (47) fails to estimate the gain for this frequency range. We therefore make use of Eq. (58) to obtain the gain at the frequency satisfying Eq. (57). We also emphasize the reader that the gain of the cusptron amplifier at the frequency ω corresponding to Eq. (57) is significantly greater than that at other frequencies.

In order to illustrate a high-gain cusptron amplification, shown in Fig. 12 are plots of the normalized growth rate Ω_i/ω_c vs ω/ω_c obtained from Eqs. (47) and (58) for $\beta_n = 0.96$, $N = 24$, $l = 25$, $R_c/R_a = 1.1$, $R_a \omega_c/c = 1.069$, and parameters otherwise identical to Fig. 8. The dashed curves in Fig. 12 are plots of the gain obtained from Eq. (47) in the frequency range satisfying Eq. (57). Obviously, Eq. (47) fails in this frequency range. However, Eq. (58) correctly evaluates the growth rate in this region. As expected, the maximum gain in Fig. 12 is considerably enhanced in comparison with that of an ordinary cusptron amplifier (Figs. 8 and 11).

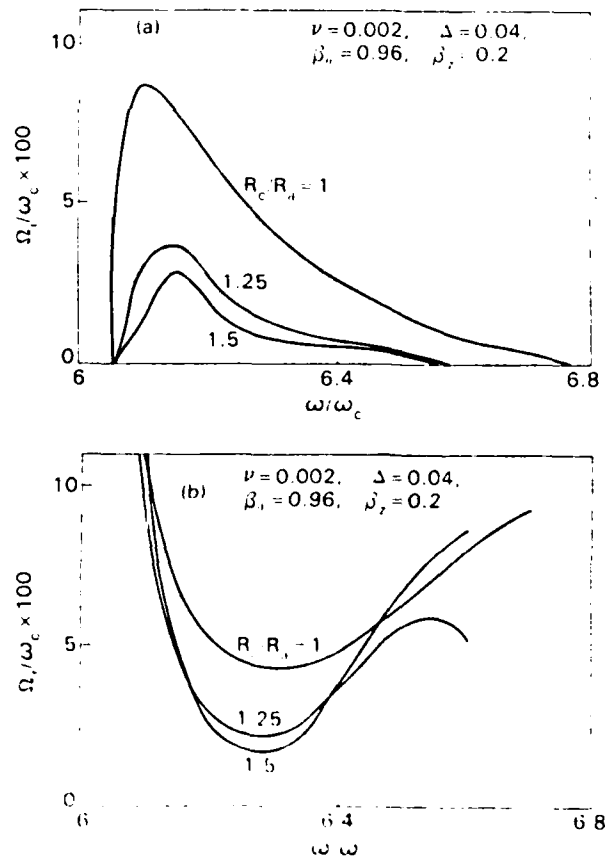


FIG. 11. Plots of (a) the normalized growth rate Ω_i/ω_c and (b) the Doppler-shifted real frequency Ω_r/ω_c vs kc/ω_c for $\beta_n = 0.96$, the grazing conditions corresponding to Eq. (53), and parameters otherwise identical to Fig. 8.

Millimeter wave emission from a rotating electron ring in a rippled magnetic field

G. Bekefi and R. E. Shefer

Department of Physics and Research Laboratory of Electronics, Massachusetts Institute of Technology, Cambridge, Massachusetts 02139

W. W. Destler

Department of Electrical Engineering, University of Maryland, College Park, Maryland 20742

(Received 30 September 1983; accepted for publication 4 November 1983)

We report measurements of millimeter wave emission from a rotating relativistic electron ring (2 MV, 1 kA) in which electrons move in quasi-circular orbits under the combined action of a uniform axial magnetic field and an azimuthally periodic wiggler magnetic field. We observe radiation at frequencies above 91 GHz, at power levels in excess of 200 kW.

PACS numbers: 41.70. + t, 42.55.Bi, 42.52. + x

There have been many theoretical¹ and experimental² studies of free-electron lasers (FEL's) in linear geometry with spatially periodic transverse^{1,2} or longitudinal³⁻⁶ magnetic wiggler fields. Such configurations have gain limitations imposed by the finite length of the interaction region. Recently, a novel circular version of the free-electron laser has been explored both theoretically⁷⁻⁹ and experimentally¹⁰ in which a rotating, relativistic electron stream is subjected to an azimuthally periodic wiggler field. The potential advantages of circular FEL's as compared with the conventional linear form are several. First, the beam circulates continuously through the wiggler field resulting in a long effective interaction region. Secondly, because of the recirculation of the growing electromagnetic wave, the device provides its own internal feedback and is in essence an oscillator rather than an amplifier, as is the case in linear FEL's. And thirdly, because the electron motion is primarily circular the system¹⁰ is very compact.

There are several ways of producing a rotating relativistic electron stream. One is to subject the electrons to orthogonal electric and magnetic fields as is typical in magnetron-like devices. Here, the electrons undergo a $\mathbf{v}(r) = \mathbf{E}_\theta(r) \times \mathbf{B}_z / |\mathbf{B}_z|^2$ drift in a radial electric field $\hat{r}E_\theta(r)$ and a uniform axial magnetic field $\hat{z}B_z$. Addition of an azimuthally periodic magnetic field $\mathbf{B}_w(\theta, r)$ then results in a circular FEL. This

scheme has been explored previously,^{7,8,10} and though the experimental results¹⁰ are encouraging, it may have a potential drawback in that the electron velocity $v(r)$ varies with radial distance r . This velocity shear may lead to degradation of the spectral purity of the emitted electromagnetic radiation, and a reduction in gain and efficiency of the device.

In this letter we describe initial experiments on a circular FEL which uses a monoenergetic rotating electron ring and thereby circumvents the problem of velocity shear mentioned above. Moreover, in the device discussed below one has better control over the circulating current than in a magnetronlike scheme where the anode-cathode gap is part¹⁰ of the magnetic wiggler interaction region.

A high quality (energy spread $\leq 1\%$) rotating electron ring is produced by injecting a hollow nonrotating beam into a narrow magnetic cusp.^{11,12} The hollow beam is generated by field emission from an annular graphite cathode energized by a pulsed, high voltage, high current accelerator (2 MV, 20 kA, 30 ns). The resulting rotating electron ring is guided downstream from the cusp by a uniform axial magnetic field of ~ 1.4 kG. The ring is 6 cm in radius, has a duration of ~ 5 ns, and carries an axial current of ~ 1.5 kA. The electron rotation velocity $v_\theta \simeq 0.96c$, and the electron axial velocity $v_z \simeq 0.2c$. Thus, in the absence of the wiggler magnetic field, the electron orbits form fairly tight helices.

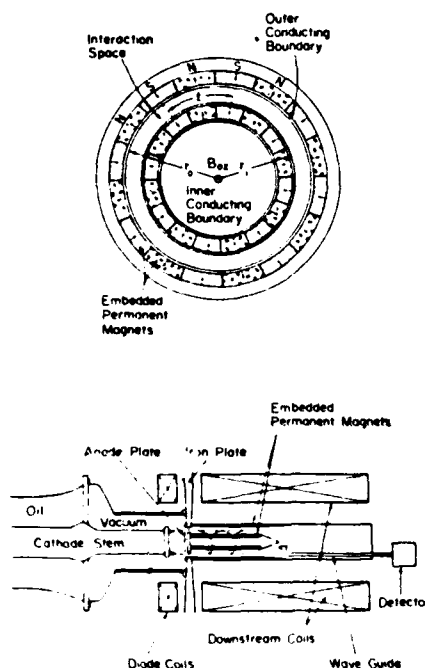


FIG. 1. General experimental configuration.

A schematic of the device is illustrated in Fig. 1. It comprises two smooth coaxial stainless steel cylinders of radii $r_0 = 6.58$ cm and $r_i = 5.25$ cm, respectively. The electron ring propagates within the gap formed by the two cylinders. Superimposed on the axial guiding magnetic field is an azimuthally periodic magnetic wiggler field B_w , which, near the center of the gap, is primarily¹⁰ radial and is thus transverse to the electron flow velocity, as is the case in conventional linear free-electron lasers. A single particle computer simulation program has been generated for the purpose of studying the electron motion in the combined axial and wiggler magnetic fields. We see from Fig. 2 that the trajectory is not perturbed too strongly: it remains quasi-helical, the radial displacements are small, and the electron does not strike the cylinder walls.

In our device, the wiggler magnetic field is produced by an assembly of 384 samarium-cobalt bar magnets,^{10,13}

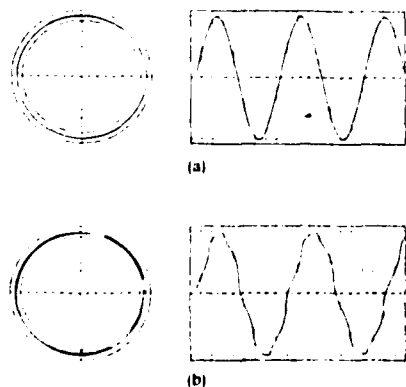


FIG. 2. Calculated particle orbits in the r - θ and r - z planes for an electron injected with $v_r = 0.20c$, $v_z = 0.96c$ into the interaction space with (a) $B_{\theta} = 1.4$ kG, $B_w = 0$, and (b) $B_{\theta} = 1.4$ kG, $B_w = 1.3$ kG.

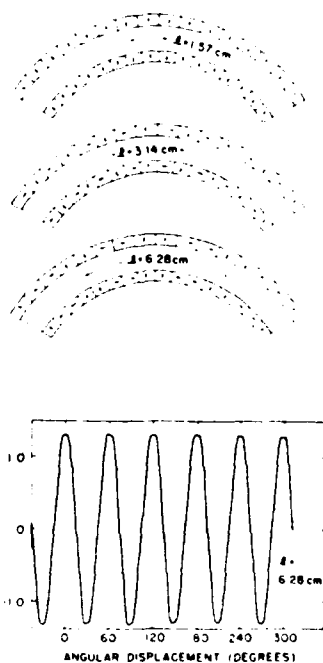


FIG. 3. Arrangement of bar magnets (top); Hall probe measurement of the wiggler field at a radial position $r = 5.92$ cm, as a function of azimuthal angle (bottom).

$0.40 \times 0.40 \times 4.8$ cm, each having a residual induction of ~ 9.0 kG. The magnets are positioned behind the grounded stainless steel cylinders and held in place in grooved aluminum holders. To achieve a given periodicity l , the dipole axes of the magnets are arranged as illustrated in Fig. 3. The lower part of the figure shows a Hall-probe measurement of the radial component of the wiggler field at the center of the vacuum gap. The measured field amplitude equals 1.31 kG. The axial length of the wiggler is 20 cm. This is achieved by stacking end-to-end four rows of bar magnets. At the present time, all of the radiation measurements described below were made with a wiggler having six spatial periods (N) and a periodicity $l = 6.28$ cm. Shorter periodicities are expected to give radiation at frequencies which lie above the range of our detection equipment.

To estimate the radiation frequency we assume that in the presence of the wiggler, the electrons experience a ponderomotive force which causes electron bunching in the θ direction. When the θ -directed phase velocity $\omega/(k_w + k_{\theta})$ of this space-charge wave is slightly below the electron velocity v_0 , energy can be given up to the electromagnetic wave. Here $k_w = N/r = 2\pi/l$, ω is the radiation frequency; $k_{\theta} = m/r$ is the radiation wave number with m as the mode number of a transverse magnetic (TM) mode of the coaxial waveguide and $r \approx (r_0 + r_i)/2$. Near cutoff ($k_z \rightarrow 0$), one obtains the familiar FEL formula,^{1,2}

$$\omega \approx (1 + \beta_0 \gamma^2 k_w c / K). \quad (1)$$

Here $\beta_0 = v_0/c$, $\gamma = 1 + eV/m_0 c^2$ with V as the beam voltage; $\Omega_w = eB_{0w}/m_0$ is the nonrelativistic cyclotron frequency in the wiggler field of amplitude B_{0w} , and $K = 1 + (\Omega_w/k_w c)^2$.

The radiation generated in the interaction region is al-

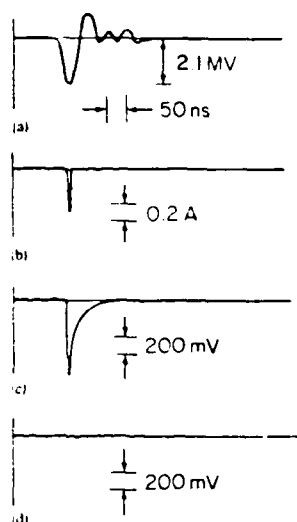


FIG. 4. Oscilloscope waveforms of (a) diode voltage, (b) axial current collected by a 2.24-mm² collector located in the center of the interaction region, (c) microwave signal in *T*-band (91–170 GHz) with wiggler magnets, and (d) microwave signal in *T*-band without wiggler magnets.

lowed to leak out from the gap formed by the two coaxial cylinders. It is received by means of a small horn antenna, and is guided through various waveguide cut-off filters to a crystal detector where it is rectified and displayed on a fast oscilloscope. Figure 4(c) illustrates the time history of a typical radiation burst at frequencies above 91 GHz as measured with a *T*-band (91–170 GHz) filter. When the magnetic wiggler field is turned off (by removing the samarium-cobalt magnets from their grooved aluminum cylinders) the emitted power falls to a level too small to be distinguished from background noise [Fig. 4(d)]. We thus conclude that the observed radiation is produced only in the presence of the wiggler field.

We have as yet not addressed the problem of how best to couple out the available radiation. Our horn antenna merely probes the radiation field and receives only a small fraction of the available power. Using the crystal calibration of our detector, the total power radiated from the device at frequencies above 91 GHz is estimated to be no smaller than 200 kW. Inserting experimental parameters into Eq. (1) yields a radiation frequency $\omega/2\pi \approx 170$ GHz. But, we have not yet measured the spectrum.

In addition to the *T*-band (91–170 GHz) range of frequencies, we also explored emission at lower frequencies, from 21 GHz and up. Here we find that some emission occurs even in the absence of the wiggler magnetic field. The cause of this radiation is the negative mass instability.^{14–17} However, as a result of the proximity¹⁸ of the two grounded, concentric metal cylinders the level of this radiation is greatly reduced compared to that observed in earlier work^{14,15} on the negative mass instability, where the conducting boundaries were not in such close proximity to the beam. When the wiggler magnetic field is introduced the level of the low-

frequency emission remains either unchanged or, in some cases, is diminished. This shows that the presence of the wiggler field does not enhance the negative mass instability, which has been a worrisome possibility.

In conclusion, we have observed radiation in the millimeter wavelength range ($\lambda < 3.3$ mm) from a novel type of circular FEL which uses a high quality, high current relativistic electron ring rotating in an azimuthally periodic wiggler magnetic field. The emitted power attributed to the FEL instability is at least 200 kW. Spectral measurements using a calibrated microwave grating spectrometer^{10,19} will be carried out in the near future. In addition, by rearranging the magnets as illustrated in Fig. 3, we will be able to shorten the wiggler periodicity l and thereby study emission at wavelengths ranging from 0.05 to 1.0 mm.

This work was supported in part by the United States Air Force Office of Scientific Research, in part by the Department of the Air Force Aeronautical Systems Division, and in part by the National Science Foundation. We gratefully acknowledge the assistance of A. Bromborsky in performing the orbit calculations.

¹N. M. Kroll and W. A. McMullin, *Phys. Rev. A* **17**, 300 (1978); P. Sprangle and R. A. Smith, *Phys. Rev. A* **21**, 293 (1980) and references therein.
²P. A. Sprangle, R. A. Smith, and V. L. Granatstein, in *Infrared and Submillimeter Waves*, edited by K. Button (Academic, New York, 1979), Vol. 1, p. 279 and references therein.

³W. A. McMullin and G. Bekefi, *Appl. Phys. Lett.* **39**, 845 (1981).

⁴W. A. McMullin and G. Bekefi, *Phys. Rev. A* **25**, 1826 (1982).

⁵R. C. Davidson and W. A. McMullin, *Phys. Rev. A* **26**, 1997 (1982).

⁶R. C. Davidson and W. A. McMullin, *Phys. Fluids* **26**, 840 (1983).

⁷G. Bekefi, *Appl. Phys. Lett.* **40**, 578 (1982).

⁸R. D. Estes, A. Palevsky, and A. T. Drobot, *Bull. Am. Phys. Soc.* **27**, 1075 (1982); also R. E. Shefer, G. Bekefi, R. D. Estes, C.-L. Chang, E. Ott, T. M. Antonsen, and A. T. Drobot, *Proceedings of Fifth International Topical Conference High Power Electron and Ion-Beam Research and Technology*, San Francisco 1983.

⁹R. C. Davidson and W. A. McMullin, *Massachusetts Institute of Technology, Cambridge, Massachusetts, Plasma Fusion Center Report No. PFC/JA-83-33*, 1982.

¹⁰G. Bekefi, R. E. Shefer, and B. D. Nevins, *Massachusetts Institute of Technology, Cambridge, Massachusetts, Plasma Fusion Center Report No. PFC/JA-83-33*, 1983; also *Lasers '82*, Society for Optical and Quantum Electronics, *SOQUE*, 1982 (STS, 1982), p. 136.

¹¹M. J. Rhee and W. W. Destler, *Phys. Fluids* **17**, 1574 (1974).

¹²W. W. Destler, P. K. Misra, and M. J. Rhee, *Phys. Fluids* **18**, 1820 (1975).

¹³K. Halbach, *Lawrence Berkeley Laboratory, University of California Accelerator and Fusion Research Division Report No. LBL11393*, August 1980; also *IEEE Trans. Nucl. Sci.* **NS-26**, 3882 (1979).

¹⁴W. W. Destler, H. Romero, C. D. Striffler, R. L. Weiler, and W. Namkung, *J. Appl. Phys.* **52**, 2740 (1981).

¹⁵W. W. Destler, D. W. Hudgings, M. J. Rhee, S. Kawasaki, and V. L. Granatstein, *J. Appl. Phys.* **48**, 3291 (1977).

¹⁶H. Uhm and R. C. Davidson, *J. Appl. Phys.* **49**, 593 (1978).

¹⁷Y. Goren, H. Uhm, and R. C. Davidson, *J. Appl. Phys.* **49**, 3789 (1978).

¹⁸L. J. Laslett, *IEEE Trans. Nucl. Sci.* **NS-20**, 271 (1973).

¹⁹J. A. Pasour and S. P. Schlesinger, *Rev. Sci. Instrum.* **48**, 1355 (1977); also R. E. Shefer, Ph.D. thesis, Department of Physics, M.I.T. 1981 (unpublished).

Abstract Submitted
For the Twenty-fifth Annual Meeting
Division of Plasma Physics
November 7 to 11, 1983

Category Number and Subject 4.9 Coherent Radiation Generation

☒ Theory ☐ Experiment

Interaction of a Rotating Electron Beam with a Cylindrical Slotted Wall Structure. R. KULKARNI and C. D. STRIFFLER, University of Maryland.¹---A theoretical study of the generation of microwave radiation from a relativistic rotating electron beam propagating along a concentric slotted wall cylindrical waveguide is presented. The empty waveguide modes of the slotted structure as well as the linear stability analysis of the resonant interaction of a beam mode $\omega = \ell\omega_c + kv_z$ and a guide mode are displayed. An analysis² is made of the different modes in the slotted structure with respect to the power efficiency in each mode. The effects of slotted wall geometry are then examined in order to enhance interaction with the 2π mode of the guide. The effects of mode coupling and competition on the stability of the 2π mode is also examined relative to changes in slot geometry. Specific results for a 2 MeV beam in the presence of a 12 or 20 slotted wall structure are shown and compared with experimental data.¹

* This work is supported by AFOSR and the Electrical Engineering Computer Facility.

¹C. D. Striffler, W. W. Destler, R. Kulkarni, R. L. Weiler, IEEE Trans. NS-30, August 1983.

- ☒ Prefer Poster Session
☐ Prefer Oral Session
☐ No Preference
☐ Special Requests for placement of this abstract:
☐ Special Facilities Requested (e.g., movie projector)

Submitted by:

Charles D. Striffler

(signature of APS member)

Charles D. Striffler

(same name typewritten)

Lab. for Plasma and Fusion Energy Res
University of Maryland, College Park,
(address)

MD 20742

This form, or a reasonable facsimile, plus *Two Xerox Copies* must be received
NO LATER THAN Noon, Friday, July 15, 1983, at the following address:

Division of Plasma Physics Annual Meeting
c/o Ms. Barbara Sarfaty
Princeton Plasma Physics Laboratory
P. O. Box 451
Princeton, New Jersey 08544

Abstract Submitted
For the Twenty-fifth Annual Meeting
Division of Plasma Physics
November 7 to 11, 1983

Category Number and Subject 4.9 Coherent Radiation Generation

☐ Theory ☒ Experiment

Experimental Studies of High Power Microwave Generation from Rotating Electron Beams in Magnetron-Type Waveguides. W. W. DESTLER, Univ. of Maryland.*--
The generation of high power microwave radiation at high harmonics of the electron cyclotron frequency by the interaction of a rotating electron beam (2 MeV, 2 kA, 5 ns) with inner and/or outer slotted boundary systems has been under study in our laboratory for several years.¹⁻³ In these experiments, a rotating electron beam is produced by passing a non-rotating beam through a narrow magnetic cusp. We have measured the electron beam cross section as a function of axial position downstream of the cusp transition to allow the design of improved magnetron boundaries for radiation production. Results of experiments designed to produce radiation at $20 \omega_{ce}$ (16 GHz), $40 \omega_{ce}$ (32 GHz) and above will be reported.

*Work supported by AFOSR.

¹W. W. Destler, R. L. Weiler, and C. D. Striffler, Appl. Phys. Lett. 38, 570 (1981).

²W. W. Destler, R. Kulkarni, C. D. Striffler, and R. L. Weiler, J. Appl. Phys. July 1983 (to be published).

³C. D. Striffler, W. W. Destler, R. Kulkarni, and R. L. Weiler, IEEE Trans. NS-30, August 1983 (to be published).

- ☒ Prefer Poster Session
☐ Prefer Oral Session
☐ No Preference
☐ Special Requests for placement of this abstract:
☐ Special Facilities Requested (e.g., movie projector)

Submitted by:

William W. Destler

(signature of APS member)

William W. Destler

(same name typewritten)

Lab. for Plasma and Fusion Energy Res.
Univ. of Maryland, College Park, MD
(address) 20742

This form, or a reasonable facsimile, plus *Two Xerox Copies* must be received
NO LATER THAN Noon, Friday, July 15, 1983, at the following address:

Division of Plasma Physics Annual Meeting
c/o Ms. Barbara Sarfaty
Princeton Plasma Physics Laboratory
P. O. Box 151

Abstract Submitted
For the Twenty-fifth Annual Meeting
Division of Plasma Physics
November 7 to 11, 1983

Category Number and Subject 4.9.1 Gyrotrons and Cyclotron Masers

☐ Theory ☒ Experiment

Microwave Generation from a Cusptron Device.
W. NAMKUNG, W. LAWSON, and D. BYUN, University of Maryland.*--A cusptron device¹ holds promise as a tunable, high-frequency microwave tube using a low energy rotating electron beam and low magnetic fields. Experimental studies of this device for microwave generation are being conducted. An annular electron beam of 17 KeV energy with 3 cm diameter and 0.2 cm thickness is produced by a Pierce-type electron gun and is injected through a cusped magnetic field to produce a rotating beam in a downstream drift tube. An $N = 6$ magnetron-type structure is placed immediately downstream of the cusp transition. The electron beam dynamics in the system are measured for various parameters and show good agreement with theoretical predictions. The results of initial radiation measurements will be presented.

*This work is supported by AFOSR and the University of Maryland Computer Center.

¹W. Namkung, W. W. Destler, W. Lawson, and C. D. Striffler, Bull. Am. Phys. Soc. 27, 1062 (1982).

- ☒ Prefer Poster Session
☐ Prefer Oral Session
☐ No Preference
☐ Special Requests for placement of this abstract:
☐ Special Facilities Requested (e.g., movie projector)

Submitted by:

Won Namkung
(signature of APS member)

Won Namkung
(same name typewritten)

Lab. for Plasma and Fusion Energy Res.
Univ. of Maryland, College Park, MD
(address) 20742

This form, or a reasonable facsimile, plus *Two Xerox Copies* must be received
NO LATER THAN Noon, Friday, July 15, 1983, at the following address:

Division of Plasma Physics Annual Meeting
c/o Ms. Barbara Sarfaty
Princeton Plasma Physics Laboratory
P. O. Box 451
Princeton, New Jersey 08544

1984 IEEE International Conference on Plasma Science
May 14-16, 1984, St. Louis, MO

Category Number and Subject 18 High Power Microwave and Submillimeter
Wave Generation

High Power Microwave Generation from a Cusp-
Injected Intense Relativistic Electron Beam*

R. KULKARNI, W. W. DESTLER, W. G. LAYSON, C. D. STRIFFLER, and S. B. SWANKAMP, University of Maryland, Electrical Engineering, College Park, MD 20742.

--The generation of high power microwave radiation from an intense cusp-injected relativistic electron beam interacting with various wall structures has been investigated for the last several years. Initial investigations involved smooth coaxial walls¹ and more recently slotted walls.²⁻⁴ A summary of these results, experimental and theoretical, is presented.

The narrow magnetic cusp allows for the creation of a thin intense rotating E-layer with nominal operating parameters of 2 MeV, 2 kA and a pulse width of ~ 5 ns. The cusp-injection technique has the advantage of high power electron beam input into the interaction region while maintaining a high degree of beam quality. In the experiment, the radiation spectrum is examined in X-band (8-12 GHz), Ku-band (12-18 GHz), and Ka-band (26-40 GHz) as a function of the applied cusp magnetic field and the particular waveguide wall structure. Experimental results are presented for inner and outer slotted wall structures of 12, 20, and 40 slots respectively. Strong interaction is observed with the rotating E-layer at the 2π mode of the slotted wall structures with typical powers of 500 MW with a 12 slot wall configuration (9.6 GHz) and 500 MW and 10 MW with 20 and 40 slot wall configurations (16 GHz and 32 GHz). The slot dimensions are critical for single mode operation at the 2π ($\sim N\omega$) frequency. The feasibility of using alternate slow wave structures such as dielectrics is currently being investigated.

A systematic theoretical examination of the beam-waveguide interaction is also presented. The complete mode structure for the empty slotted wall structure is presented along with the linear stability analysis of the resonant interaction with the beam mode $\omega = \omega_0 + k_y v_{\perp}$. The initial starting condition, namely the cusp injection, is shown to be critical relative to mode selection and operation at the 2π mode. Also, the injection radius effectively selects the proper radial mode number, and for strong coupling the beam must be close to the slotted wall structure. Radiated power spectra are also calculated. Initial theoretical studies are presented of the vacuum dispersion relation for a dielectric lined waveguide along with the linear interaction of a rotating electron beam with the modes of the dielectric liner.

*Work supported by AFOSR and U. Maryland Computer Science Center.

1. W. W. Destler, H. Romero, C. D. Striffler, R. L. Weiler, and W. Sankung, J. Appl. Phys. 52, 2740 (1981).
2. W. W. Destler, R. L. Weiler, and C. D. Striffler, Appl. Phys. Lett. 38, 570 (1981).
3. W. W. Destler, R. Kulkarni, C. D. Striffler, and R. L. Weiler, J. Appl. Phys. 55, 4152 (1983).
4. C. D. Striffler, W. W. Destler, R. Kulkarni, and R. L. Weiler, IEEE Trans. Nucl. Sci. 31, 3129 (1983).

Abstract Submitted

1984 IEEE International Conference on Plasma Science
May 14-16, 1984, St. Louis, MO

High Harmonic Microwave Generation from a
Non-Relativistic Cusptron Device.* WON

NAMKUNG, Electrical Engineering Department, University of Maryland, College Park, MD 20742.--Microwave radiation at the sixth harmonic of the electron cyclotron frequency has been produced through the negative mass instability by the resonant interaction of a non-relativistic rotating electron beam and a conducting boundary with six vanes. This device, which we call a cusptron,¹⁻³ uses very low magnetic fields since it produces radiation at a high harmonic of the electron cyclotron frequency.

An annular electron beam of 3 cm diameter and 0.2 cm thickness is produced by a Pierce-type electron gun and is injected through a cusped magnetic field to produce an axis-encircling electron beam (E-layer) in a downstream drift tube. An anode with an annular slit is attached to an iron plate which sharpens the cusp field. The diode is typically operated at 17 kV, 0.6-1.0 A, and 3 μ s. The conducting boundary in the beam-wave interaction region has six equally spaced vanes of 1.84 cm inner radius and 3.68 cm outer radius. Typical microwave power detected by the receiving antenna is 500 W and the microwave frequency is 4.38 GHz which corresponds to the sixth harmonic of the electron cyclotron frequency at a magnetic field of only 260 G.

In this paper, we present the details of the sixth harmonic generation experiment and also preliminary results of an experiment designed to produce radiation at the twelfth harmonic.

*This work is supported by AFOSR.

1. W. W. Destler, R. L. Weiler, and C. D. Striffler, Appl. Phys. Lett. 38, 570 (1981).
2. W. Namkung, Phys. Fluids, 26, xxx (1984).
3. H. S. Uhm, J. M. Kim, and W. Namkung, Phys. Fluids, 26, xxx (1984).

Subject category and number:

18. High Power Microwave and
Submillimeter Wave Generation

- ☒ Paper presentation
☐ Paper poster session
☐ No preference
☐ Special requests for placement of this Abstract

Submitted by:

Won Namkung

Electrical Engineering Dept.

University of Maryland

College Park, MD 20742

(301)454-7086

Abstract Submitted

1984 IEEE International Conference on Plasma Science
May 14-16, 1984, St. Louis, MO

Millimeter Wave Radiation from a Rotating
Electron Beam in a Rippled Magnetic Field.*

G. BEKEFI and R. E. SHEFER, MIT, and W. W. DESTLER, University of Maryland.--We report the generation of millimeter wave radiation produced by a rotating electron beam interacting with a rippled magnetic field. In the experiments, a 12 cm diameter, hollow, rotating electron beam (2 MeV, 1-2 kA, 5 ns) is generated by passing a hollow non-rotating beam through a narrow magnetic cusp. The rotating beam performs helical orbits ($\beta_{\theta} \approx .95$, $\beta_z \approx .2$) downstream of the cusp in an axial guide field of about 1450 Gauss. Radiation is produced by the interaction of the beam with an azimuthally periodic wiggler magnetic field produced by samarium cobalt magnets located interior and exterior to the beam. In the present work, the wiggler field has an amplitude of about 1300 Gauss, six spatial periods around the azimuth, and a periodicity of 6.28 cm. We have observed at least 200 kW of radiation above 91 GHz in initial experiments,¹ a result consistent with the frequency expected for a linear Free Electron Laser operating with comparable parameters. Radiation at these frequencies is not observed in the absence of the wiggler field. Numerical calculations of the electron orbits in the combined axial and wiggler fields indicate that the orbits are relatively unperturbed in the $r-\theta$ plane and that the perturbation of the orbits due to the wiggler is primarily axial, as desired. Measurements of the actual circulating current exciting the wiggler region with and without the wiggler magnets in place confirm that the wiggler field does not have a seriously adverse effect on the electron orbits. Measurements of the radiation spectrum using a grating spectrometer and studies of the effects of wiggler amplitude and periodicity are currently underway.

*This work was supported in part by The Air Force Office of Scientific Research, The Department of the Air Force Aeronautical Systems Division, and in part by the National Science Foundation.

1. G. Bekefi, R. E. Shefer, and W. W. Destler, Appl. Phys. Lett. 44, 280 (1984).

18. High Power Microwave and Submillimeter Wave Generation

Prefer Poster Session

William W. Destler

William W. Destler

Laboratory for Plasma and
Fusion Energy Studies

University of Maryland

College Park, MD 20742

(301)454-3187

END

FILMED

6-85

DTIC